Modeling, Analysis and Control of quasi-Z-Source Inverters

Farzaneh Bagheri

Submitted to the
Institute of Graduate Studies and Research
in partial fulfillment of the requirements for the degree of

Doctor of Philosophy
in
Electrical and Electronic Engineering

Eastern Mediterranean University
September 2019
Gazimağusa, North Cyprus

Approval of the Institute of Graduate Studies and Research

Prof. Dr. Ali Hakan Ulusoy
Acting Director

I certify that this thesis satisfies the requirements as a thesis for the degree of Doctor of Philosophy in Electrical and Electronic Engineering.

Prof. Dr. Hasan Demirel
Chair, Department of Electrical and Electronics Engineering

We certify that we have read this thesis and that in our opinion, it is fully adequate, in scope and quality, as a thesis of the degree of Doctor of Philosophy in Electrical and Electronic Engineering.

Prof. Dr. Osman Kükrer
Co-Supervisor

Prof. Dr. Hasan Kömürcügil
Supervisor

Examining Committee

1. Prof. Dr. Erdal Bekiroğlu
2. Prof. Dr. Murat Doğruel
3. Prof. Dr. Hasan Kömürcügil
4. Prof. Dr. Osman Kükrer
5. Prof. Dr. İbrahim Sefa
6. Prof. Dr. Şener Uysal
7. Assoc. Prof. Dr. Reza Sirjani

ABSTRACT

This thesis aims to develop new control methods for the single-phase quasi-Z-source inverters (qZSIs). The key challenge lies in the design of suitable control method for the qZSI which is a nonlinear multi-input-multi-output (MIMO) system. Hence, from the control point of view, developing an integrated control technique is a challenging issue. Although the conventional control methods attain reasonable responses, suppression of double frequency ripple (DFR), robustness against parameter variations and simplification issues are still open issues. Thus, the proposed new control methods target to achieve these objectives.

A novel approach which is created based on the model of the system while tuning the current of the system (MBCC) with DFR mitigation, virtual time constant and active damping to damp the resonances of the LCL filter is presented for a grid-tied qZSI as the first control method in this thesis.

The second control method proposed in this thesis is a MIMO sliding mode control (SMC) which aims to control all variables of qZSI concurrently. This control approach not only synchronizes the control of all state variables at the same time, but also offers simplification in the implementation without using proportional-integral (PI) controllers in the dc-side, robustness to parameter variations, DFR mitigation when the sliding constant in the dc-side is selected appropriately and fixed switching frequency by introducing boundary layer technique. The boundary layer smooths the sliding functions and makes them appropriate for the PWM process. The applicability of the MIMO SMC method is also investigated for a single-phase high gain Z-source inverter which is called switched Z-source inverter (SZSI) in the literature. The effectiveness and validity of the proposed control methods are supported by simulation results in MATLAB/Simulink environment and the experimental results. The results show that the DFR mitigation approach can remove the DFR in the inductor current successfully and the MBCC method is also an efficient approach with fast dynamic response, zero steady state error and active damping of the resonance. Moreover, MIMO SMC can also achieve the goals with zero steady state error, robustness against parameter variation and fast dynamic response while attaining fixed switching frequency.

Keywords: Active damping, double frequency ripple, quasi-Z-source inverter, LCL filter, proportional-resonant control, boundary layer, sliding mode control, switched Z-source inverter

ÖZ

Bu tez, tek-faz yarı-empedans-kaynaklı evirgeçler (qZSI) için yeni denetleme yöntemleri geliştirmeyi amaçlamaktadır. Uygun bir denetim yönteminin tasarımındaki kilit zorluk, qZSI'nin doğrusal olmayışı ve çoklu-giriş çoklu-çıkış (MIMO) bir sistem olmasında yatmaktadır. Bundan dolayı, denetim açısından bakıldığı zaman karma bir denetim yöntemi geliştirmek oldukça zorlu bir konudur. Geleneksel denetim yöntemleri bu evirgeç topolojisi için makul durağan ve dinamik tepki cevaplarına ulaşsa bile, çift frekans dalgacık bastırımı (DFR), parametre değişikliğine karşı gürbüzlük ve uygulamadaki basitleştirme hala daha açık olan konulardır. Bu nedenle, önerilen yeni denetim yöntemleri bu amaçları başarmayı hedeflemektedir.

Bu tezdeki ilk denetim yöntemi olarak, tek-faz şebekeye bağlı qZSI için DFR azaltma ve sanal zaman sabiti özellikleri bulunan modele dayalı akım denetim (MBCC) yöntemi önerilmiştir. DFR azaltma, dc taraftaki kondansatör ve indüktör gerilimleri arasındaki faz ilişkisini kullanarak başarılırken, ac tarafın denetimi qZSI modeline dayanan MBCC tarafından yapılmıştır. Aktif sönümleme ve sanal zaman sabiti içeren akım denetimi, evirgeç akımının kendi referansını takip etmesini zorlamaktadır.

Bu tezde önerilen ikinci denetim yöntemi olarak qZSI'nin dc ve ac taraflarındaki değişkenleri ayni anda kontrol etmeyi amaçlayan MIMO kayan kipli denetim (SMC) yöntemidir. Bu denetim yaklaşımı sadece tüm durum değişkenlerinin denetimini ayni anda senkronize etmekle kalmayıp, ayrıca dc tarafta PI denetleyicisi kullanmadığı için uygulamada basitleşme, parametre değişikliğine karşı gürbüzlük, kayan sabit uygun seçildiği zaman DFR azaltma ve sınır tabakası tekniğiyle sabit anahtarlama frekansı sunmaktadır. Sınır tabakası kayan fonksiyonları pürüzsüz yaparak darbe genişlik modülasyon (PWM) işlemi için uygun hale getirmektedir.

Ayrıca, MIMO SMC yönteminin bir tek-faz şebekeye bağlı yüksek kazançlı anahtarlı empedans kaynaklı evirgeçe (SZSI) uygulanabilirliği araştırılmıştır. Yarı-empedans-kaynaklı evirgeç topolojisinde olduğu gibi, bu evirgeç topolojisi de tüm durum değişkenlerinin ayni anda kontrolünün başarılabilmesi için etkili bir denetim yöntemine ihtiyaç duyar. Bu topolojideki ek anahtar denetim yönteminin karmaşık olma pahasına yüksek destek faktörü sunar.

Bu tezde önerilen denetim yöntemlerinin etkisi ve geçerliği MATLAB/Simulink ortamında yapılan benzetim sonuçlarıyla destektenmiştir. Ayrıca, önerilen MBCC ve MIMO SMC yöntemlerinin deneysel sonuçları şebekeye bağlı ve ada modunda çalışan qZSI için sunulmuştur.

Anahtar Kelimeler: Aktif sönümleme, çift frekans dalgacık, yarım-empedans-kaynaklı evirgeç, LCL süzgeç, orantılı-rezonant denetim, sınır tabakası, kayan kipli denetim, anahtarlı empedans-kaynaklı evirgeç

To My Parents

For Their Endless Love, Support and Encouragement

ACKNOWLEDGMENT

I am especially indebted to Prof. Dr. Hasan Kömürcügil for his supervision, advice, and guidance who has been supportive of my career goals and who worked actively to provide me with the protected academic time to pursue those goals. His ideas, experiences, and passions has truly inspired and enriched my growth as a student. As my teacher and mentor, he has taught me more than I could ever give him credit for here. I would also like to acknowledge my co-supervisor, Prof. Dr. Osman Kukrer for his advice, guidance and encouragement.

I am grateful to Dr. Naki Guler who provided me extensive personal and professional guidance in Power Electronic Laboratory of Gazi University.

This work would not have been possible without the financial support of TRNC state scholarship which was given by the Turkish Republic of Northern Cyprus Ministry of National Education and Sports awards.

My special thanks go to my supportive husband, Ali and particularly I wish to thank my son, Hoseyn for his unending patience and inspiration throughout the period of my studies.

TABLE OF CONTENTS

LIST OF TABLES

LIST OF FIGURES

LIST OF SYMBOLS AND ABBREVIATIONS

RES	Renewable energy source
VSI	Voltage-source inverter
CSI	Current-source inverter
UPS	Uninterruptible power supply
IGBT	Insulated gate bipolar transistor
EMI	Electromagnetic interference
ZSI	Z-source inverter
qZSI	Quasi-Z-source inverter
MBCC	Model-based current control
DFR	Double frequency ripple
MIMO	Multi-input multi-output
SMC	Sliding mode control
PWM	Pulse width modulation
SZSI	Switched Z-source inverter
MPC	Model predictive control
qSBI	Quasi-Switched Boost Inverter
nST	Non-shoot through
ST	Shoot through
SBI	Switched boost inverter
EMC	Electromagnetic compatibility
BqZSI	Bidirectional-quasi-Z-source inverter
SL	Switched inductor
SC	Switched-capacitor

SCL	Switched-coupled-inductor
CA	Capacitor assisted
DA	Diode assisted
TL	Terminal-tapped inductor
Trans-qZSI	Transformed based qZSI
SPWM	Sinusoidal pulse width modulation
d_{ST}	Shoot through duty cycle

Chapter 1

INTRODUCTION

1.1 Introduction

Nowadays, energy demand is becoming a problem due to the environmental challenges such as climate change and limited source of energy which basically depends on oil, gas and coal. Furthermore, the main source of heavy pollutants in the air and water is due to burning coal, petroleum and other fossil fuels. Renewable energy sources (RES) such as solar energy, wind energy and water power, which are natural energy sources and have limitless energy with much lower impact on the environment, can protect the planet by significantly reducing the amount of carbon emissions being produced right now. Moreover, less dependency on fossil fuel, gas and oil avoids the rising cost of energy bills which can be considered as the other advantages of the natural power sources.

The most important thing in using RES is the integration of these natural sources to the power distribution system. The voltage-source inverter (VSI) and current-source inverter (CSI) are the most frequently used topologies to transfer energy from a RES to the power system [1]. Inverters, which are used in adjustable-speed ac motor drives, uninterruptible power supplies (UPS), and running ac appliances from an automobile battery, transfer power from a dc source to an ac load or grid [1]. In a VSI, the dc voltage source which can be a battery, fuel-cell, diode rectifier and capacitor feeds the main inverter circuit. Despite its limitations and barriers, the VSI is broadly used [2]:

I. It acts as a buck inverter because the ac output voltage cannot surpass the dc input voltage. Thus, the necessity of an extra dc-dc converter to boost the source voltage to the selected value makes the system costly and lowers efficiency.

II. It has less reliability due to the short circuit of the inverter if both switches of the same leg are switched on at the same time which short circuit the inverter.

III. Compared to CSI, it needs an extra filter to obtain sinusoidal output voltage which causes further power losses and control difficulty.

In CSI, the main inverter circuit is fed by a relatively large dc inductor which is connected to a voltage source like a battery or diode rectifier. The CSI is not popular due to the following limitations and barriers [2]:

I. Due to the boosting characteristic of the system, it needs an extra buck converter to regulate the input voltage to the desired value required value that makes the system costly and lowers efficiency.

II. The open circuit should be avoided in such a system by switching on at least one of the upper switches and one of the lower switches. Else, the open circuit can destroy the switches.

In CSI, it is not possible to use low-cost and high-performance insulated gate bipolar transistor (IGBT) modules directly due to the feature of CSI that the main switches must block reverse voltage that needs a diode with a series connection in mixture with high-speed and high-performance switches.

Both VSI and CSI have the following common limitations [1]:

I. They cannot operate either in buck or in boost mode and need an extra converter to obtain the desired dc input voltage.

II. VSI and CSI cannot be replaced with each other in the necessary time due to the different connection of switches.

III. They are exposed to electromagnetic interference (EMI) noise due to the reliability problem.

To overthrow the aforementioned limitations of the traditional VSI and CSI, Z-source inverter (ZSI) and other modified impedance source inverters are presented in [2]. These new topologies benefit a unique impedance network to connect the inverter to the grid, load, or another converter.

Among the existing topologies of the impedance source inverters, the quasi-Z-source inverter (qZSI), which is an improved type of ZSI, is widely used and got more consideration due to its promising behaviors such as boost/buck operation ability, less number of active devices compared to the dual-stage topology, increased reliability due to unused dead-band time, simpler design, increased efficiency, constant input current and less stress on the components in the impedance system[3]-[19].

1.2 Thesis Objectives

In this section, the main objectives of the thesis are listed to overcome the drawbacks in the controller design of the qZSI. When the single-phase qZSI is employed in the grid-tied or standalone modes, there are some main concerns regarding controller design: 1) robustness; 2) simplicity of design; 3) the number of sensors in ac and dc sides; 4) steady-state error at output. With these concerns in mind, new control strategies that target to achieve the required goals are proposed here. Therefore, in chapter 3, a novel controller based on the model of the system planned to control the current (MBCC) is presented for the grid-tied qZSI with LCL-filter operating in single-phase operation mode. This method concurrently removes the double frequency ripple (DFR) existing in single-phase inverters while injecting a sinusoidal current to the grid as well by using the proposed active damping and virtual time constant idea.

Besides, a multi-input multi-output (MIMO) sliding mode controller (SMC) is proposed. This control method synchronizes the control of all state variables in the system, achieves robustness to any changes in parameters and less difficulty in the implementation as no proportional-integral (PI) controller is used in the dc-side. It requires only two gains in the dc-side and one gain in the ac-side with a low number of sensors on both sides of the inverter. The computation of dc- and ac-side control variables is considerably simple and easy. Due to the independence of the control inputs on the system parameters, it is robust to parameter variations. Unlike the traditional SMC methods, the proposed control approach results in fixed switching frequency which is attained by flattening the sliding manifolds in narrow border layers employed for both dc- and ac-sides separately. In this technique, the chattering of the sliding functions is alleviated, and the discontinuous control inputs are changed to continuous signals. In this case, the continuous control signals can be analogized with a triangular carrier signal to generate the pulse width modulation (PWM) signals needed to drive the switches of the inverter. On the other hand, the zero steady-state error in output voltage, which is one of the control objectives, is achieved by means of a proportional-resonant (PR) controller which generates the filter inductor current reference by processing the difference of the load voltage and its reference. Moreover, unlike the traditional methods which generate the dc side inductor current reference using PI controllers, the qZS network inductor current reference is generated with the help of a power balance equation in which the measurement of the inverter input current is essential.

Finally, the MIMO SMC introduced in chapter 4 is also applied to control a high gain switched-boost inverter in chapter 5. The switched boost inverter which is called switched Z-source inverter (SZSI) is the family of impedance source inverters with continuous input current and the same number of passive elements in comparison with ZSI and qZSI [53]. The simulation results under linear and nonlinear loads are presented to verify the feasibility of the proposed control method in achieving the desired control objectives such as sinusoidal output voltage with low total harmonic distortion (THD), improved dynamic response, zero steady-state error in tracking dc- and ac-side variables and a fixed switching frequency.

1.3 Literature Survey

In single-phase inverters, an inevitable DFR exists in dc-side current because of the instantaneous output power double frequency ripple. This DFR power in the dc side leads to double frequency ripples in voltage and current of the capacitors and inductors of the traditional single-phase H-bridge inverter and the single-phase ZSI family. Elimination or even attenuation of DFR is one of the most challenging issues investigated in the literature [13]-[24]. The DFR decreases the lifetime and effectiveness of the photovoltaic (PV) array used to supply energy [14]. Besides, it leads to undesired fluctuations in all variables of the system and undesired harmonics in the output voltage and current of the inverter. Compensation of DFR propagation through qZSI can be made possible by filtering the ripple via an energy storage component. On the other hand, it is also possible to compensate it by using active and passive buffering. While passive buffering uses huge inductors and capacitors to reduce the ripples and increases cost and size [13], active buffering alleviates the ripples through using active devices to divert the pulsating power into an additional small valued capacitor [14]-[15], [20]-[21]. Additional switching devices and capacitor not only increase the cost, but also deteriorate reliability of the system.

The dual voltage control method, which controls the output power and double frequency power in distinct loops removes the necessity for extra storage components [22]. However, this method suffers from long time computation process, control difficulty and failure in pulsating power compensation during transients [23].

New modulation techniques [16], [18] and closed loop control method [24] are also used to remove the ripples. However, the modulation method in [16] causes a reduction in the electrolytic capacitor's size connected in parallel with PV terminals, the DFR component still exists on the capacitor voltages. Also, there are no results regarding the dc-side inductor currents in [16]. On the other hand, the hybrid modulation technique in [18] and control method in [24] minimize the qZS components, while the DFR component still happens in the qZS network. On the other hand, in LCL filtered grid-tied inverters, resonance damping is essential. Passive damping in [25] is achieved by using additional power loss elements such as resistors.

Active damping is made possible by controlling inverter current in [26], by controlling capacitor current in [27], grid current in [28], both grid current and voltage of the filter capacitor in [29], capacitor voltage and both inverter and grid currents in [30], [31], and all variables in [32]. According to [33], controlling only single parameter in a one-loop method is not enough to attain damping, thus, resonance alleviation can be achieved by regulating two [29] and three parameters [30], [31]. This achievement can be made possible at the expense of losing some of the aspects such as robustness against variations, fast dynamic response, and less steady-state error in the grid current.

Furthermore, the qZSI is a nonlinear MIMO system that has a challenging mathematical model to control the entire system concurrently. Since dc and ac side variables affect each other, therefore a control method should be designed for such a system to consider all variables in one state-space model and control all variables simultaneously. To control the entire system, both qZS network and the inverter should be controlled concurrently. Numerous control methods including classical PI and nonlinear controllers are proposed for qZSI to attain fast dynamic response, good steady-state performance and robustness against parameter variations [11], [14], [18], [35]-[45]. Nevertheless, due to the nonlinearity of qZSI, the development of the integrated control technique is a challenging topic [83].

To control the whole variables of the system including current and voltages of the dc side and current or voltage of the ac side, multiple feedback control methods are proposed to adjust the value of the shoot-through duty cycle and the modulation index [14]–[17]. Classical PI controllers are the popular methods which control the variables of qZSI [11], [12], [14], [18], [34]-[44]. Nevertheless, the conventional linear controllers are simple in theory and implementation, but they are ineffective in achieving acceptable performance at all operating points for the nonlinear systems.

Due to the inherent nonlinearity of the qZSI, nonlinear controllers such as fuzzy control [35], [36], neural network control [37], model predictive control (MPC) [38]-[41] and SMC [12], [42]-[44], [85] are proposed. The nonlinear controllers are presented to improve the dynamic response and attain the robustness of the system against parameter variations. Although the MPC approach is used in such nonlinear systems owing to its effectivity in achieving the control of all variables in one stage, it can destroy the system performance because of the lack of robustness and vulnerability to parameter variations. Therefore, considering the drawbacks in the fuzzy and neural network controllers, the SMC is the widely preferred method due to its features such as implementation simplicity, strong robustness and fast dynamic response. Though, it suffers from chattering and variable switching frequency [45]. In [12] and [42]-[43], the SMC approach is only used to control the dc-side variables (qZS network currents and voltages) and the classical PI controllers are used for adjusting the ac-side variables. Furthermore, employing PI controllers in [42] to regulate ac signals lead to steady-state errors. On the other hand, the dc side inductor current reference generation in [42] is not mentioned. Besides, the method for dc side inductor current reference generation seems unsuccessful due to the disability of the system during the transients caused by load changes.

The hyper-plane MIMO SMC proposed in [44] regulates all state variables concurrently. However, the reference generation and controlling dc side variables are still based on using classical PI controllers. On the other hand, the control inputs (shoot-through duty cycle and modulating signal) include continuous and discontinuous components. Hence, calculation and implementation of the control variables is complicated and takes a fraction of the time. Additionally, the ac side sliding surface manifold requires an integral process which also increases the implementation difficulty. Also, the robustness of dc-side control is not achieved due to the dependency of the dc side control method on the system parameters. Moreover, there is no data about chattering elimination/mitigation.

One of the most important perspectives in developing the ZSI and qZSI family is to increase the boost factor by improving the topologies. Many studies have been established in improving the topology to increase boost factor [47]-[53]. Quasi-SBI (qSBI) was proposed in [47] and [48] to boost the output voltage gain. This topology can perform higher effectiveness with a smaller number of passive elements and one extra switch used in the impedance network [48]. A series of high boost SL-qSBIs were presented in [49]-[51] by replacing the inductor in the qSB network with one switched-inductor (SL) cell. However, it suffers from high voltage stress on passive and active components and high ripple in the input current. Similarly, by applying the SC-cells into the qSB network, high boost SC-qSBIs were proposed in [52]. In [53] and [86], a new high-gain voltage switched qZSIs with continuous input current and the same number of passive elements in comparison with ZSI and qZSI is proposed. Although SZSI has a high boost factor, it has the same voltage stress on the components in comparison with ZSI [53].

1.4 Contribution of the Thesis

The main contribution of this thesis is to propose control methods to overcome the problems existing in control of qZSI. In chapter 3 of this thesis, the DFR existing in the variables of the qZSI is mitigated through an idea based on the mathematical relation between the DFR of the inductor voltage and capacitor current of the qZS network. The dc side control is performed by modifying the conventional PI controller while using simple boost control. Through using this adjustment, the qZS the output of the first PI controller which is the inductor current reference does not hold double frequency ripple component. A MBCC method is also proposed for controlling ac side of the grid tied qZSI through an LCL filter. This method generates the inverter current in such a way that tracks its reference with approximately zero steady state error while using a virtual time constant to fasten the dynamic response. Furthermore, the active damping technique used to damp the resonance of the LCL filter adjusts the inverter output current reference instead of the inverter voltage reference presented in [28] and [32].

Chapter 4 proposes a MIMO SMC method that synchronizes the control of all state variables of the qZSI. Different from the existing SMC based approaches, the dc- and ac-side variables are completely controlled by the proposed SMC concurrently. This method gets the benefit of the boundary layer approach to mitigate chattering existing in the sliding mode control method and fix the switching frequency. Fixed switching frequency operation is highly desirable in practice. The use of only two gains in the dc-side and one gain in the ac-side makes this method considerably simple and easy to simulate and implement. The control inputs are the smoothed sliding surfaces which do not depend on the system parameters. Instead of the conventional linear PI controller, the dc side inductor current reference is generated by using the power balance equation. The ac-side inductor current reference is generated by a PR controller by regulating the load voltage. In this case, a zero steady-state error in the load voltage is achieved.

Chapter 5 introduces a MIMO SMC method to generate modulation signal and shoot trough duty cycle simultaneously to achieve the desired control objectives for SZSI. The sliding surface functions are designed using the difference of only one variable which eliminates using derivative operations on the contrary to the conventional SMC methods. To remove the discontinuity of the sliding function and chattering, the idea of the boundary layer is utilized to fix the frequency and limit the sliding surface function in a narrow manifold.

1.5 Conclusion

This thesis aims to propose effective control methods to control the impedance source inverters. In the third chapter, the grid-tied LCL filtered single-phase qZSI is controlled by a MBCC method which compensates the DFR in dc side components and achieves the ac- side control with virtual time constant. The feasibility of the control method is investigated by experimental results which verifies the theory and suggested idea.

In the fourth chapter, a MIMO SMC methodology is proposed to control the qZSI in both grid-tied and standalone mode. The proposed control has the ability for controlling dc and ac side variables of the qZSI simultaneously. Unlike the existing control SMC approaches, the proposed control approach does not employ any PI controller in the dc side. It offers a better dynamic response, robustness, and less complexity in implementation. Furthermore, the steady-state error in the load voltage is eliminated using PR controller in the ac side. Also, the fixed switching frequency is made possible by smoothing the sliding surface function through a boundary layer. The feasibility and effectiveness of the presented control methodology are validated through experimental results under linear and nonlinear load types standalone mode and by simulation results in grid-tied mode.

The proposed MIMO SMC has been also applied to a novel topology called ZSI which is a new generation of the ZSI family with a very high boost factor. The proposed SMC combines the control of dc- and ac-side variables into a compact form of equations which simplifies the controller design. Because of the proposed sliding surface functions, the derivative operation is not needed. Also, due to the smoothing operation applied to the sliding surface functions, it is shown that the switching frequency is fixed for all time (except for the start-up and transients). The simulation results under linear and nonlinear loads verify the feasibility of the offered control approach in achieving the desired control objectives such as sinusoidal output voltage with low THD, fast dynamic response, zero steady-state error in tracking dc- and ac-side variables and a fixed switching frequency.

Chapter 2

IMPEDANCE SOURCE INVERTER TOPOLOGIES AND PWM TECHNIQUES

2.1 Introduction

This chapter introduces some well-known topologies in the family of qZSI and their pos and cons. Furthermore, the PWM methodologies of single-phase impedance source inverters are also investigated in this chapter.

2.2 Z-Source Inverter (ZSI)

ZSI is one of the greatest auspicious networks that can be used instead of CSI and VSI topologies. The ZSI is an emerging topology that can be used for converting ac to dc and dc to ac with fascinating aspects such as buck-boost features and single-stage conversion [2]. Figure 2.1 shows a single-phase ZSI which is a set of two capacitors and two inductors linked in an X form, linking dc input voltage to the inverter main circuit. The shoot-through (ST) state which means switching on both switches of one leg of the inverter simultaneously is the benefit of this network that increases the input voltage, advances the inverter reliability and expands its application areas. The other benefits of this ZSI are one-stage conversion, buck-boost capability with lower prices, smaller size, and greater effectiveness owing to less number of elements.

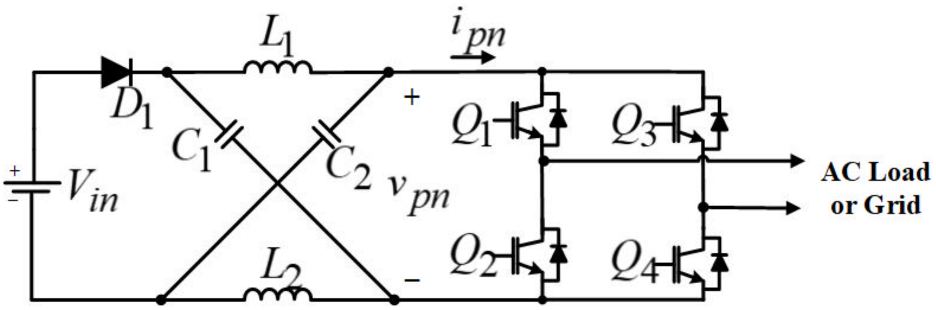

Figure 2.1: Z-source inverter

The advantage of the ZSI over the traditional VSI and CSI is that the output ac voltage can have any value between zero and a value which is greater or less than the input dc voltage. Therefore, it can be a buck-boost inverter.

According to Table 2.1, unlike traditional single-phase inverter which has 4 switching states, the single-phase ZSI has five permissible switching states (vectors). Traditional VSI has two active states where output voltages are V_{in} and $-V_{in}$ and two zero states where the output voltage is zero.

Table 2.1: Switching states of ZSI

Switch state	State	Output voltage
$Q_1, Q_4 \Rightarrow ON$, $Q_2, Q_3 \Rightarrow OFF$	Active	V_{in}
$Q_2, Q_3 \Rightarrow ON$, $Q_1, Q_4 \Rightarrow OFF$	Active	$-V_{in}$
$Q_1, Q_3 \Rightarrow ON$	Zero	0
$Q_2, Q_4 \Rightarrow ON$	Zero	0
$Q_1, Q_2 \Rightarrow ON$ OR $Q_3, Q_4 \Rightarrow ON$ OR all the switches are ON concurrently	Shoot through	0

The ZSI has another extra ST state which is due to the concurrent switching of two switches on one leg and is forbidden in traditional inverters. Therefore, ZSI has three different states: active-state, zero-state and shoot-through state. The equivalent circuit of ZSI in non-shoot-through (nST) and shoot-through (ST) states are revealed in Figure 2.2. In ST state, while the inverter is short-circuited, it behaves like a current source in nST state. It should be mentioned that the zero state can be considered in the active state due to considering it like a current source with zero value.

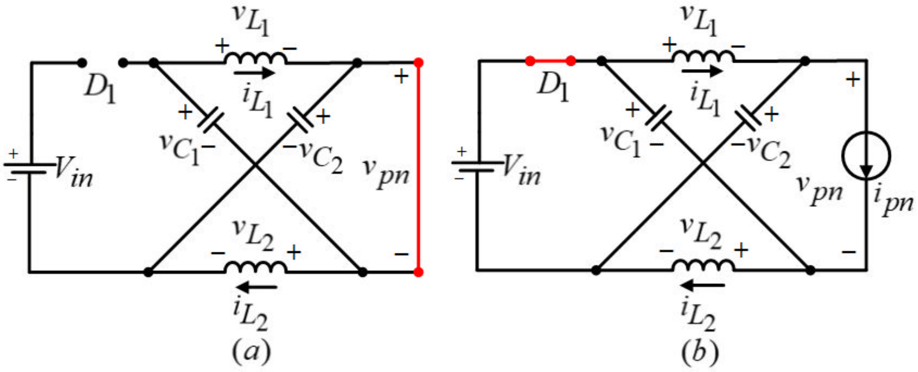

Figure 2.2: Equivalent circuit of ZSI (a) ST state, (b) nST state

If we assume that $L_1 = L_2 = L$ and $C_1 = C_2 = C$ to make the circuit symmetric, then the following equations can be written [2]

$$v_{C_1} = v_{C_2} = V_C \quad , \quad v_{L_1} = v_{L_2} = V_L \tag{2.1}$$

Where all the dc side variables can be written as the addition of dc part and DFR components as $v_{C_1} = V_{C_1} + \tilde{v}_{C_1}$, $v_{C_2} = V_{C_2} + \tilde{v}_{C_2}$, $v_{pn} = V_{pn} + \tilde{v}_{pn}$, $i_{L_1} = I_{L_1} + \tilde{i}_{L_1}$, $i_{L_2} = I_{L_2} + \tilde{i}_{L_2}$.

However, in equation (2.1) the DFR component of the capacitor and inductor voltages are ignored. According to Figure 2.2(a), the equations of the circuit in ST state are

$$V_L = V_C \quad , \quad V_{in} = 2V_C , \quad v_{pn} = 0 \tag{2.2}$$

According to Figure 2.2(b), the equations of the circuit in nST state are

$$V_L = V_{in} - V_C \,, v_{pn} = V_C - v_L = 2V_C - V_{in} \tag{2.3}$$

where V_{in} is the dc input voltage and v_{pn} is the output voltage of Z-source network. Since the average voltage of the inductors over one switching period (T_{sw}) is zero in steady state, thus from (2.2) and (2.3), the following is obtained:

$$V_L = \frac{T_{ST}V_C + T_{nST}(V_{in} - V_C)}{T_{sw}} = 0 \tag{2.4}$$

Solving for V_C gives

$$V_C = \frac{T_{nST}V_{in}}{T_{nST} - T_{ST}} = \frac{(1-d_{ST})V_{in}}{1-2d_{ST}} \tag{2.5}$$

where T_{ST} is the shoot through time, T_{nST} is the non-shoot through time and d_{ST} is the shoot through duty cycle defined as $d_{ST} = \frac{T_{ST}}{T_{sw}}$, respectively. The output voltage of Z-source network (v_{pn}) is obtained as follows, while the boost factor is denoted as B.

$$v_{pn} = 2V_C - V_{in} = 2\frac{(1-d_{ST})V_{in}}{1-2d_{ST}} - V_{in} = \frac{1}{(1-2d_{ST})}V_{in} = BV_{in} \tag{2.6}$$

2.3 Quasi-Z-Source Inverter (qZSI)

The quasi-ZSI (qZSI) is an integrated version of ZSI with more benefits, including a lower element rating due to less voltage on capacitors comparing to ZSI, reducing the noise existing in the system due to the joint earthing of the input power source and the dc link and achieving continuous input current owing to the presence of an input coil [54]-[56]. The conventional qZSI which is shown in Figure 2&3 gets the entire benefits of the ZSI. The qZSI takes a dc input voltage and can buck or boost it with a given boost factor. Nevertheless, there are some unique advantages for qZSI which makes it a better selection than ZSI:

I. qZSI needs lower capacitor rating, due to lower capacitor voltage.

II. The input current stress significantly reduces due to the continuity of the input current of the qZSI, while the ZSI has discontinuous input.

III. Easier assembling and less EMI problems occur in qZSI due to a mutual dc point between the source and inverter.

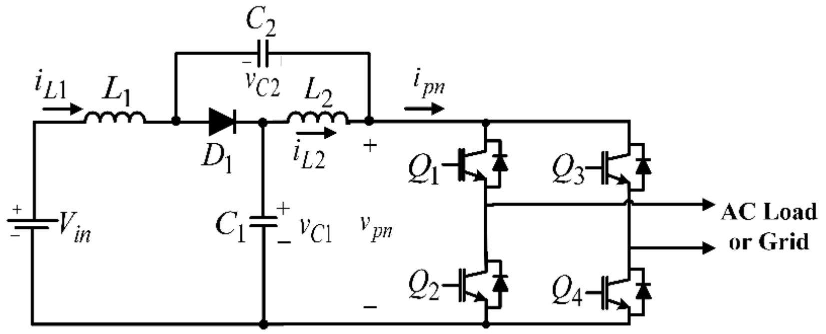

Figure 2.3: Quasi-Z-source inverter (qZSI)

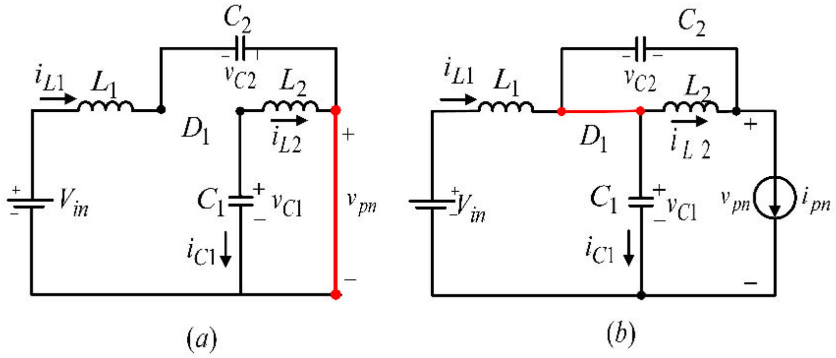

Figure 2.4: Equivalent circuit of qZSI (a) ST state (b) nST state

The control methods used for ZSI can be used for qZSI similarly. Same as ZSI the operation of qZSI, can be broken down into two modes; the nST mode and the ST mode, where the nST mode is included of active and zero states. The equivalent circuit of qZSI in nST and ST states are revealed in Figure 2.4.

In nST mode, one and only one device in each phase leg conducts and control of inverter is same as traditional VSI. The ST mode occurs when at least one leg is switched on. The voltage across the inverter (v_{pn}) during this mode is zero. If $L_1 = L_2 = L$ and $C_1 = C_2 = C$ to make the circuit symmetric.

Where all the dc side variables can be written as the addition of dc part and DFR components as $v_{C_1} = V_{C_1} + \tilde{v}_{C_1}$, $v_{C_2} = V_{C_2} + \tilde{v}_{C_2}$, $v_{pn} = V_{pn} + \tilde{v}_{pn}$, $i_{L_1} = I_{L_1} + \tilde{i}_{L_1}$, $i_{L_2} = I_{L_2} + \tilde{i}_{L_2}$. The equations of the circuit for ST state according to Figure 2.4(a) are given as

$$v_{L_1} = V_{in} + v_{C_2} \ , \ v_{L_2} = v_{C_1} , \ v_{pn} = 0 , \ i_{C_1} = -i_{L_2} , \ i_{C_2} = -i_{L_1} \tag{2.7}$$

The equations of the circuit for nST state according to Figure 2.4(b) are given as

$$v_{L_1} = V_{in} - v_{C_1} \ , \ v_{L_2} = -v_{C_2} , v_{pn} = v_{C_1} + v_{C_2}$$

$$i_{C_1} = i_{L_1} - i_{pn} , \ i_{C_2} = i_{L_2} - i_{pn} \tag{2.8}$$

Since the average voltage of inductors in steady state over one switching period is zero, so it can be written as

$$V_{L_1} = \frac{T_{ST}(V_{in} + v_{C_2}) + T_{nST}(V_{in} - v_{C_1})}{T_{sw}} = 0$$

$$V_{L_2} = \frac{T_{ST}(v_{C_1}) + T_{nST}(-v_{C_2})}{T_{sw}} = 0 \tag{2.9}$$

If (2.9) is solved to find v_{C_1} and v_{C_2}, it gives

$$v_{C_1} = V_{in}(\frac{1 - T_{ST}}{1 - 2T_{ST}}) \ , \ v_{C_2} = V_{in}(\frac{T_{ST}}{1 - 2T_{ST}}) \tag{2.10}$$

If the capacitor voltages are presented in terms of the duty cycle yields

$$v_{C_1} = V_{in}(\frac{1 - d_{ST}}{1 - 2d_{ST}}), \quad v_{C_2} = V_{in}(\frac{d_{ST}}{1 - 2d_{ST}}) \tag{2.11}$$

The output voltage of qZS network and the boost factor can be obtained as

$$v_{pn} = v_{C_1} + v_{C_2} = \frac{1}{(1-2d_{ST})} V_{in} = BV_{in} \quad , \quad B = \frac{1}{1-2d_{ST}} \tag{2.12}$$

On the other hand, since the mean vale of the current of capacitors in steady state over one switching period is zero, hence it can be written as

$$I_{C_1} = \frac{T_{ST}(-i_{L_2}) + T_{nST}(i_{L_1} - i_{pn})}{T_{sw}} = 0$$

$$I_{C_2} = \frac{T_{ST}(-i_{L_1}) + T_{nST}(i_{L_2} - i_{pn})}{T_{sw}} = 0 \tag{2.13}$$

Solving (2.13) for i_{L_1} and i_{L_2} gives

$$i_{L_1} = i_{L_2} = i_{pn}\left(\frac{1-d_{ST}}{1-2d_{ST}}\right) \tag{2.14}$$

The average current of the inductors can be obtained by using system input power rating as following:

$$I_{L_1} = I_{L_1} = \frac{P_{in}}{V_{in}} \tag{2.15}$$

2.4 Switched-Z-Source Inverter (SZSI)

Switched-Z-source inverter (SZSI) is a high gain switched boost inverter (SBI) which is proposed in [53] with continuous input current and the same passive elements in comparison with ZSI and qZSI. Based on the results of [53], although SZSI has high boost factor, it has the same voltage stress on components in comparison with ZSI.

Figure 2.5 shows SZSI. The SZSI includes two inductors (L_1, L_2) and two capacitors (C_1, C_2) which increase the input dc voltage (V_{in}) to the anticipated rate by controlling the shoot-through duty cycle. The main difference between this topology and conventional ZSI is that SZSI has high voltage gain which is obtained through switching an extra switch (Q) and continuous input current. When the switch Q is turned ON, the inverter is in the ST mode and when the switch Q is turned OFF, it is in the nST mode. The equivalent circuits of SZSI in ST and nST modes are depicted in Figure 2.6.

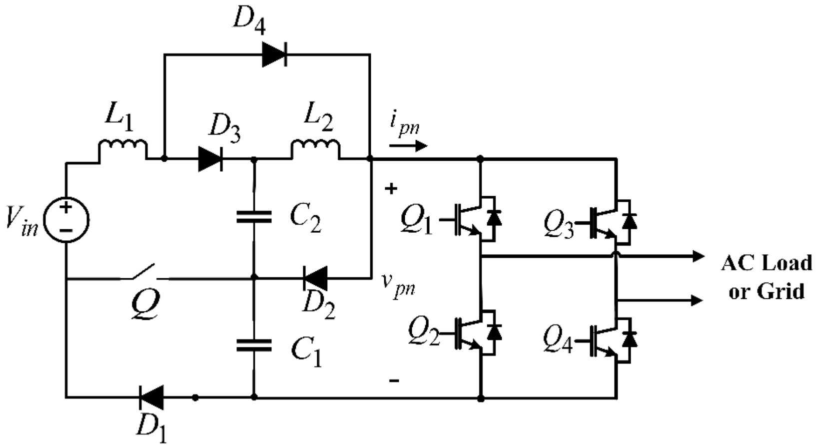

Figure 2.5: Switched-Z-source inverter (SZSI)

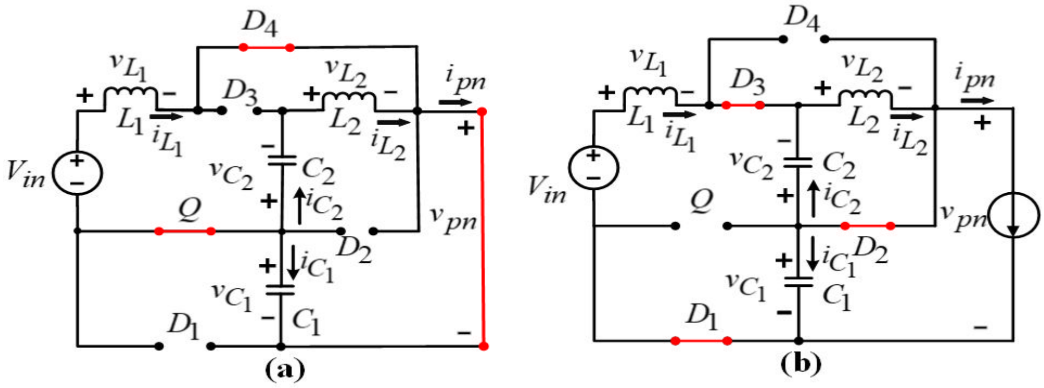

Figure 2.6: Equivalent circuit of SZSI (a) ST state (b) nST state

Same as the mentioned topologies before, L_1 and L_2 are considered equal to L and C_1 and C_2 are considered equal to C. Where all the dc side variables can be written as the addition of dc part and DFR components as $v_{C_1} = V_{C_1} + \tilde{v}_{C_1}$, $v_{C_2} = V_{C_2} + \tilde{v}_{C_2}$, $v_{pn} = V_{pn} + \tilde{v}_{pn}$, $i_{L_1} = I_{L_1} + \tilde{i}_{L_1}$, $i_{L_2} = I_{L_2} + \tilde{i}_{L_2}$.

During the ST state, when switch Q is ON, the analysis of Figure 2.6(a) yields

$$v_{L_1} = V_{in} + v_{C_1}\ ,\ v_{L_2} = v_{C_1} - v_{C_2}\ ,\ v_{pn} = 0\ , i_{C_1} = -i_{L_1} - i_{L_2}\ ,\ i_{C_2} = i_{L_2} \tag{2.16}$$

where the input dc voltage, the dc side capacitor voltages ,the dc side inductor currents and the output voltage of SZS network are denoted as V_{in} , v_{C_1}, v_{C_2} , i_{L_1} i_{L_2} and v_{pn}, respectively. During the nST state when the switch Q is OFF, the following equations can be obtained

$$v_{L_1}=V_{in}+v_{C_2}-v_{C_1} \ , \ v_{L_2}=-v_{C_2} , \ v_{pn}=v_{C_1}$$

$$i_{C_1}=i_{L_1}-i_{pn} , \ i_{C_2}=i_{L_2}-i_{L_1} \tag{2.17}$$

Meanwhile the average voltage of inductors and the mean value of the current of capacitors over one switching period is zero, hence it can be written as

$$V_{L_1}=\frac{(V_{in}+v_{C_1})T_{ST}+(V_{in}-v_{C_1}+v_{C_2})T_{nST}}{T_{sw}}=0 \tag{2.18}$$

$$V_{L_2}=\frac{(v_{C_1}-v_{C_2})T_{ST}+(-v_{C_2})T_{nST}}{T_{sw}}=0 \tag{2.19}$$

$$I_{C_1}=\frac{-(i_{L_1}+i_{L_2})T_{ST}+(i_{L_1}-i_{pn})T_{nST}}{T_{sw}}=0 \tag{2.20}$$

$$I_{C_2}=\frac{(i_{L_2})T_{ST}+(i_{L_2}-i_{L_1})T_{nST}}{T_{sw}}=0 \tag{2.21}$$

Solving (2.18)-(2.21) for v_{C_1} ,v_{C_2} , i_{L_1} and i_{L_2} yields

$$v_{C_1}=V_{in}(\frac{1}{d_{ST}{}^2-3d_{ST}+1}) \ , \ v_{C_2}=d_{ST}v_{C_1} \tag{2.22}$$

$$i_{L_1}=\frac{i_{pn}(1-d_{ST})}{(d_{ST}{}^2-3d_{ST}+1)} \ , \ i_{L_2}=i_{L_1}(1-d_{ST}) \tag{2.23}$$

where $d_{ST}=\frac{T_{ST}}{T_{sw}}$ is substituted in the equations.

According to (2.17), the output voltage of SZS network can be obtained as

$$v_{pn}=v_{C_1}=\frac{V_{in}}{(d_{ST}{}^2-3d_{ST}+1)}=BV_{in} \tag{2.24}$$

where $B = \frac{1}{(d_{ST}{}^2 - 3d_{ST} + 1)}$ is the boost factor of the SZSI. Comparing the boost factor of SZSI to the boost factor of the mentioned topologies shows that it has higher boost value.

2.5 Overview of qZSI Topologies

Numerous inverter topologies have been studied in the literature to overcome the restrictions and difficulties of the traditional voltage source, current source, traditional Z-source and quasi-Z-source inverters. Improving the reliability and performance of the power system can be accomplished via appropriate application of the impedance-source network with proper switching arrangements and topologies.

Investigating literature about the improved topologies reveals that most of them are based on improving boost factor, reducing the number or size of devices, decreasing the voltage stress on devices, improving the electromagnetic compatibility (EMC) of the system and increasing the reliability of the system.

The qZSI, which is mentioned before, is the conventional qZSI with ceaseless input current and the improved version of ZSI. It predominates ZSI due to specifications including ceaseless input current, a fewer component values and the shared earthing of the input source and dc supply.

If the input diode of the qZSI is replaced by a bidirectional switch, bidirectional qZSI (BqZSI) is created as shown in Figure 2.7 which has bidirectional power flow [57].

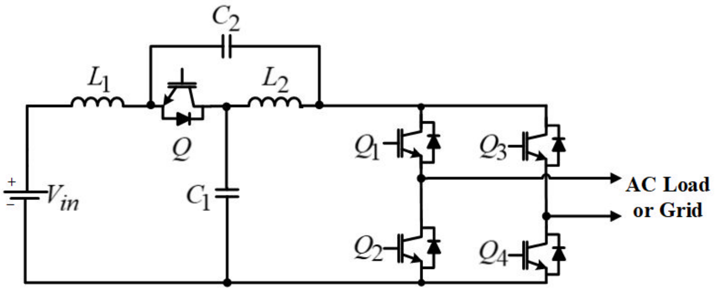

Figure 2.7: Bidirectional-quasi-Z-source inverter (BqZSI)

Although, the qZSI and BqZSI have benefits over ZSI, but they still have the same boost factor as in ZSI. Most of the studies are searching to find topologies based on qZSI to get benefit of the qZSI advantages while increasing the boost factor [58].

SL-QZSI which is presented in [59] and [60] is designed to improve the boost factor by replacing inductors of the quasi-Z-impedance with a switched inductor (SL) as shown in Figure 2.8(a). This topology achieves high boost factor while also reduced source stress and lower component rating. SCL-qZSI is also another topology presented in [61] and [62] to retain advantages of qZSI while increasing boost factor is achieved by mixture of switched-capacitor (SC) and a three-winding switched-coupled-inductor (SCL) as shown in Figure 2.8(b).

Another topology presented in this family is ASC/SL-QZSI based on the qZSI topology as shown in Figure 2.8(c) [63]. It utilizes low number of passive components with high boost factor and low voltage stress over the switches. However, the disadvantage of not sharing the neutral point among the supply source and the inverter in this topology is a significant problem.

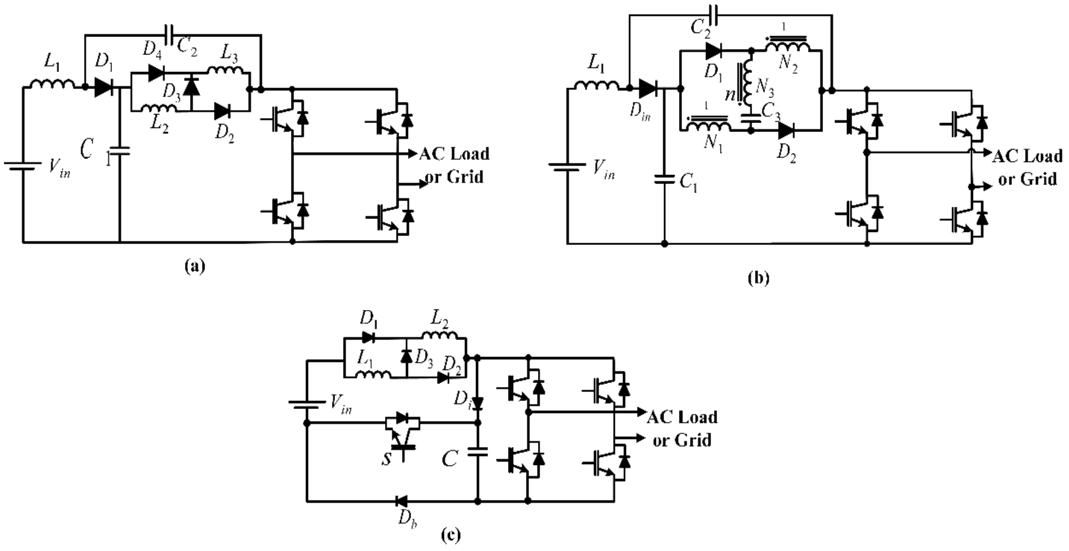

Figure 2.8: Different SL-qZSI (a) SL-qZSI (b) SCL-qZSI (c) ASC/SL-qZSI

If two inductors of qZS network are replaced by two SL cells, the new topologies can be achieved as shown in Figure 2.9(a) and 2.9(b). These topologies are named as rippled input current SL-qZSI (rSL-qZSI) and continuous input current SL-qZSI (cSL-qZSI)] [64]. Figure 2.9(c) displays the extended SL-QZSI (ESL-QZSI) topology where the SL-QZSI topology has been united with the conventional boost converter [65].

The rSL-QZSI has greater boost factor while non-continuous input current, though both rSL-QZSI and cSL-QZSI topologies have similar number of elements. The ESL-qZSI topology shown in Figure 2.9(c) is a better choice in this family since while having same components improves the boost factor and has continuous input current, but it has an active switch also.

Table 2.2 shows the different aspects of the mentioned topologies and gives obvious view to see the benefits and drawbacks of these topologies.

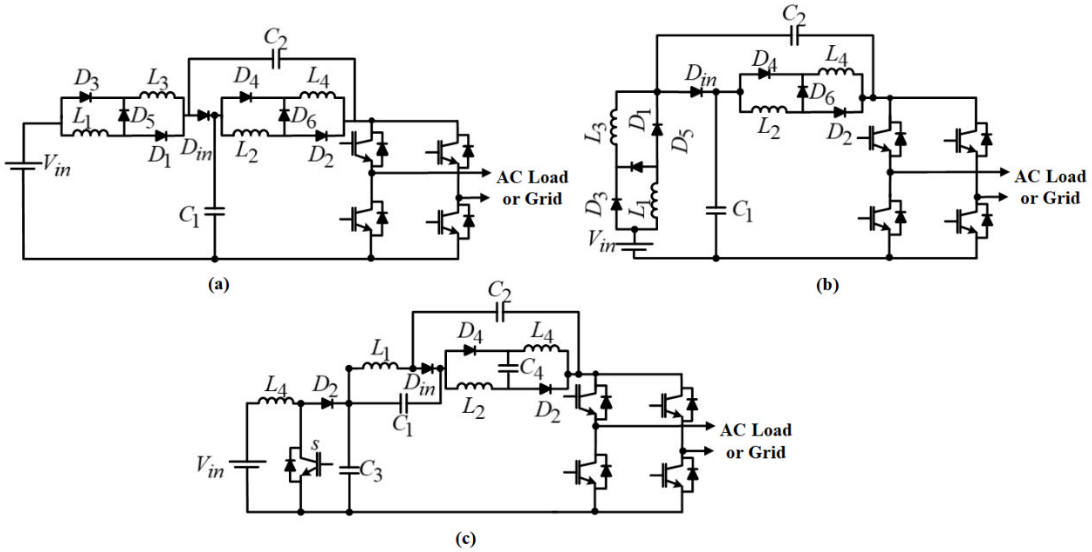

Figure 2.9: The three SL-qZSI (a) rSL-qZSI (b) cSL-qZSI (c) ESL-qZSI

Moreover, the concept of cascaded qZSI is proposed in [66]-[68] as shown in Figure 2.10 with the purpose of increasing boost factor without increasing the active devices. It can be divided to capacitor assisted (CA) and diode assisted (DA) topologies. Drawbacks such as less boost factor, more complex assembly, complex passive components plan, and big capacity make these topologies undesirable to implement.

Table 2.2: The characteristics of different topologies based on qZSI

	qZSI	SL-qZSI	SCL-qZSI	ASC/SL-qZSI	rSL-qZSI	cSL-qZSI	ESL-qZSI
Number of passive elements	2 Inductor 2 Capacitor 1 Diode	3 Inductor 2 Capacitor 4 Diode	1 Inductor 1Coupled-inductor 3 Capacitor 3Diode	2 Inductor 1Capacitor 5 Diode 1 Switch	4 Inductor 2 Capacitor 7 Diode	4 Inductor 2 Capacitors 7 Diode	4 Inductor 4 Capacitor 4 Diode 1 Switch
Continuous input current	Yes	Yes	Yes	Yes, rippled	Yes, rippled	Yes	Yes
Startup inrush current	No	No	No	No	No	No	No
Common earthing	Yes	Yes	Yes	No	Yes	Yes	Yes
Boost factor	$\frac{1}{1-2d_{ST}}$	$\frac{1+d_{ST}}{1-2d_{ST}-d_{ST}^2}$	$\frac{3}{1-4d_{ST}}$	$\frac{1+d_{ST}}{1-3d_{ST}}$	$\frac{1+d_{ST}}{1-3d_{ST}}$	$\frac{1}{1-3d_{ST}}$	$\frac{2}{(1-3d_{ST})(1-d_{ST})}$

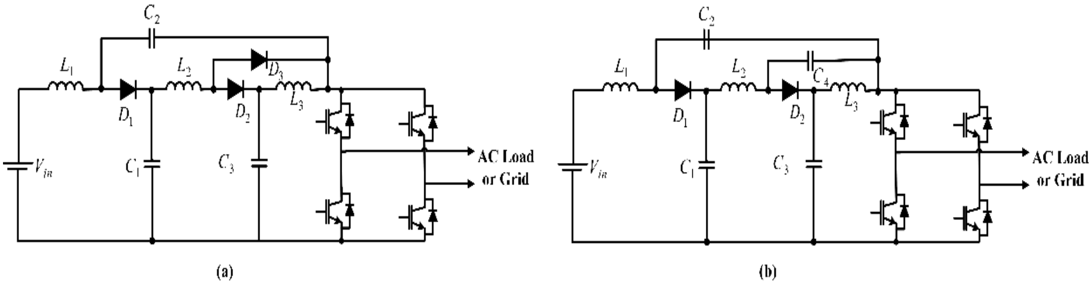

Figure 2.10: Cascaded-qZSI (a) DAC-qZSI (b) CAC-qZSI

Table 2.3 compares the different aspects of cascaded qZSIs. According to Table 2.3, DAC-qZSI has less boost factor and more elements than CAC-qZSI. However, DAC-qZSI has continuous input current despite CAC-qZSI.

Table 2.3: The characteristics of different Cascaded qZSI

	CAC-qZSI	DAC-qZSI
Number of elements	3 Inductor 4 Capacitor 2 Diode	3 Inductor 3 Capacitor 3 Diode
Continuous input current	Yes	Yes
Startup inrush current	No	No
Common earthing	Yes	Yes
Boost factor	$\frac{1}{1-3d_{ST}}$	$\frac{1}{(1-d_{ST})(1-2d_{ST})}$

If the SL cell in SL-qZSI is replaced by terminal-tapped inductor (TL) as shown in Figure 2.11, a Tapped-inductor-qZSI (TL-qZSI) is achieved [69]. This topology increases the boost factor compared to traditional qZSI while bucking the input voltage to the desired value.

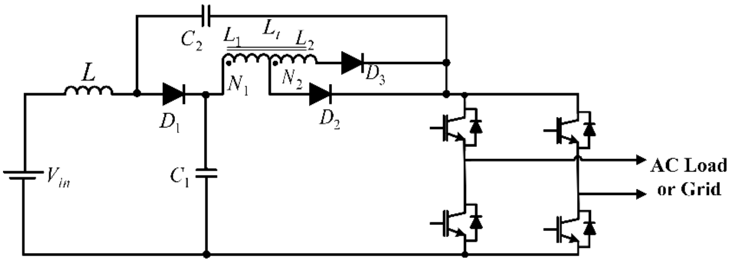

Figure 2.11: Tapped-inductor-qZSI (TL-qZSI)

Transformed based qZSI (Trans-qZSI) is also presented in [70] to improve boost ability as displayed in Figure 2.12(a). This topology reduces the number of passive elements and decreases the cost of the system. Figure 2.12(b) displays an enhanced trans-qZSI topology with ceaseless input current and low ripples, low current stress on the transformer windings and input diode and high-boost factor compared to the Trans-qZSI [71], [72]. According to Figure 2.12(c) by substituting two inductors in the traditional qZSI with two transformers, the transformer (TqZSI) is generated. This topology offeres a very high boost factor when the turns ratio of the transformer is larger than 1. If it is compared to Trans-qZSI, it uses lower transformer turns ratio which can reduce the cost by reducing weight of transformer [72]. Table 2.4 summarizes the different features of the tapped inductor and Transformer based qZSI, where n shows the transformer turns ratio, n_1 shows the first transformer turns ratio and n_2 shows the second transformer turns ratio. On the other hand, in Figure 2.11 N is the turn ratio of the tapped inductor which can be written as $N = \frac{N_2}{N_1}$.

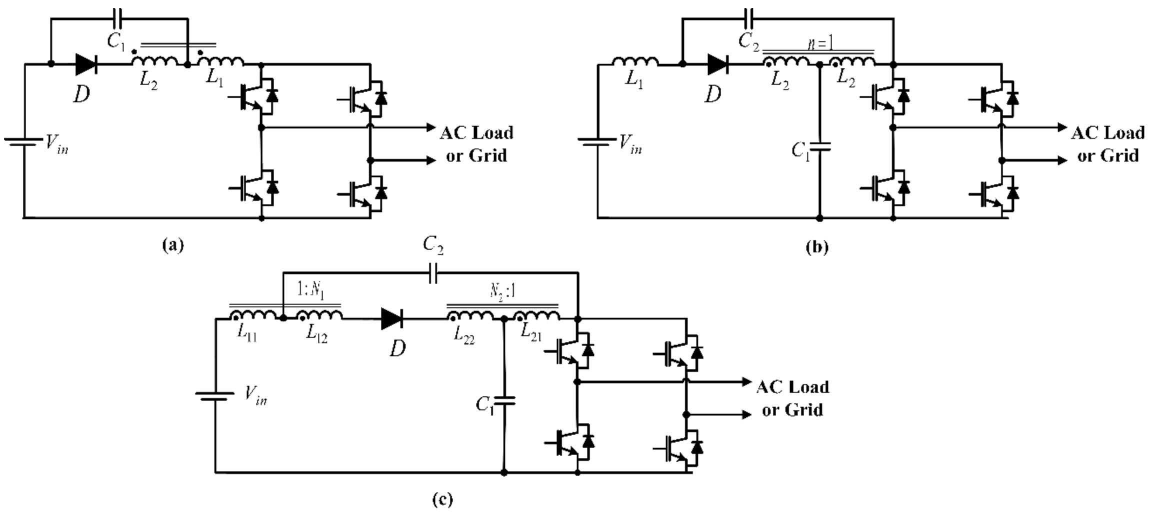

Figure 2.12: Transformed based qZSI(a) Trans-qZSI (b) Improved-Trans-qZSI (c) TqZSI

Table 2.4: The characteristics of different tapped inductor and Transformer based qZSI

	TL-qZSI	Trans-qZSI	IMPROVED TRANS-QZSI	T-QZSI
Number of passive elements	1TL cell 2Capacitor 1Inductor 3Diode	1Transformer 1Capacitor 1Diode	1Transformer 1Inductor 2Capacitor 1Diode	2Transformer 2Capacitor 1Diode
Continuous input current	Yes	Yes, High rippled	Yes	Yes
Startup inrush current	No	Yes	No	No
Common earthing	Yes	Yes	Yes	Yes
Boost factor	$\frac{1+nd_{ST}}{1-2d_{ST}-Nd_{ST}{}^{2}}$	$\frac{1}{1-(n+1)d_{ST}}$	$\frac{1}{1-(n+2)d_{ST}}$	$\frac{1}{1-(N_1+N_2+2)d_{ST}}$

2.6 Overview of qZSI Pulse Width Modulation (PWM) Techniques

Numerous PWM methods to generate gate signals of qZSI are presented in studies. The basic method is simple boost control [2]. The main difference between simple boost control and traditional sinusoidal pulse width modulation (SPWM) is that the simple boost control method uses two straight lines with opposite values for generating shoot through duty cycle. These lines can be equal or greater than the amplitude of the reference waveform (v_{ref}). When the carrier is greater than the upper line or lower than the lower line, it will generate shoot through state, else it operates like a traditional SPWM. Figure 2.13 shows the simple boost control of the qZSI. In Figure 2.13, the reference waveform (sinusoidal waveform), triangular carrier waveform and two straight lines are shown as v_{ref}, v_{car}, u_{ST} and $-u_{ST}$, respectively. The gate signals of four switches are shown as Q_1, Q_2, Q_3 and Q_4. The shoot through time is shown by dashed lines. As it is shown in this figure, the shoot-through time per switching cycle is kept constant, which yields a constant boost factor. The output voltage of single-phase inverter after filter can be written as $v_o = mV_{pn}$ where V_{pn} is the peak value of the input voltage of inverter. Thus, it can be written as

$$V_{pn} = BV_{in},\ v_o = mV_{pn} = mBV_{in} = GV_{in} \tag{2.25}$$

Thereafter, the voltage gain (G) is determined by modulation index ($m = M\sin(\omega t)$) and boost factor where ω is the frequency of the reference waveform. The maximum shoot through duty cycle (D_{ST}), boost factor (B) and voltage gain (G) with triangular carrier in terms of the amplitude of the modulation signal are given as

$$D_{ST} = 1 - M\,,\ \ B = \frac{1}{2M-1},\ G = MB = \frac{M}{2M-1} \tag{2.26}$$

In simple boost control technique, achieving bigger boost factor needs smaller M and the resultant voltage stress across the switches is high. So, there should be a tradeoff between higher boost and lower stress voltage on switches.

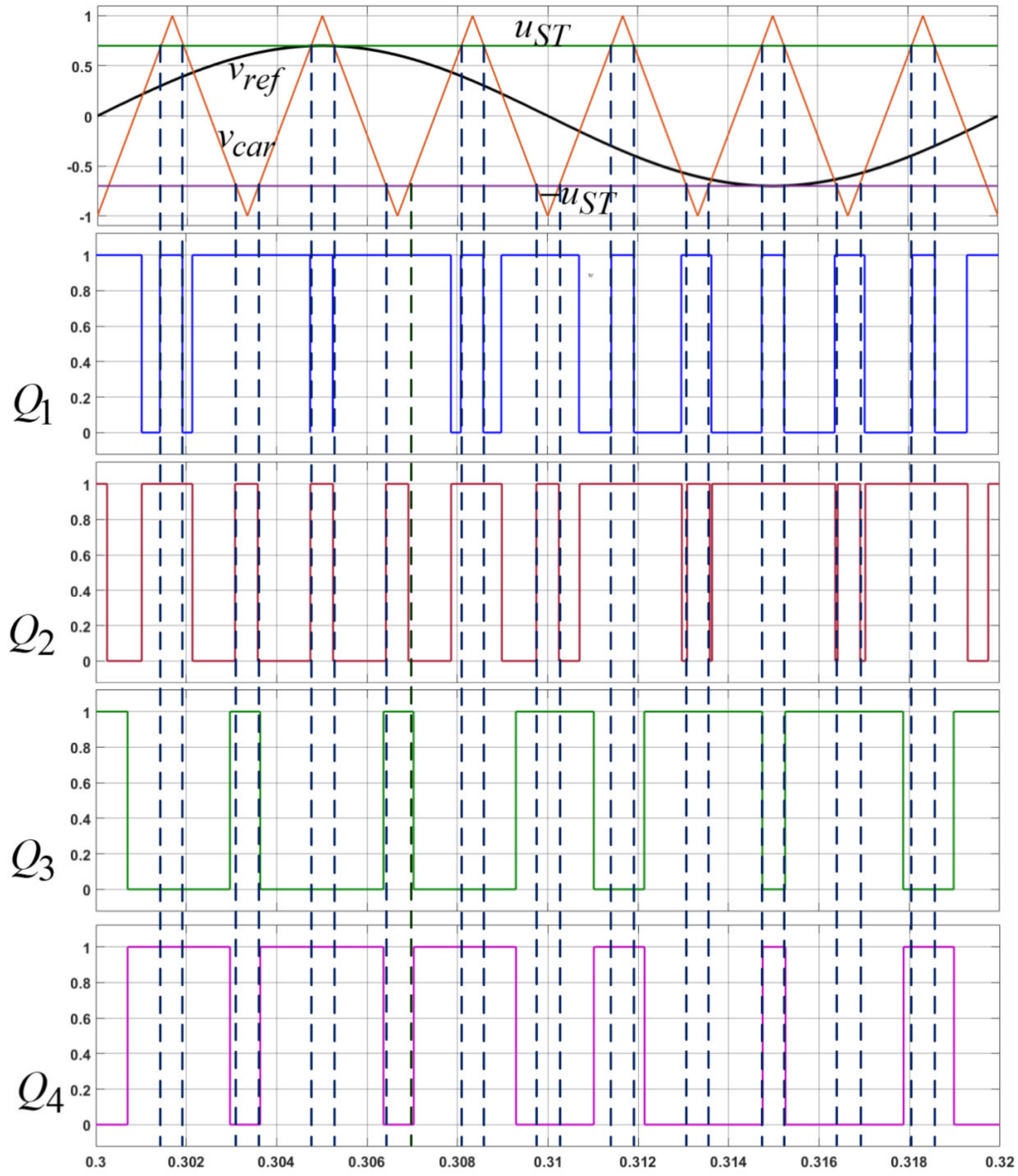

Figure 2.13: Simple boost control of single phase qZSI

A maximum boost control was presented in [73]. In this control method, all zero states change to shoot through states. It means that there will be no zero states and there will be only active states and shoot through states. In maximum boost control method, instead of using straight lines to generate shoot through duty cycles, the relation between D_{ST} and M can be written as follows:

$$B = \frac{\pi}{3\sqrt{3}M - \pi}, \quad G = MB = \frac{\pi M}{3\sqrt{3}M - \pi} \tag{2.27}$$

If this control technique is compared to the simple boost control, the operational region of maximum boost control is bigger than the simple boost and for a definite voltage gain, the modulation signal is bigger and consequently less voltage stress on the switches. However, it should be mentioned that D_{ST} has much more low frequency ripple than the simple boost control and to decrease the low ripples in inductors and capacitors, the design of the qZS impedance components will have bigger dimensions and more expensive.

The third technique is maximum constant boost control which is presented based on decreasing the low frequency ripples on the components of the qZSI [74]. To decrease the dimension and costs of the system, these ripples should be reduced. In this method by using a constant shoot through duty cycle, the low frequency ripples can be removed. Since the boost factor is determined based on the shoot through duty cycle, so to have a constant boost factor, the shoot through duty cycle should have been fixed in all switching regions and at the same time the maximum boost should be kept also. In this control method, the shoot through duty cycle and gain voltage are given as follows

$$D_{ST} = \frac{2 - \sqrt{3}M}{2}, \quad B = \frac{1}{\sqrt{3}M - 1}, \quad G = MB = \frac{M}{\sqrt{3}M - 1} \tag{2.28}$$

Maximum constant boost control method decreases the ripples existing in the maximum boost control, however the voltage stress on the switches is a little more than the maximum boost control and much less than the simple boost control method.

Chapter 3

CONTROL METHOD BASED ON THE MODEL OF THE SYSTEM FOR SINGLE-PHASE GRID-TIED qZSI

3.1 Introduction

This chapter discusses MBCC for a grid-tied quasi-Z-source inverter together with the DFR damping in the system. While the latter is performed through using the relation between the variables of the qZSI and applying the simple boost control method, a current control method with active damping and virtual time constant is employed in ac side which generates approximately sinusoidal output current with zero steady state error.

3.2 Mathematical Modeling of the system

The single-phase LCL filtered grid-tied qZSI is represented in Figure 3.1.

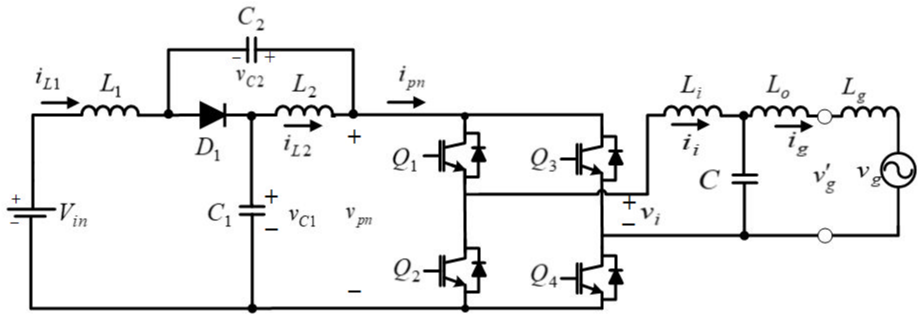

Figure 3.1: Single-phase LCL filtered grid-tied qZSI

The mathematical model of dc side and the related equations are explained in detail in Section 2.3. The boost factor and relations between the variables of qZSI are shown in equations (2.7)-(2.15). The mathematical model of ac side and the differential equations of single-phase inverter are given as follows

$$L_i \frac{di_i}{dt} + r_i i_i = uv_{pn} - v_c \tag{3.1}$$

$$L_{og} \frac{di_g}{dt} + r_{og} i_g = v_c - v_g \tag{3.2}$$

$$C \frac{dv_c}{dt} = i_i - i_g \tag{3.3}$$

where L_{og} and r_{og} can be described as $L_{og} = L_o + L_g$, $r_{og} = r_o + r_g$ and the grid voltage is considered as a sinusoidal voltage as $v_g = V_g \sin(\omega t)$, the switching function and the related resistances of the ac side inductances are described as u, r_i and r_o. The following equations show the transfer functions of I_g to I_i with and without r_{og}.

$$H_1(s) = \frac{I_g(s)}{I_i(s)} = \frac{1}{L_{og} C s^2 + r_{og} C s + 1} \tag{3.4}$$

$$H_2(s) = \frac{I_g(s)}{I_i(s)} = \frac{1}{L_{og} C s^2 + 1} \tag{3.5}$$

Figure 3.2 shows the magnitude responses of $H_1(s)$ and $H_2(s)$. It is obvious that even though r_{og} is not zero, the spike due to resonance between L_{og} and C is not zero. Therefore, alleviating such a spike is possible via using an effective damping method. On the other hand, the grid current should be forced to follow its reference which is expected to have unity power factor as follows

$$v_g = V_g \sin(\omega t) \text{ and } i_g^* = I_g^* \sin(\omega t) \tag{3.6}$$

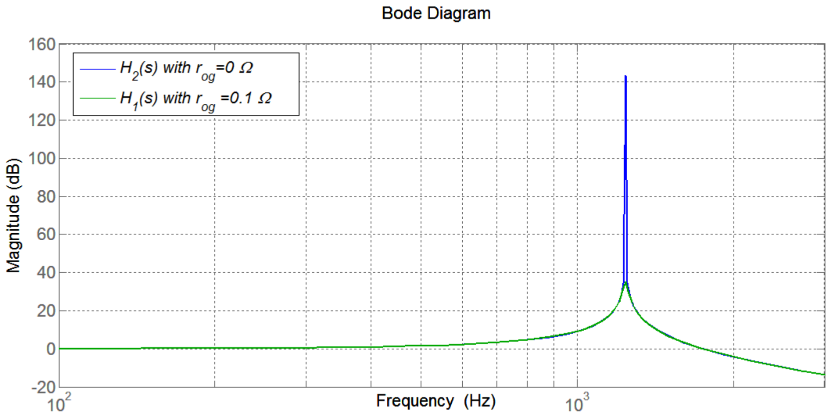

Figure 3.2: Magnitude responses of $H_1(s)$ and $H_2(s)$.

3.3 Proposed Control Approach

3.3.1 DFR Mitigation Method

According to [18], one of the methods for controlling dc side of qZSI is conventional simple method which uses PI controllers to generate the shoot through duty cycle. While the first PI controller generates $I_{L_1}^*$ by processing difference of qZS capacitor voltage and its reference ($V_{C_1}^* - V_{C_1}$), the second PI is used to generate the shoot through duty cycle (d_{ST}) by processing the inductor current and its reference. The dc side variables including current of inductors and voltage of capacitors contain DFR.

Investigating the relation between the double frequency components of inductor and capacitor voltages shows that there is a relationship between them which will be discussed in the following. Therefore, this study will get benefit of this idea and present a new PI controller as follows

$$I_{L_1}^* = K_{p1}(V_{C_1}^* - V_{C_1} - V_{L_1}) + K_{i1}\int (V_{C_1}^* - V_{C_1} - V_{L_1})dt \tag{3.7}$$

$$d_{ST} = K_{p_2}(I_{L_1}^* - I_{L_1}) + K_{i_2}\int (I_{L_1}^* - I_{L_1})dt \tag{3.8}$$

Considering the dc side capacitor voltage and inductor voltage, subtracting V_{L_1} from $V_{C_1}^* - V_{C_1}$ yields a DFR free inductor current reference. To derive the mathematical model of the proposed method, the inductor voltage is calculated in two different switching functions. First switching function is the switching time when the qSZI is in shoot-through state ($d_s = 1$), while second switching time is when qZSI is in active state ($d_s = 0$)

$$V_{L_1} = \begin{cases} V_{in} - (\bar{V}_{C_1} + \tilde{v}_{C_1}) & d_s = 0 \\ V_{in} + (\bar{V}_{C_2} + \tilde{v}_{C_2}) & d_s = 1 \end{cases} \tag{3.9}$$

where $\langle d_s \rangle_T = d_{ST}$, $\tilde{v}_{C_1}$ and $\tilde{v}_{C_2}$ are the double frequency components of the capacitor voltages, and the average values in steady-state are $\bar{V}_{C_1}$ and $\bar{V}_{C_2}$. In [18], the capacitor voltages are defined as

$$\tilde{v}_{C_1} = \tilde{v}_{C_2} = \frac{2\omega L_1}{4L_1C_1\omega^2 - (1-2d_{ST})^2} \frac{mI_i}{2} \sin(2\omega t - \phi) \tag{3.10}$$

The modulation index, peak value of i_i and phase angle between v_i and i_i are denoted as m, I_i and ϕ , respectively . The differential equations of $\tilde{i}_{L_1}$ and $\tilde{v}_{C_1}$ can be obtained as

$$L_1 \frac{d\tilde{i}_{L_1}}{dt} = (2d_{ST} - 1)\tilde{v}_{C_1} \tag{3.11}$$

$$C_1 \frac{d\tilde{v}_{C_1}}{dt} = (1 - 2d_{ST})\tilde{i}_{L_1} - (1 - d_{ST})\tilde{i}_{pn} \tag{3.12}$$

where $\tilde{i}_{pn} = -\frac{mI_i}{2(1-d_{ST})^2} \cos(2\omega t - \phi)$. Since $\tilde{v}_{C_1}$ and $\tilde{v}_{C_2}$ have same values, then equation (3.9) can be shown in compact form as

$$V_{L_1} = V_{in} + (d_s - 1)V_{C_1} + d_s V_{C\,2} + (2d_s - 1)\tilde{v}_{C_1} \tag{3.13}$$

Therefore, throughout both active and shoot through states, the input to the dc side controller can be obtained as

$$V_{C_1}^* - V_{C_1} - V_{L_1} = V_{C_1}^* - (\bar{V}_{C_1} + \tilde{v}_{C_1}) - (V_{in} - \bar{V}_{C_1} - \tilde{v}_{C_1}) = V_{C_1}^* - V_{in} \tag{3.14}$$

$$V_{C_1}^* - V_{C_1} - V_{L_1} = V_{C_1}^* - V_{in} - (\bar{V}_{C_1} + \bar{V}_{C_2} + 2\tilde{v}_{C_1}) \tag{3.15}$$

The average value of the input of the first PI over one switching time is given by

$$\left\langle V_{C_1}^* - V_{C_1} - V_{L_1} \right\rangle_T = V_{C_1}^* - \bar{V}_{C_1} - 2d_{ST}\tilde{v}_{C_1} \tag{3.16}$$

If equations (3.7) and (3.8) are written in the form of DFR components, then it gives

$$\tilde{i}_{L_1}^* = -2K_{p_1} d_{ST}\tilde{v}_{C_1} - 2K_{i_1}\int d_{ST}\tilde{v}_{C_1} dt \tag{3.17}$$

$$\tilde{d}_{ST} = -K_{p_2}(\tilde{i}_{L_1}^* - \tilde{i}_{L_1}) - K_{i_2}\int (\tilde{i}_{L_1}^* - \tilde{i}_{L_1}) dt \tag{3.18}$$

Equations (3.17) and (3.18) are derived under the assumption that $I_{L_1}^* = \bar{I}_{L_1}^* + \tilde{i}_{L_1}^*$ where $\bar{I}_{L_1}^*$ is the mean value of inductor current reference and $\bar{V}_{C_1} = V_{C_1}^*$. If the output of the second PI controller in (3.18) is divided to two parts as $d_{ST} = \bar{d}_{ST} + \tilde{d}_{ST}$, where $\bar{d}_{ST}$ is the mean value and $\tilde{d}_{ST}$ is the time-dependent constituent, then it can be shown that the shoot through duty cycle has also another part though $\tilde{d}_{ST}$ is not a double frequency ripple. Equations (3.11) and (3.12) infer that if $\tilde{d}_{ST}$ was a DFR component, then it should have been perpendicular to both $\tilde{v}_{C_1}$ and $\tilde{i}_{L1}$. Therefore, the steady state values are zero in these equations. Though, due to the orthogonality of $\tilde{v}_{C_1}$ and $\tilde{i}_{L1}$ [13], it can be inferred that $\tilde{d}_{ST}$ has components with 4ω frequencies and even various and higher frequencies over 4ω.

Equations (3.17), (3.18) in conjunction with (3.11) and (3.12) are the time-varying closed-loop equations of the qZS system. These equations are nonlinear and the only way that they can be possibly solved is the Fourier series method, whereby Fourier series of all the time-varying components with unknown amplitudes and phases could be substituted into (3.17), (3.18), (3.11) and (3.12). Then, coefficients of same-frequency sine and cosine terms are equated to obtain equations for the unknown amplitudes and phases. This procedure itself yields nonlinear equations for the unknowns and require numerical methods for their solution. Therefore, analytical treatment of the effect of the PI gains on the dynamics of the dc side seems impossible. On the other hand, close inspection of (3.18) may provide an insight into how the DFR component reduction occurs. The product $\tilde{d}_{ST}\tilde{v}_{C_1}$, with $\tilde{d}_{ST}$ comprising a 4ω component gives rise to 2ω and 6ω components. The 2ω component, through an appropriate choice of the PI gains, cancels a significant part of the 2ω component of $\tilde{v}_{C_1}$.

3.3.2 MBCC with Virtual Time Constant

Rearranging equation (3.1) and replacing i_i^* instead of i_i, yields

$$u = \frac{1}{V_{pn}}\left(L_i \frac{di_i^*}{dt} + r_i i_i^* + v_c \right) \tag{3.19}$$

where i_i^* is the reference of i_i. Equation (3.19) displays the switching function, but for improving the performance of the system, a parameter can be added to the switching function as following

$$u = \frac{1}{V_{pn}}\left(L_i \frac{di_i^*}{dt} + r_i i_i^* + v_c - K_d (i_i - i_i^*) \right) \tag{3.20}$$

The parameter K_d is introduced to control the amount of virtual time constant which in turn controls the convergence rate of the inverter current error. If (3.20) is substituted into (3.1), with the assumption that $|u| < 1$, one can obtain

$$\frac{d\Delta i_i}{dt} + \frac{\Delta i_i (r_i + K_d)}{L_i} = 0 \tag{3.21}$$

where $\Delta i_i = i_i - i_i^*$. Equation (3.21) indicates that selection of (3.20) as the switching function, (Δi_i) converges to zero in all circumstances. The time constant of decaying Δi_i to zero is given as

$$\tau_v = \frac{L_i}{r_i + K_d} \tag{3.22}$$

where τ_v is virtual time constant. Comparing τ_v while $K_d = 0$ and $K_d \neq 0$ reveals that when $K_d = 0$, τ_v is larger. Therefore K_d can be used as a tuning parameter to adjust the convergence rate of Δi_i. If i_i tracks i_i^*, equation (3.3) can be written as

$$C\frac{dv_C}{dt} + i_g = i_i^* \tag{3.23}$$

where v_C is given by

$$v_C = L_{og}\frac{di_g}{dt} + r_{og} i_g + v_g \tag{3.24}$$

Substituting (3.24) into (3.23), with the assumption that $v_g = 0$, gives

$$L_{og} C\frac{d^2 i_g}{dt^2} + r_{og} C\frac{di_g}{dt} + i_g = i_i^* \tag{3.25}$$

The s-domain transfer function which shows the relation between I_g and I_i^* can be obtained by taking Laplace transform of (3.25) as

$$H_3(s) = \frac{I_g(s)}{I_i^*(s)} = \frac{1}{L_{og}Cs^2 + r_{og}Cs + 1} \tag{3.26}$$

Comparison of (3.26) and (3.4) shows that (3.26) is not able to damp the resonance individually and requires an active damping injection.

3.4 Active Damping Injection

As it is mentioned before, due to the use of LCL filter there exists resonance between L_{og} and C as it is shown in Figure 3.2. Therefore, to damp the resonance, a virtual resistor can be used in series or in parallel with L_o and C which in turn results in four connection possibilities. Series connection is not suggested since it requires current measurement (requiring current sensor) and derivative operation. Between the parallel connection choices, parallel connection with C is chosen here because of cost reduction (requiring one voltage sensor) in comparison with the other parallel methods. After connecting the virtual damping resistor (R_d), i_i^* should be modified. Therefore, the inverter current reference can be described as

$$i_{i,damp}^* = i_i^* - \frac{v_C}{R_d} \tag{3.27}$$

Thus, i_i^* in (3.20), (3.23), and (3.25) is replaced by $i_{i,damp}^*$. Similarly, $\Delta i_i = i_i - i_i^*$ is remodified as $\Delta i_i = i_i - i_{i,damp}^*$. If i_i^* in (3.25) is replaced by $i_{i,damp}^*$ in (3.27) and taking Laplace transform of the subsequent equation yields

$$H_4(s) = \frac{I_g(s)}{I_i^*(s)} = \frac{1}{L_{og}Cs^2 + \left(r_{og}C + (L_{og}/R_d)\right)s + \left((r_{og}/R_d) + 1\right)} \tag{3.28}$$

The extra terms (L_{og}/R_d and r_{og}/R_d) in the denominator of (3.28) cause damping which can be adjusted by changing the value of R_d.

3.5 Reference Generation

For generating the reference of the output current of the inverter, the following equation can be used

$$i_i^* = L_{og} C \frac{d^2 i_g^*}{dt^2} + r_{og} C \frac{di_g^*}{dt} + C \frac{dv_g}{dt} + i_g^* \tag{3.29}$$

It is obvious that generating i_i^* requires derivative operations and also knowledge of L_{og}, r_{og} and C. Besides, the error existing in steady-state in the output current is unavoidable [30]. Instead, a proportional-resonant (PR) controller can be used to generate i_i^* as follows

$$G(s) = K_p + \frac{2K_r \omega_c s}{s^2 + 2\omega_c s + \omega^2} \tag{3.30}$$

where cut-off frequency and resonant frequency are denoted by ω_c and ω and the proportional and resonant gains are denoted as K_p and K_r, respectively. If the grid current error $(i_g^* - i_g)$ is applied to the PR controller, the output is the reference inverter current which can be written in the S-domain as follows

$$I_i^*(s) = (I_g^* - I_g)\left(\frac{K_p s^2 + 2\omega_c (K_p + K_r) s + K_p \omega^2}{s^2 + 2\omega_c s + \omega^2}\right) \tag{3.31}$$

The transfer function which shows the relation between I_g and I_g^* can be found by substituting (3.27) into (3.25), finding the Laplace transform of the resultant equation and then substituting $I_i^*(s)$ as follows

$$H_5(s) = \frac{I_g(s)}{I_g^*(s)} = \frac{K_p R_d s^2 + 2\omega_c R_d (K_p + K_r) s + K_p R_d \omega^2}{a_4 s^4 + a_3 s^3 + a_2 s^2 + a_1 s + a_0} \tag{3.32}$$

where

$$b_0 = \omega^2 (r_{2g} + K_p R_C^p + R_C^p)$$

$$a_1 = \omega^2 (r_{og} R_d C + L_{og}) + 2\omega_c r_{og} + 2\omega_c R_d (K_p + K_r + 1)$$

$$a_2 = \omega^2 R_d L_{og} C + r_{og} + 2\omega_c (r_{og} R_d C + L_{og}) + R_d (K_p + 1)$$

$$a_3 = L_{og} (2\omega_c R_d C + 1) + r_{og} R_d C$$

$$a_4 = R_d L_{og} C$$

Since in steady state the output current of the inverter tracks its reference ($i_i = i_{i,\, damp}^{*}$), thus the degree of $H_5(s)$ is decreased by one. On the other hand, since the proposed control approach is implemented in discrete-time, the frequency response of $H_5(s)$ is formulated in discrete time. In order to apply delay effect to the system, one-sampling period delay is considered to the control method as shown in (3.20). It is worth mentioning that because the controller delay is less than one sampling period, the discretized transfer function signifies the worst case of this delay.

Figure 3.3 shows the Bode diagram (magnitude) of discretized transfer function inspecting the effect of delay via using the values given in Table 3.1 with various R_d values. Choosing $R_d = 3\Omega$ leads to a satisfactory damping, in both delay and no delay conditions, while increasing R_d worsens damping. On the other hand, this figure shows that the magnitude of $H_5(s)$ is zero at 50 Hz which means that the error in the grid current is zero in all operating conditions.

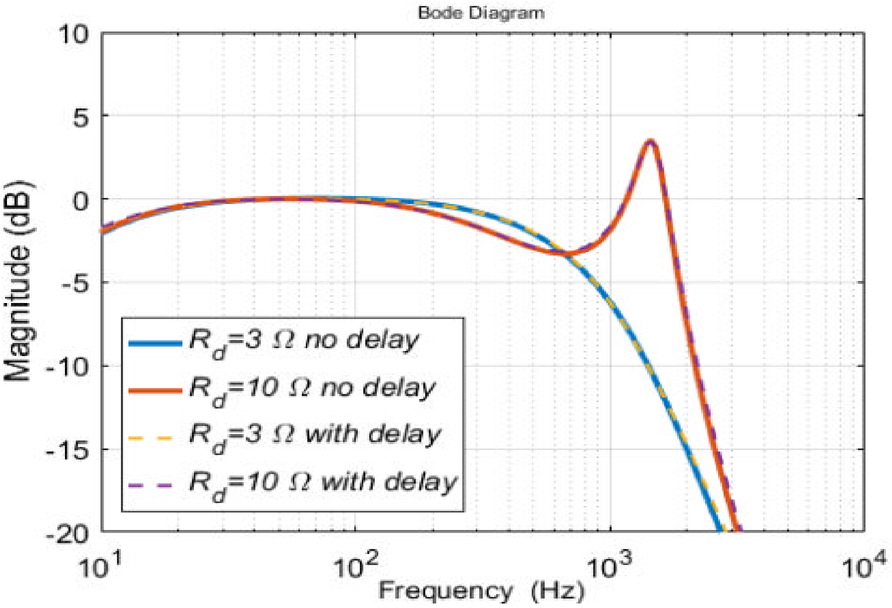

Figure 3.3: Magnitude responses of discretized $H_5(s)$ with and without delay under different R_d values

3.6 Root-Loci and Robustness

3.6.1 Root-Loci

Figure 3.4 shows the loci of the poles while varying R_d , K_p, and. The root-loci is obtained by changing one parameter while other parameters are kept constant. Obviously, increasing R_d enforces all poles approaching the unit circle limit. The square-dotted line in Figure 3.4(a) shows the consequence of increasing R_d which in turn leads to instability and taking poles out of the boundary of the unit circle. It is worth mentioning that one real pole is not shown in the figure because it is not affected by the variation of R_d . Increasing K_p leads to convergence of one of the poles near the unit circle limit while the other poles diverge from the unit circle limit.

Furthermore, once K_r is changed, one of the complex-conjugate pairs of poles approaches the unit circle limit while the other pair approach the real axis as shown in

Figure 3.4(b). Therefore, increasing K_r too much slows down the transient response and may endanger instability. So, there is a trade-off among the transient response and stability while choosing K_r value. The regulation of PR gains based on rational method is hard because of the fourth-order transfer function in equation (3.32). However, by tracking the movement of poles, the variations of the PR controller gains can be inspected.

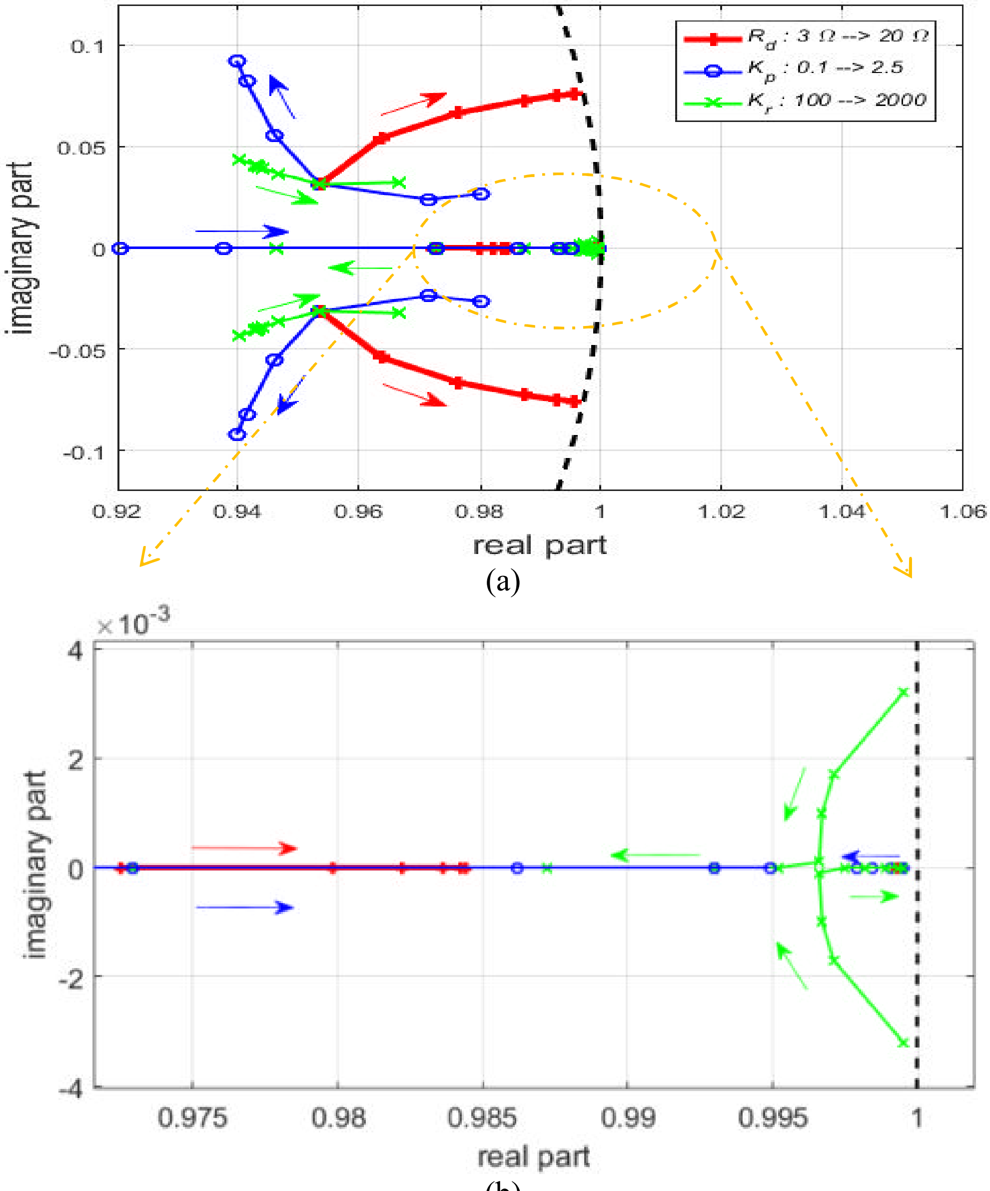

(a)

(b)

Figure 3.4: (a) The loci of closed-loop poles obtained with no delay when R_d , K_p , and K_r are varied. (b) Magnified view of the poles around unit circle boundary.

Increasing R_d from 3Ω to 20Ω under delay is inspected in Figure 3.5. Investigating variations in R_d with and without delay is possible by comparing Figure 3.4 and Figure 3.5. Obviously, an extra pole is added to the control loop, while the routes of poles in both cases are fairly the same.

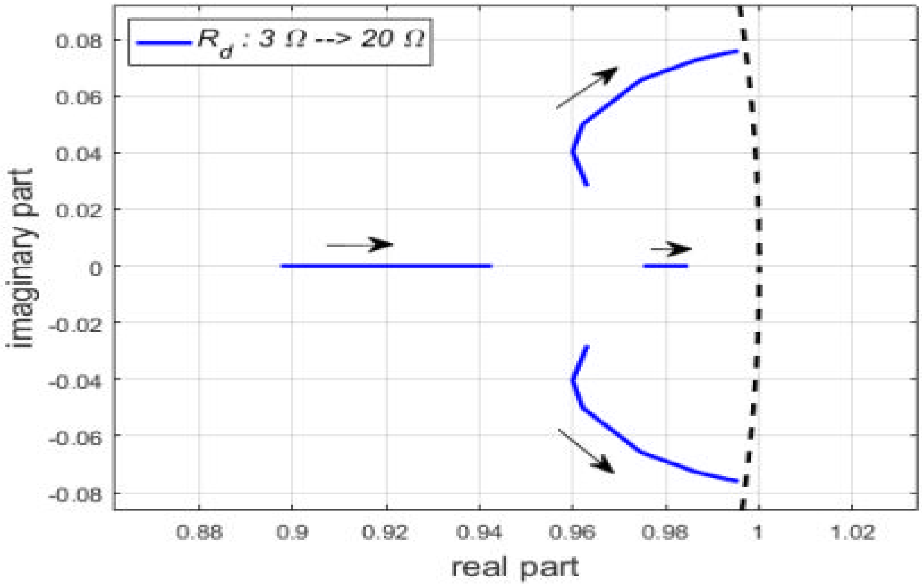

Figure 3.5. The loci of closed-loop poles obtained under one-sample delay when R_d is changed from $3\,\Omega$ to $20\,\Omega$ while K_p and K_r are kept constant

3.6.2 Robustness

To shorten the study in this part, the inductor resistance is neglected deliberately. Since $\hat{L}_i$ is the estimated inductance in (3.20), the switching function in (3.20) can be defined as follows

$$u = \frac{1}{V_{pn}}\left(\hat{L}_i \frac{di^*_{i,damp}}{dt} + v_c - K_d(i_i - i^*_{i,damp}) \right) \tag{3.33}$$

Substituting (3.33) in (3.1) and replacing $i^*_{i,damp}$ with (3.27) gives

$$L_i \frac{di_i}{dt} + \frac{\hat{L}_i}{R_d}\frac{dv_c}{dt} + K_d i_i + \frac{K_d v_c}{R_d} = \hat{L}_i \frac{di_i^*}{dt} + K_d i_i^* \tag{3.34}$$

As it is mentioned before, i_i^* is generated via PR controller. The real values of i_i and v_C can be given as

$$i_i = L_{og} C \frac{d^2 i_g}{d^2 t} + C \frac{dv_g}{dt} + i_g \tag{3.35}$$

$$v_C = L_{og} \frac{di_g}{dt} + v_g \tag{3.36}$$

Substituting (3.35) and (3.36) into (3.34), taking Laplace transform of the resultant equation, and replacing $I_i^*(s)$ with (3.31) yields the transfer function showing the relation between I_g and I_g^* that can be obtained as

$$H_6(s) = \frac{I_g(s)}{I_g^*(s)} = \frac{b_3 s^3 + b_2 s^2 + b_1 s + b_0}{c_5 s^5 + c_4 s^4 + c_3 s^3 + c_2 s^2 + c_1 s + c_0} \tag{3.37}$$

where

$b_0 = \omega^2 K_p K_d$, $b_1 = \omega^2 K_p \hat{L}_i + 2\omega_c K_d (K_p + K_r)$, $b_2 = 2\omega_c \hat{L}_i (K_p + K_r) + K_p K_d$

$b_3 = \hat{L}_i K_p$, $c_0 = \omega^2 K_d (K_p + 1)$, $c_1 = \omega^2 (L_i + \hat{L}_i K_p + K_d L_{og}) + 2\omega_c K_d (K_p + K_r + 1)$

$c_2 = \omega^2 L_{og} (K_d C + \hat{L}_i / R_d) + 2\omega_c (L_i + K_p \hat{L}_i + K_r \hat{L}_i + K_d L_{og} / R_d) + K_d (K_p + 1)$

$c_3 = \omega^2 L_i L_{og} C + L_i + \hat{L}_i K_p + 2\omega_c L_{og} (\hat{L}_i / R_d + K_d C) + K_d L_{og} / R_d$

$c_4 = 2\omega_c L_i L_{og} C + K_d L_{og} C + \hat{L}_i L_{og} / R_d$

$c_5 = L_i L_{og} C$

The Bode diagram (magnitude) of the equation (3.37) is displayed in Figure 3.6. For inspecting the effect of parameter variation on the robustness of the system, $\hat{L}_i$ is changed for three different values in this Figure ($\hat{L}_i = 1.35\text{ mH}, 1.275\text{ mH}, 1.2\text{ mH}$). The results show that the magnitude response in 50 Hz is zero in all conditions. It means that the presented control method is robust to the parameter variations.

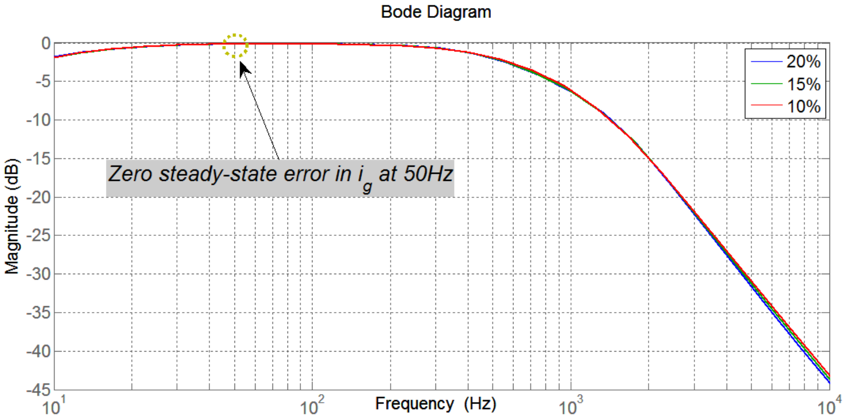

Figure 3.6: Magnitude response of $H_6(s)$ with different values of $\hat{L}_i$.

3.7 Experimental Verification

The efficiency of the proposed control method depicted in Figure 3.7 is validated by manipulating the control method on a 3.12kW system. The system and control parameters are given in Table 3.1 and Table 3.2, respectively. For realizing the control approach on the system, the high-performance advanced platform OPAL-RT Wanda controller is used and for building the single-phase inverter prototype the Genesic GB100XCP12 IGBT modules and Avago ACPL-332J gate drivers are used. LEM LA100-P and LV 25-P are used for sensing the voltage and current signals, respectively and the power source for input is supplied through KeySight programmable power supply. It is worth mentioning that the appeared noises on V_{L_1} while measuring have no effect on the control approach as can be seen in experimental results.

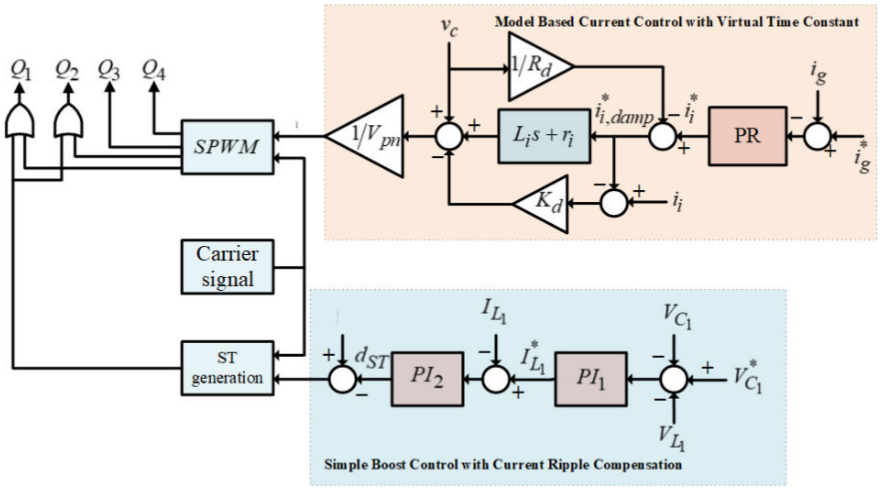

Figure 3.7. Block diagram of the proposed control method.

Figure 3.8 shows all the variables of the qZSI with and without DFR compensation in (a) and (b) parts when r_g and L_g are included in the grid for $V^*_{C_1} = 400\,V$ and $I^*_g = 10\,A$. The DFR existing in dc side variables is obvious in Figure 3.8(a) which is obtained without compensation method. Nevertheless, when the DFR mitigation method is applied, the DFR is removed in I_{L_1} as demonstrated in Figure 3.8(b). To calculate the qZSI boost factor, the average value of output voltage of the qZS network (V_{pn}) which is (550V) is divided over the input voltage which results in that boost factor is approximately $B = 2.2$. According to (2.12), the shoot through duty cycle can be calculated as $d_{ST} = 0.273$. Substituting the shoot through duty cycle into (2.11) results in $V_{C_1} = 400\,V$ and $V_{C_2} = 150\,V$ which shows good agreement between the theory and experimental results. Furthermore, while V_{C_1} tracks its reference, the grid current is sinusoidal with unity power factor that verifies the feasibility of the control methodology in controlling the entire system successfully.

Table 3.1: The system parameters

System Parameters	**Value**
Virtual resistor (R_d)	3Ω
Input voltage (V_{in})	250 V
qZS inductors ($L_1 = L_2$)	$2.5\,\text{mH}$
qZS capacitors($C_1 = C_2$)	$1000\,\mu F$
Filter input inductor and resistor (L_i, r_i)	$1.5\,\text{mH}, 0.2\,\Omega$
Filter capacitor (C)	$22\ \mu F$
Filter output inductor and resistor (L_o, r_o)	$0.5\,\text{mH}, 0.08\,\Omega$
Grid inductor and resistor (L_g, r_g)	$0.25\,\text{mH},\ 0.02\,\Omega$
Grid voltage and frequency (V_g, f_g)	$220\sqrt{2}\,V$, $50\,\text{H}z$
Switching frequency (f_{sw})	$12.5\,\text{kHz}$

Table 3.2: The control parameters

Control Parameters	**Value**
K_d	10
K_p	0.5
K_r	1500
ω_c	1 rad/s
K_{p1}	0.07
K_{p2}	0.1
K_{i1}	0.5
K_{i2}	20

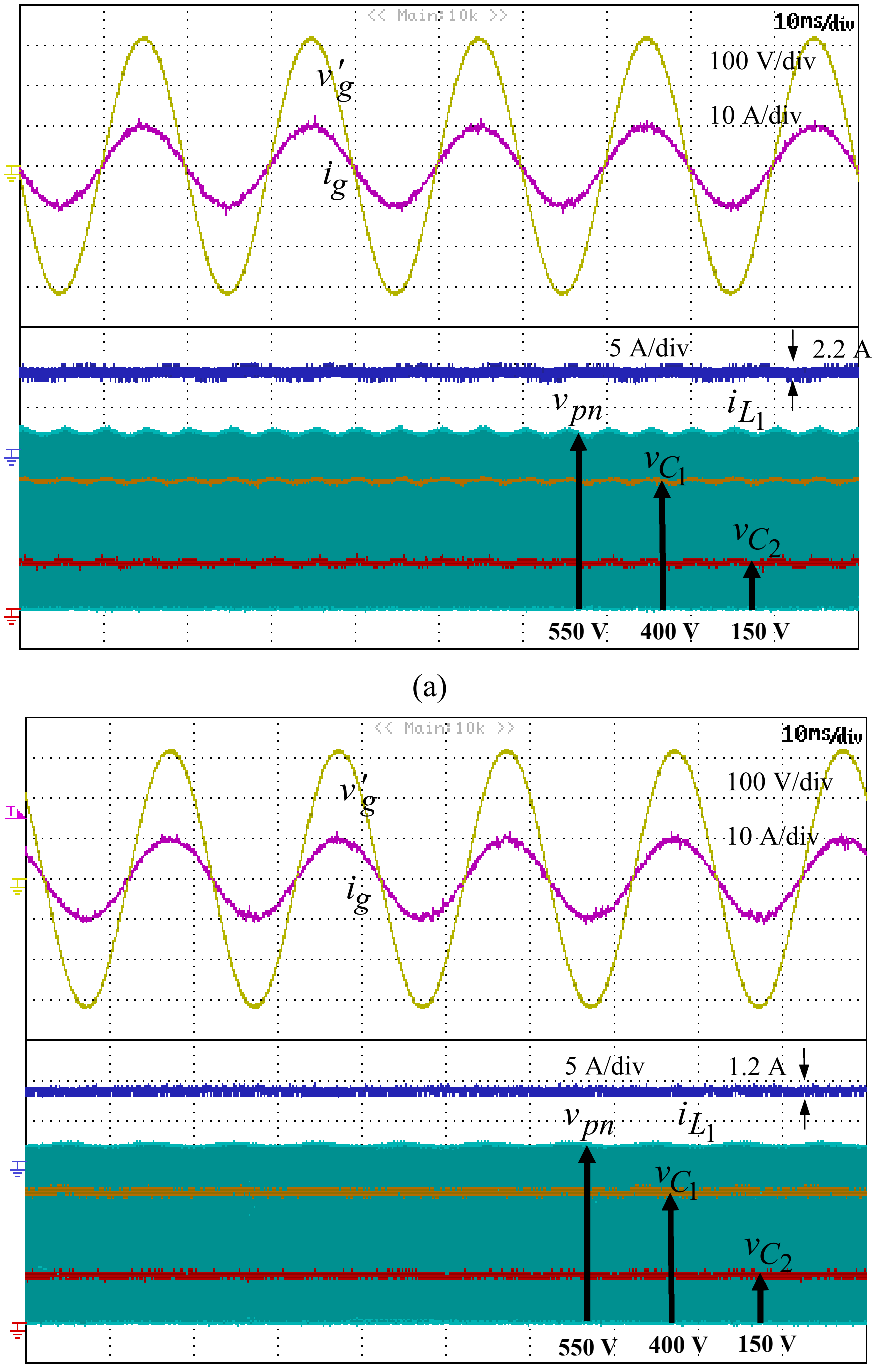

(b)

Figure 3.8: Experimental results of the system variables when r_g and L_g are applied ($V_{C_1}^* = 400V$, $I_g^* = 10A$, $L_1 = L_2 = 2.5\,\mathrm{m}H$) (a) Without DFR mitigation, (b) With DFR mitigation

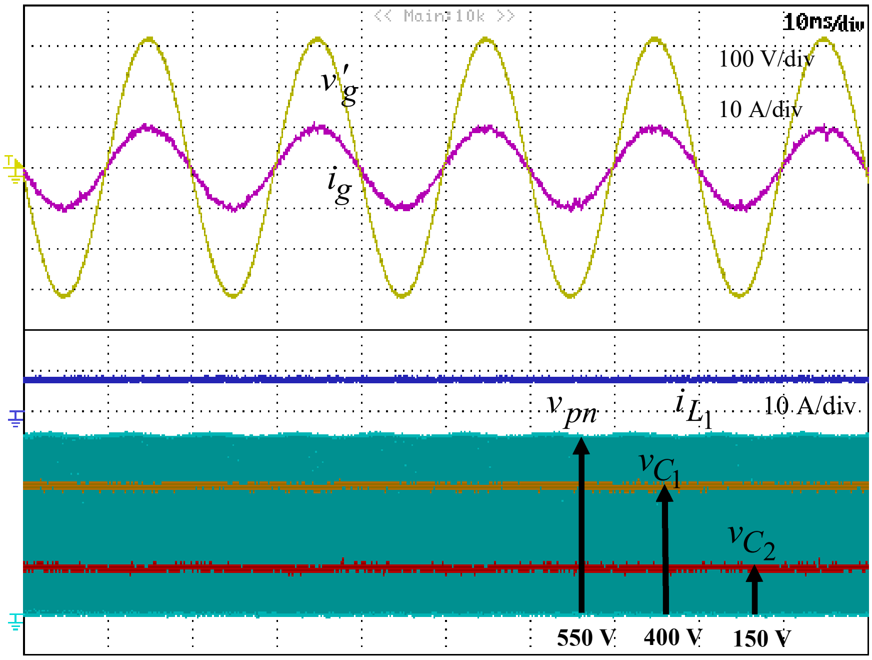

Figure 3.9: Experimental results of the entire system variables when r_g and L_g are zero ($V_{C_1}^* = 400\,V$, $I_g^* = 10\,A$, $L_1 = L_2 = 2.5\,mH$).

The experimental results of dc and ac side variables in steady-state while mitigation of double frequency ripple is enabled when r_g and L_g are zero, is shown in Figure 3.9. Clearly, even ignoring the grid inductance does not affect the performance of the proposed control method.

The total harmonic distortion (THD) of the grid currents related to Figure 3.8(b) and Figure 3.9 are shown in Figure 3.10. The THD is measured as 2.6% and 2.8%, without and with r_g and L_g, respectively. These values are in acceptable ranges according to the standards [76]. The responses of all of the variables of the system are investigated when the values of the dc side inductors are decreased from $2.5\,\mathrm{mH}$ to $1\,\mathrm{mH}$ as shown in Figure 3.11. Obviously, it can be shown that the DFR does not exist in both situations even while reducing the inductor values.

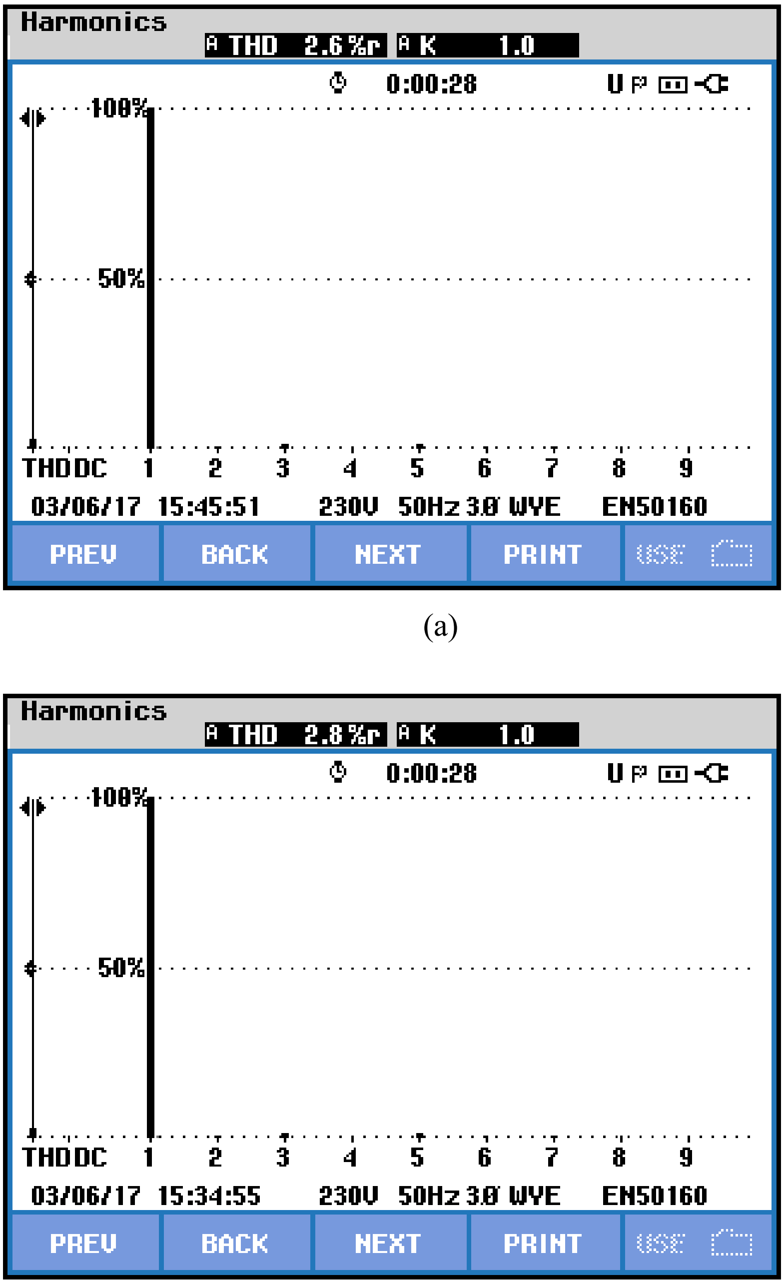

(a)

(b)

Figure 3.10: Harmonic spectrum of i_g when: (a) r_g and L_g are present, (b) r_g and L_g are zero.

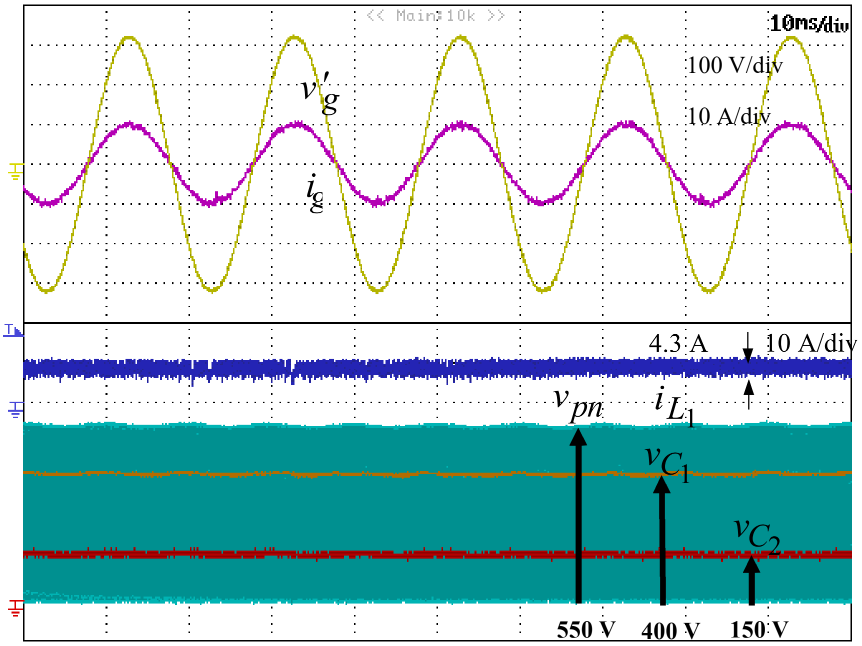

Figure 3.11: Experimental results of the system variables with DFR compensation when r_g and L_g are present ($L_1 = L_2 = 1\text{m}H$)

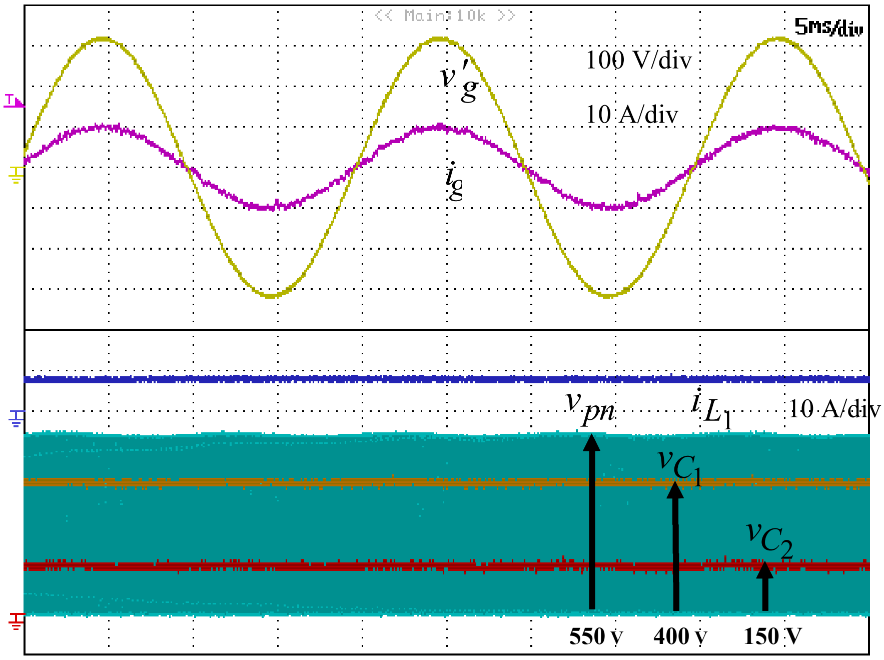

Figure 3.12: Experimental results of the system variables when $\hat{L}_i$ is different from L_i by 10% ($\hat{L}_i = 1.35\,\text{m}H$)

The performance of the closed-loop system, when $\hat{L}_i$ deviates from L_i by 10% ($\hat{L}_i = 1.35\,\text{mH}$) is investigated as shown in Figure 3.12. Even with 10% error in $\hat{L}_i$, the performance is not affected by this parameter mismatch.

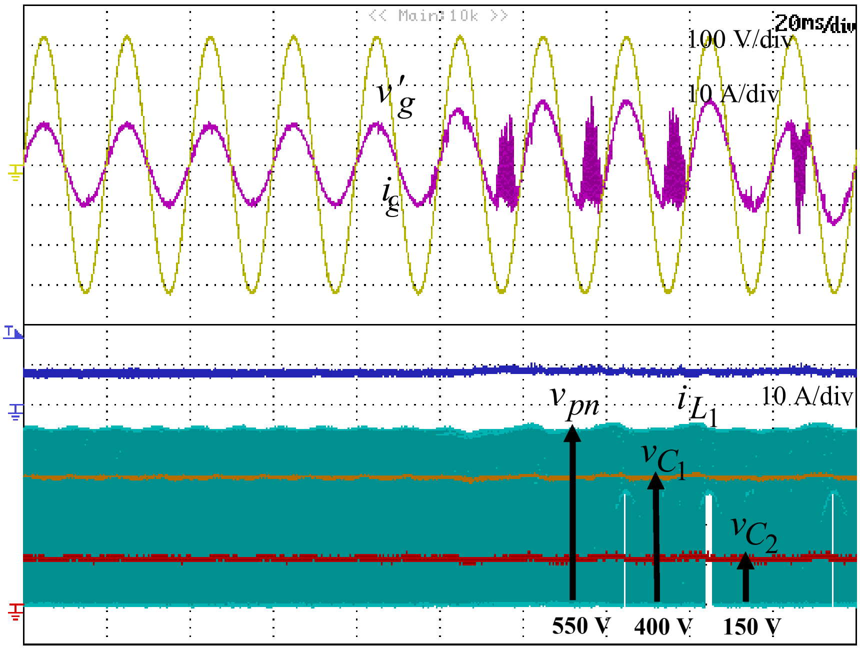

Figure 3.13: Experimental results of the system variables for a sudden variation in R_d from $3\,\Omega$ to $10\,\Omega$

The behavior of the system is investigated during an abrupt change in R_d from 3Ω to 10Ω in Figure 3.13. The experimental responses of dc and ac side variables in the steady-state during the sudden change are shown in this figure. When R_d is increased to 10Ω, the performance of the system is deteriorated. This effect demonstrates that when $R_d = 10\Omega$ the damping is unacceptable in accordance to the closed loop poles location in Figure 3.5. The behavior of the system while varying K_d from 10 to 0 is investigated in Figure 3.14. The performance of closed-loop system is extremely disturbed when K_d is ignored ($K_d=0$). But obviously the closed loop system performs perfectly for $K_d=10$.

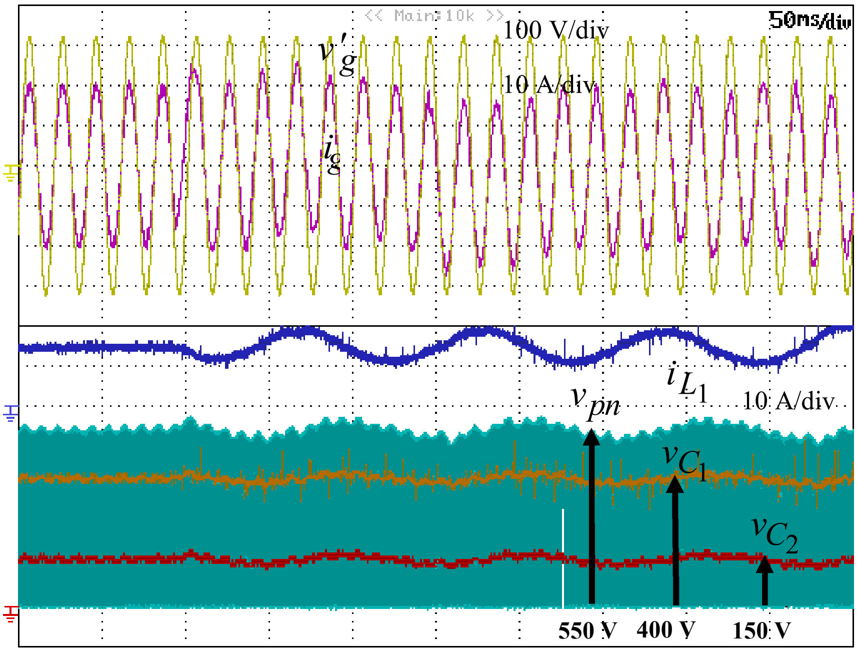

Figure 3.14: Experimental results for the system variables for a sudden variation in K_d from 10 to 0.

The dynamic responses of all variables of the qZSI while experiencing an abrupt change in the grid current reference is inspected in Figure 3.15. the grid current reference is varied from 10A to 20A as it is shown in this Figure. Perceptibly, the entire variables track the desired references after the sudden variation in I_g^*. The fast tracking behavior of i_g with no overshoot is explicit, though the settling time of I_{L_1} and v_{pn} is nearly 7ms. Since I_{L_1} is forced to vary its value due to the change in grid current, I_{L_1} encounters an overshoot which is counted to be 14.3%. However, v_{pn} preserves its previous value after the variation.

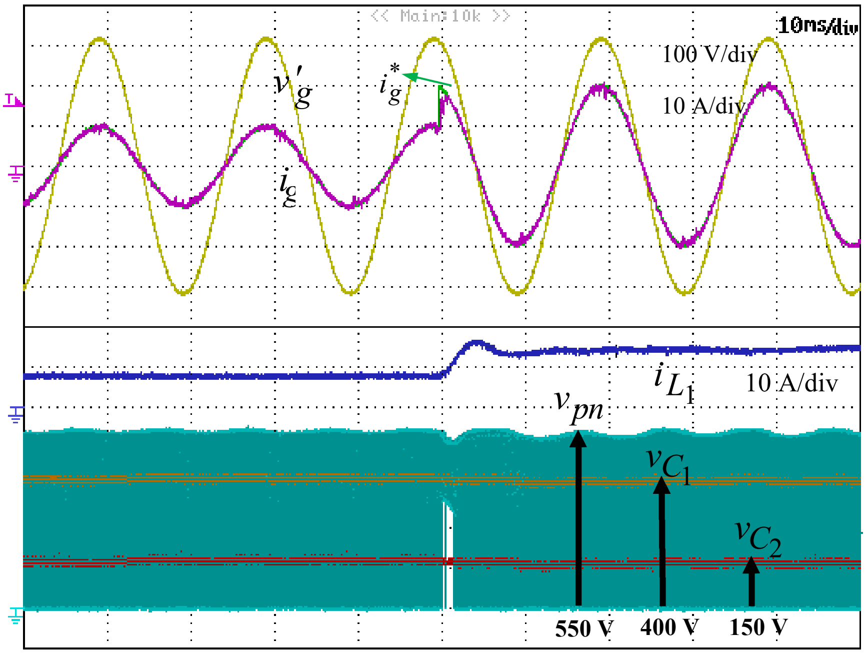

Figure 3.15: Dynamic responses of the system variables for a sudden variation in I^*_g from 10A to 20A.

3.8 Conclusion

This chapter proposes a MBCC method for the single-phase grid-tied qZSI with LCL filter. While the presented methodology, regulates the injected current to the grid with active damping and virtual time constant, it has also the feature of compensating the DFR existing in dc side inductor current of the qZSI. The DFR mitigation is performed through using the relation between the variables of the qZSI and applying the simple boost control method. The effectiveness of the proposed method is validated through experimental results.

Chapter 4

MULTI INPUT MULTI OUTPUT BASED SLIDING MODE CONTROL OF qZSI

4.1 Introduction

The qZSI is a multi-input multi-output (MIMO) nonlinear system which makes it a challenging structure for close loop control. In this chapter, a MIMO sliding mode control (SMC) approach to control all the variables of a single-phase qZSI is presented. Different from the recent SMC approaches, the proposed control approach not only synchronizes the control of all state variables for qZSI, but also achieves the control of all the system variables.

The theory of boundary layer is utilized to smooth the sliding functions in a boundary layer and make them appropriate for the PWM process. The smoothing process converts the discontinuous control signal to continuous signal which can be compared with a triangular carrier to generate PWM signals leading to the fixed switching frequency. The validity of the proposed SMC is investigated by providing simulation and experimental results in standalone mode and simulation results for grid-connected mode.

4.2 Standalone Mode

4.2.1 State Space Modeling of Standalone qZSI

Figure 4.1 represents a single-phase qZSI connected to a load through an LC filter.

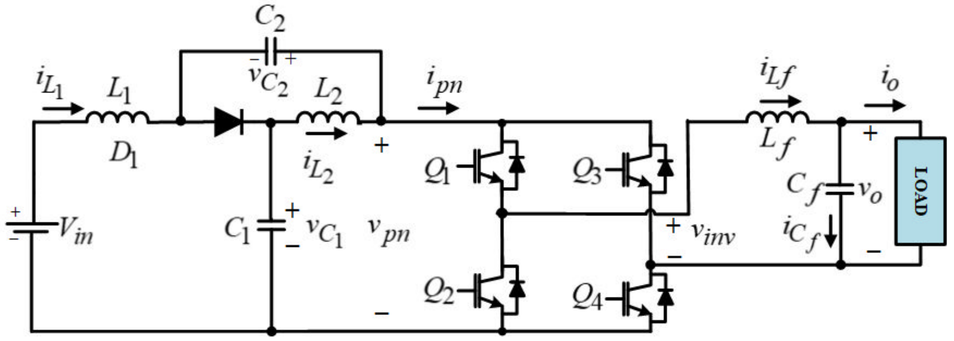

Figure 4.1: Single-phase qZSI with LC filter.

When the qZSI is controlled by modulation signal $m = M \sin \omega t$, where ω is the fundamental angular frequency of the output voltage, the filtered output voltage yields

$$v_o = m v_{pn} \tag{4.1}$$

If the power balance equation of the whole system is written and (4.1) is substituted in this equation, the following relation can be obtained [18]:

$$v_{pn} i_{pn} (1 - d_{ST}) = v_o i_o = m v_{pn} i_o \tag{4.2}$$

where d_{ST} is the shoot-through duty cycle described as $d_{ST} = \frac{T_{ST}}{T_{sw}}$ in terms of the switching time (T_{sw}) and shoot through time (T_{ST}). Arranging (4.2) gives

$$i_{pn} (1 - d_{ST}) = m i_o \text{ (4.3)} \tag{4.3}$$

Assuming $L_1 = L_2 = L$ and $C_1 = C_2 = C$, the order of qZS system can be decreased. Furthermore, the qZS network variables can be written as the addition of dc part and DFR component as $v_{C_1} = V_{C_1} + \tilde{v}_{C_1}$, $v_{C_2} = V_{C_2} + \tilde{v}_{C_2}$, $i_{L_1} = I_{L_1} + \tilde{i}_{L_1}$, $i_{L_2} = I_{L_2} + \tilde{i}_{L_2}$, and $v_{pn} = V_{pn} + \tilde{v}_{pn}$. Figure 4.2 shows the equivalent model of the standalone mode qZSI in ST and nST states.

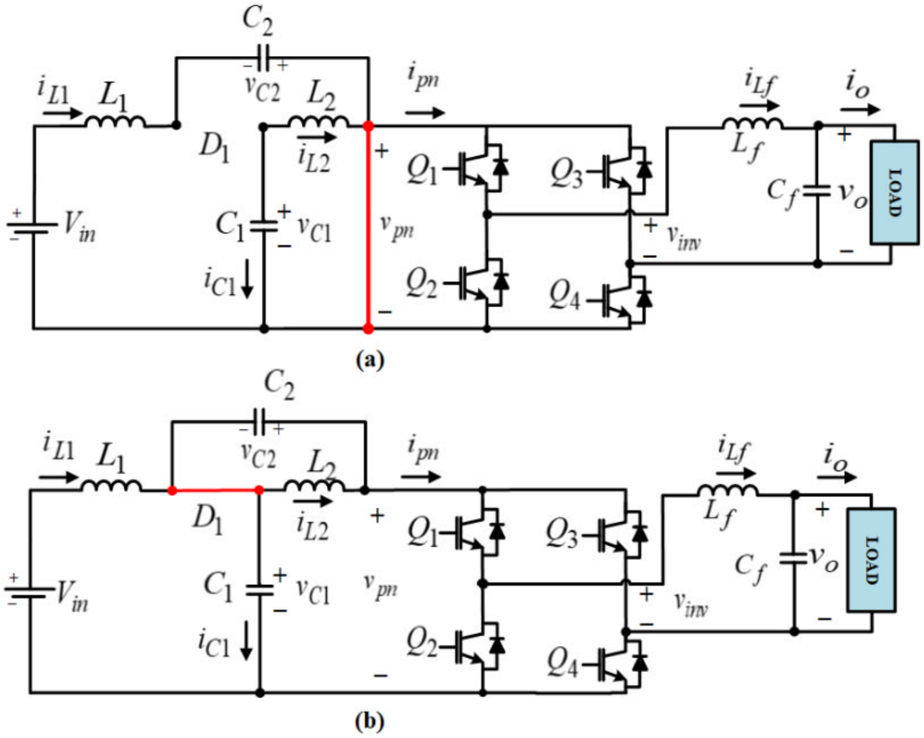

Figure 4.2: Equivalent circuit of the standalone qZSI in: (a) ST state (b) nST state.

According to Figure 4.2(a), during the ST state, the inverter is short-circuited. Applying Kirchhoff's laws yields

$$L\frac{di_{L_1}}{dt} = V_{in} + v_{C_1} - (r_L + r_C)i_{L_1} \tag{4.4}$$

$$C\frac{dv_{C_1}}{dt} = -i_{L_2} \tag{4.5}$$

$$L_f\frac{di_{Lf}}{dt} = -r_f i_{Lf} - v_o \tag{4.6}$$

Likewise, according to Figure 4.2(b), in the nST state, the equations can be written as

$$L\frac{di_{L_1}}{dt} = V_{in} - v_{C_1} - (r_L + r_C)i_{L_1} + r_C i_{pn} \tag{4.7}$$

$$C\frac{dv_{C_1}}{dt}=i_{L_1}-i_{pn} \tag{4.8}$$

$$L_f\frac{di_{Lf}}{dt}=-r_f i_{Lf}+v_{inv}-v_o \tag{4.9}$$

where r_L and r_C are the internal resistances of the inductor and capacitor of the qZSI, respectively. The averaged model of the qZSI in one switching period can be obtained by combining (4.4) –(4.9) as follows

$$L\frac{di_{L_1}}{dt}=d_{ST}(V_{in}+v_{C_1}-(r_L+r_C)i_{L_1})+(1-d_{ST})(V_{in}-v_{C_1}-(r_L+r_C)i_{L_1}+r_C i_{pn}) \tag{4.10}$$

$$C\frac{dv_{C_1}}{dt}=d_{ST}(-i_{L_2})+(1-d_{ST})(i_{L_1}-i_{pn}) \tag{4.11}$$

$$L_f\frac{di_{Lf}}{dt}=d_{ST}(-r_f i_{Lf}-v_o)+(1-d_{ST})(-r_f i_{Lf}+v_{inv}-v_o) \tag{4.12}$$

Rearranging equations (4.10)-(4.12) and substituting (4.1) and (4.3) in the resultant equations yields

$$L\frac{di_{L_1}}{dt}=d_{ST}(2v_{C_1}-V_{in})+V_{in}-v_{C_1}-(r_L+r_C)i_{L_1}+mr_C i_o \tag{4.13}$$

$$C\frac{dv_{C_1}}{dt}=i_{L_1}-2d_{ST}i_{L_1}-mi_o \tag{4.14}$$

$$L_f\frac{di_{Lf}}{dt}=-r_f i_{Lf}+(1-d_{ST})v_{inv}-m(2v_{C_1}-V_{in}) \tag{4.15}$$

Considering d_{ST} and m as the control inputs of the system and rearranging equations (4.13)-(4.15), the state-space model of the single-phase qZSI in matrix form can be written as follows

$$\begin{bmatrix} L\dfrac{di_{L_1}}{dt} \\ C\dfrac{dv_{C_1}}{dt} \\ L_f\dfrac{di_{Lf}}{dt} \end{bmatrix} = \begin{bmatrix} -(r_L + r_C) & -1 & 0 \\ 1 & 0 & 0 \\ 0 & 0 & -r_f \end{bmatrix} \begin{bmatrix} i_{L_1} \\ v_{C_1} \\ i_{Lf} \end{bmatrix} + \begin{bmatrix} (2v_{C_1} - V_{in}) & r_c i_o \\ -2i_{L_1} & -i_o \\ -V_{inv} & (V_{in} - 2v_{C_1}) \end{bmatrix} \begin{bmatrix} d_{ST} \\ m \end{bmatrix} + \begin{bmatrix} V_{in} - v_{C_1} \\ 0 \\ v_{inv} \end{bmatrix} \tag{4.16}$$

where the rightmost term is the disturbance which is bounded for all operating conditions, since V_{in} has a limited value and v_{C_1} and v_{inv} track their references which have also bounded amounts.

4.2.2 Multi Input Multi Output (MIMO) Sliding Mode Control Method

Two steps are required for applying SMC to a nonlinear system. First step is the definition of an appropriate sliding function and second step is the stability analysis by investigating existence conditions [87].

In recent studies the definition of the traditional sliding function is often sum of the state variable and its derivative or its integral to decrease the steady-state error [12], [29], [45]. Although the conventional sliding functions yield reasonable performance, derivative operation is needed in the implementation. Furthermore, the variable switching frequency of traditional SMC approaches is also another shortcoming making them undesirable for impedance source inverters. To alleviate these drawbacks, this chapter presents a simple MIMO sliding function removing derivative or integral of the state variable while achieving all the advantages of the traditional methods. The proposed method is applied on both standalone and grid-tied qZSI. The same sliding function is utilized for both standalone and grid-connected modes. The only difference is in the generation of the ac side inductor current reference [84]. While the ac side inductor current reference in grid-tied mode is generated via cascaded PR controllers, in the standalone mode this current is produced through only one PR controller. Section 4.3.2 discusses the reference generation in grid-tied mode in detail and the sliding function definition and stability analysis in grid-tied mode are the same as standalone mode which is explained in the following section.

I. Sliding Surface Design

The state variables are defined as follows

$$x_1 = V_{C_1}^* - v_{C_1},\ \ x_2 = I_{L_1}^* - i_{L_1},\ \ x_3 = i_{L_f}^* - i_{L_f} \tag{4.17}$$

where $I_{L_1}^*$, $V_{C_1}^*$ and i_{Lf}^* represent the references for i_{L_1}, v_{C_1} and i_{L_f}, respectively. The sliding surface function and the sliding surface derivative are defined as

$$S = \begin{bmatrix} S_{dc} \\ S_{ac} \end{bmatrix} = \begin{bmatrix} \alpha x_1 + x_2 \\ x_3 \end{bmatrix},\ \frac{dS}{dt} = \begin{bmatrix} \frac{dS_{dc}}{dt} \\ \frac{dS_{ac}}{dt} \end{bmatrix} = \begin{bmatrix} \alpha \frac{dx_1}{dt} + \frac{dx_2}{dt} \\ \frac{dx_3}{dt} \end{bmatrix} \tag{4.18}$$

where α is the positive sliding constant. Likewise, the derivatives of the state variables can be written as

$$\frac{dx_1}{dt} = -\frac{1}{C}(i_{L1} - 2d_{ST} i_{L1} - m i_o) \tag{4.19}$$

$$\frac{dx_2}{dt} = -\frac{1}{L}(d_{ST}(2v_{C1} - V_{in}) + (V_{in} - v_{C1}) - (r_L + r_C) i_{L1} + m r_C i_o) \tag{4.20}$$

$$\frac{dx_3}{dt} = \frac{di_{Lf}^*}{dt} - \frac{1}{L_f}(-r_f i_{Lf} + (1 - d_{ST}) v_{inv} - m(2v_{C1} - V_{in})) \tag{4.21}$$

Thus, the derivative of the sliding function is obtained as

$$\frac{dS}{dt} = F + GU = \begin{bmatrix} f_1 \\ f_2 \end{bmatrix} + \begin{bmatrix} g_1 & g_3 \\ g_4 & g_2 \end{bmatrix} \begin{bmatrix} d_{ST} \\ m \end{bmatrix} \tag{4.22}$$

where

$$f_1 = \frac{1}{L}(v_{C1} - V_{in}) + (-\frac{\alpha}{C} + \frac{r_L + r_C}{L}) i_{L1} \quad , \quad g_4 = \frac{v_{inv}}{Lf} \tag{4.23}$$

$$g_1 = -\frac{1}{L}(2v_{C1} - V_{in}) + \frac{\alpha}{C} 2 i_{L1} \quad , \quad g_2 = \frac{2v_{C1} - V_{in}}{Lf} \tag{4.24}$$

$$f_2 = \frac{di_{Lf}^*}{dt} - \frac{v_{inv}}{L_f} + \frac{r_f i_{Lf}}{L_f} \quad , \quad g_3 = (-\frac{r_C}{L} + \frac{\alpha}{C})i_o \tag{4.25}$$

When the system is in sliding mode, the dynamics of the system can be represented by $S = 0$ and $\frac{dS}{dt} = 0$. For deriving the dynamic behavior of dc side capacitor voltage and inductor current, (4.18) can be equated to zero. Therefore, substituting (4.20) to $\alpha \frac{dx_1}{dt} + \frac{dx_2}{dt} = 0$, the differential equation of x_1 can be obtained as

$$K_1 \frac{dx_1}{dt} + K_2 x_1 + K_3 = 0 \tag{4.26}$$

where $K_1 = \frac{C(r_C + r_L)}{(1-2d_{ST})} - \alpha L$, $K_2 = (1-2d_{ST})$ and $K_3 = -V_{in}(1-d_{ST}) + V_{C1}^*(1-2d_{ST})$.

By using Laplace transform, the solution of (4.26) can be obtained as follows

$$x_1(t) = -\frac{K_3}{K_2} + (V_{C1}^* + \frac{K_3}{K_2})e^{\frac{-t}{\tau_1}} \tag{4.27}$$

where τ_1 denotes time constant defined as

$$\tau_1 = \frac{C(r_C + r_L) - \alpha L(1-2d_{ST})}{(1-2d_{ST})^2} \tag{4.28}$$

Since for the stability of the control method, the closed loop poles should be located at the left half of the s-plane, thus τ_1 should be positive. From which the upper limit of α can be obtained as

$$\alpha < \frac{C(r_C + r_L)}{L(1-2d_{ST})} \tag{4.29}$$

Since $V_{C_1}^*$ is the reference of v_{C_1} and designed to be equal to the steady state value of v_{C_1}, K_3 becomes zero in the steady state. Therefore, obviously $x_1(t)$ decays to zero.

Similarly, for finding the differential equation of $x_2(t)$, (4.19) is substituted into $\alpha \frac{dx_1}{dt} + \frac{dx_2}{dt} = 0$ and the result is given as

$$C \frac{dx_2}{dt} + \alpha(1-2d_{ST})x_2 - \alpha(1-2d_{ST})I_{L1}^* + \alpha M I_o = 0 \tag{4.30}$$

In the derivation of (4.30), the term mi_o is replaced by its dc component. The solution of (4.30) can be obtained as

$$x_2(t) = I_{L1}^* - \frac{MI_o}{2(1-2d_{ST})} + \frac{MI_o}{2(1-2d_{ST})} e^{\frac{-t}{\tau_2}} \tag{4.31}$$

where τ_2 denotes time constant of $x_2(t)$ defined as

$$\tau_2 = \frac{C}{\alpha(1-2d_{ST})} \tag{4.32}$$

Checking the stability of the system reveals that τ_2 is always positive (except for $d_{ST} = 0.5$).

The power balance equation for all the system considering both sides can be written as

$$V_{in} I_{L1} = \frac{V_o I_o}{2} \tag{4.33}$$

Therefore, the steady state value of I_{L1} can be obtained by substituting the peak value of output voltage and current in equation (4.33). Thus, substituting (4.1) and (2.12) in (4.33) yields:

$$I_{L1} = \frac{MI_o}{2(1-2d_{ST})} \tag{4.34}$$

On the other hand, in the reference generation in section 4.2.3, substitution of (4.3) in (4.72) produces the inductor current reference as $I_{L1}^* = MI_o / 2(1-2d_{ST})$. Thus, due to the equality of I_{L_1} and I_{L1}^* in the steady state, $x_2(t)$ decays to zero as well. Besides, as it is shown in section 4.2.3, PR controller achieves zero steady state error, hence x_3 converges to zero as well.

The dynamic response of dc side variables (capacitor voltages and inductor currents) can be affected through variation in control gain (α) of the dc side sliding manifold. It means that adjusting this coefficient can be made by investigating to get better dynamic response and lower ripple in inductor current. Equations (4.27) and (4.31) show the behavior of the dc side variables. According to the time constant of $x_1(t)$ and $x_2(t)$, which is given in (4.28) and (4.32), growing α improves the dynamic response by decreasing both time constants of the dc side variables.

II. Stability Analysis

The most beneficial and universal method for studying the stability of nonlinear systems is the theory presented in the late 19^{th} century by the Russian mathematician Alexandr Mikhailovich Lyapunov [77]. The Lyapunov theory includes two methods for stability analysis which are linearization method and direct method. The linearization method investigates the stability of the system around the equilibrium point from the linear approximation of the system. The direct method is not limited to equilibrium point and investigates the stability of a nonlinear system by defining a scalar "energy-like" function. This theory expresses that if the total energy of a system is continuously dissipated, then the system, whether linear or nonlinear, must finally settle down to an equilibrium point. According to direct method, after the system enters to sliding phase, to keep the state trajectories on the sliding manifold and stay on equilibrium point, the following conditions should be satisfied [77]

$$S_{dc}\frac{dS_{dc}}{dt}<0 \quad , \quad S_{ac}\frac{dS_{ac}}{dt}<0 \tag{4.35}$$

The planned discontinuous control input is designed as

$$u=\begin{bmatrix} u_1 \\ u_2 \end{bmatrix}=\begin{bmatrix} 0.5(1+sign(S_{dc})) \\ sign(S_{ac}) \end{bmatrix} \tag{4.36}$$

where u_1 and u_2 are the discontinuous control inputs of dc and ac-side, respectively. Substituting (4.22) and (4.36) in (4.35) yields

$$S_{dc}\left(f_1+0.5(1+sign(S_{dc}))g_1+sign(S_{ac})g_3\right)<0 \tag{4.37}$$

$$S_{ac}\left(f_2+0.5(1+sign(S_{dc}))g_4+sign(S_{ac})g_2\right)<0 \tag{4.38}$$

Then, eight existence conditions are investigated for ac and dc side sliding manifolds to satisfy (4.35), which are given as follows:

$$\begin{aligned}
&\begin{bmatrix} S_{dc}>0 \\ S_{ac}>0 \end{bmatrix} \Rightarrow f_1+g_1+g_3<0 \\
&\begin{bmatrix} S_{dc}>0 \\ S_{ac}<0 \end{bmatrix} \Rightarrow f_1+g_1-g_3<0 \\
&\begin{bmatrix} S_{dc}<0 \\ S_{ac}>0 \end{bmatrix} \Rightarrow f_1+g_3>0 \\
&\begin{bmatrix} S_{dc}<0 \\ S_{ac}<0 \end{bmatrix} \Rightarrow f_1-g_3>0
\end{aligned} \tag{4.39}$$

$$\begin{aligned}
&\begin{bmatrix} S_{ac}>0 \\ S_{dc}>0 \end{bmatrix} \Rightarrow f_2+g_2+g_4<0 \\
&\begin{bmatrix} S_{ac}>0 \\ S_{dc}<0 \end{bmatrix} \Rightarrow f_2+g_2<0 \\
&\begin{bmatrix} S_{ac}<0 \\ S_{dc}>0 \end{bmatrix} \Rightarrow f_2+g_4-g_2>0 \\
&\begin{bmatrix} S_{ac}<0 \\ S_{dc}<0 \end{bmatrix} \Rightarrow f_2-g_2>0
\end{aligned} \tag{4.40}$$

Reorganizing (4.39) and (4.40) and considering steady state values of variables, the boundaries of constants which constitute the existence of sliding mode can be determined as

$$\left(\frac{-V_{C1}+(r_L+r_C)I_{L1}+r_C I_o}{I_o-I_{L1}}\right)\frac{C}{L}<\alpha<\left(\frac{V_{C1}-(r_L+r_C)I_{L1}+r_C I_o}{I_o+I_{L1}}\right)\frac{C}{L} \tag{4.41}$$

$$\frac{-V_{pn}-V_{inv}}{L_f}<\frac{di_{Lf}^*}{dt}<\frac{V_{pn}-V_{inv}}{L_f} \tag{4.42}$$

where I_o is the amplitude of i_o and V_{inv} is the steady state value of v_{inv}. The satisfaction of inequalities (4.41) and (4.42) can be assured for the whole operational points [81]. On the other hand, adding V_{inv} to all terms of (4.42) yields

$$\left|v_o^*\right|<V_{pn} \tag{4.43}$$

III. Fixed Switching Frequency

The chattering problem in traditional sliding mode control method generates unwanted fluctuations with limited frequency and limited amplitude caused by the fast dynamic in the control loop which was neglected in system modeling. Because the amplitude of chattering depends on the magnitude of the control input, the simplest way to reduce the chattering is to decrease the control input magnitude without destroying the satisfaction of the existence conditions. The boundary layer technique which is introduced in [77] is organized based on the theory of reducing the control input magnitude. Figure 4.3 shows the boundary layer method and the process of decreasing or reducing the sliding manifold in a thin boundary layer. The chattering ripples are smoothed in a boundary layer which is denoted by $B(t)$ as follows

$$B(t)=\left\{x,\left|S(x,t)\right|\le\phi\right\} \quad , \quad \phi>0 \tag{4.44}$$

where $B(t)$ is the boundary layer, ϕ is the boundary layer thickness and $\varepsilon=\phi/\alpha^{n-1}$

is the boundary layer width as shown in Figure 4.3 for $n = 2$ [77] where n shows the number of variables in sliding manifold.

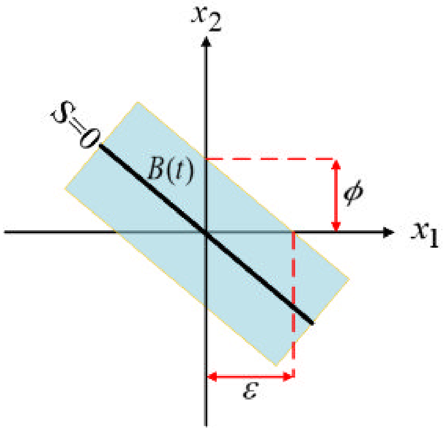

Figure 4.3: The boundary layer method.

Therefore, in this method the discontinuous control input in (4.36) is substituted with a saturated continuous control input that approximates (4.36) inside $B(t)$ during the sliding mode when $S = 0$. It means that inside the boundary layer the control input is continuous and determined as $\frac{S}{\phi}$ and outside the boundary layer, it is discontinuous. However, alongside the chattering mitigation, a definite tracking error (ε) is inevitable. The relation between the error and the boundary layer thickness can be defined as

$$\left|x_{(i)}\right| \leq \varepsilon = \phi / \alpha^{n-1} \Rightarrow i = 1, 2, 3 \tag{4.45}$$

where $x_{(i)}$ is the tracking error of the state variables. Therefore, selection of the boundary layer thickness is a tradeoff between tracking error and robustness. Figure 4.4 depicts the process of approximating the discontinuous control input to a continuous value inside a boundary layer for both dc and ac sides which are signified by ϕ_{dc} and ϕ_{ac} .

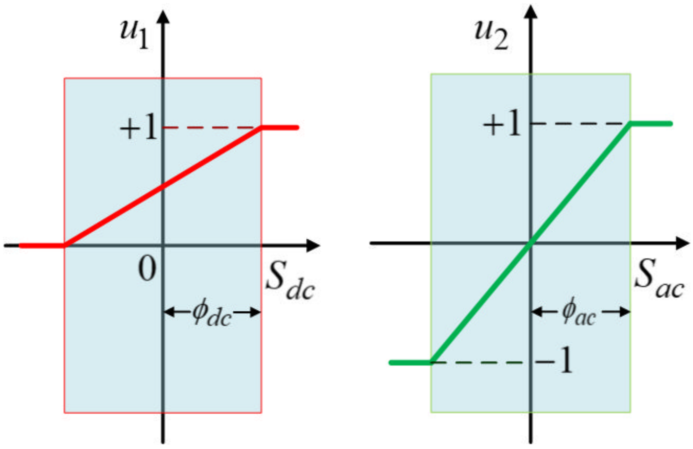

Figure 4.4: Control inputs within the boundary layers.

To ensure the existence of the sliding mode while using boundary layer method, the Lyapunov theory stability analysis can be defined for the smoothed control inputs. To satisfy the existence conditions, the subsequent equations should hold

$$S > \phi \quad \rightarrow \quad \frac{d(S-\phi)}{dt} < 0 \tag{4.46}$$

$$S < -\phi \quad \rightarrow \quad \frac{d(S-(-\phi))}{dt} > 0 \tag{4.47}$$

Since ϕ is selected to be a time invariant parameter, then (4.46) and (4.47) can be obtained as

$$S > \phi \rightarrow \frac{dS}{dt} < 0 \quad , \quad S < -\phi \quad \rightarrow \quad \frac{dS}{dt} > 0 \tag{4.48}$$

IV. Selection of Boundary Layer Thickness

The smoothed and continuous sliding manifolds inside the boundary layer are considered as the control inputs of the PWM process. The smoothed dc side sliding manifold can be written as

$$S_{dc} = \alpha x_1 + x_2 = \alpha(V_{C1}^{*} - (V_{C1} + \tilde{v}_{C1})) + I_{L1}^{*} - (I_{L1} + \tilde{i}_{L1}) \tag{4.49}$$

where $\tilde{v}_{C_1}$ and $\tilde{i}_{L_1}$ are the double frequency ripples of capacitor voltage and inductor current which can be written as [18]

$$\tilde{v}_{C1} = \tilde{V}_{C1}\sin(2\omega t - \theta) = \frac{\omega LMI_o}{(1-2d_{ST})^2 - 4LC\omega^2}\sin(2\omega t - \theta) \tag{4.50}$$

$$\tilde{i}_{L1} = \tilde{I}_{L1}\cos(2\omega t - \theta) = \frac{(1-2d_{ST})MI_o}{2(1-2d_{ST})^2 - 8LC\omega^2}\cos(2\omega t - \theta) \tag{4.51}$$

where θ represents a phase difference, $\tilde{V}_{C_1}$ and $\tilde{I}_{L_1}$ are the amplitudes of $\tilde{v}_{C_1}$ and $\tilde{i}_{L_1}$ respectively. Replacing (4.50) and (4.51) in (4.49) gives

$$S_{dc} = (\alpha\varepsilon) + k(\alpha 2\omega L\sin(2\omega t - \theta) + (1-2d_{ST})\cos(2\omega t - \theta)) \tag{4.52}$$

where ε is the steady state error of x_1 occurring due to the boundary layer and k is given by

$$k = \frac{MI_o}{2(4LC\omega^2 - (1-2d_{ST})^2)} \tag{4.53}$$

On the other hand, according to Figure 4.6, $\phi_{dc} = S_{dc} / (2d_{ST} - 1)$. Replacing (4.52) in this equation yields

$$\phi_{dc} = \frac{\alpha\varepsilon}{2d_{ST} - 1} + \frac{k[2\alpha\omega L\sin(2\omega t - \theta) + (1-2d_{ST})\cos(2\omega t - \theta)]}{2d_{ST} - 1} \tag{4.54}$$

Equation (4.54) shows that ϕ_{dc} has a dc and a time varying component. However, when computing ϕ_{dc} value which is used in experimental studies, only dc component is considered. Although the use of dc component causes an error in v_{C1}, v_{C2} and v_{pn}, the amount of this error can be minimized by selecting appropriate ϕ_{dc} value. The bounds of smoothed sliding manifolds in ac side (S_{ac} / ϕ_{ac}), which is defined based on the relation between the modulation signal and carrier signal, is given as [82]

$$Slope_{(S_{ac}/\phi_{ac})} < Slope_{(carrier)} \tag{4.55}$$

The ac side approximated sliding surface manifold can be obtained as

$$\frac{S_{ac}}{\phi_{ac}} = \frac{i_{Lf}^{*} - i_{Lf}}{\phi_{ac}} = \frac{i_{C}^{*} - i_{C} + i_{o}^{*} - i_{o}}{\phi_{ac}} \tag{4.56}$$

Equation (4.56) can be simplified due to the equality of load current (i_o) in steady state to the reference (i_o^*) and approximately equality of the capacitor current error ($i_C^* - i_C$) to the current ripple over L_f (Δi_{Lf}). Therefore, (4.56) can be modified as

$$\frac{S_{ac}}{\phi_{ac}} = \frac{\Delta i_{Lf}}{\phi_{ac}} = \frac{v_{Lf}}{L_f \phi_{ac}} \Delta t = \frac{v_{inv} - v_o}{L_f \phi_{ac}} m T_{sw} \tag{4.57}$$

Substituting, $v_{inv} = v_{pn}$, $v_o = m v_{pn}$ and $m = M \sin \omega t$ in (4.57) yields

$$\frac{S_{ac}}{\phi_{ac}} = \frac{v_{pn} - m v_{pn}}{L_f \phi_{ac}} m T_{sw} = \frac{M v_{pn} \left(1 - M \sin(\omega t)\right) \sin(\omega t) T_{sw}}{L_f \phi_{ac}} \tag{4.58}$$

The maximum ripple can be obtained by finding the value of modulation index where the derivative of (4.58) is zero which can be written as follows

$$\frac{d(\frac{S_{ac}}{\phi_{ac}})}{dt} = \cos(\omega t)\left(1 - M \sin(\omega t)\right) - M \sin(\omega t) \cos(\omega t) = 0 \tag{4.59}$$

For maximum ripple the following equation can be obtained:

$$\sin(\omega t) = \frac{1}{2M} \tag{4.60}$$

Then, replacing (4.60) in (4.58) yields

$$\frac{S_{ac}}{\phi_{ac}} = \frac{v_{pn} T_{sw}}{4 L_f \phi_{ac}} \tag{4.61}$$

The slope of S_{ac}/ϕ_{ac} can be found by differentiating (4.61) with respect to T_{sw} as follows

$$\text{Slope}_{(S_{ac}/\phi_{ac})} = \frac{v_{pn}}{4 L_f \phi_{ac}} \tag{4.62}$$

The slope of the carrier can be calculated geometrically as

$$\text{Slope}_{(carrier)} = 4V_p f_{sw} \tag{4.63}$$

where V_p and f_{sw} are the amplitude and frequency of the carrier signal, respectively. Therefore, by substituting (4.62) and (4.63) in (4.55), the lower boundary of ϕ_{ac} can be found as

$$\phi_{ac} > \frac{V_{pn}}{16V_p f_{sw} L_f} \tag{4.64}$$

Equation (4.64) shows the minimum value of ϕ_{ac}. V_{pn} in equation (4.64) is the average value of inverter input voltage.

4.2.3 Reference Generation

The power generated by the qZS network is given by

$$P_{pn} = v_{pn} i_{pn} = (V_{pn} + \tilde{v}_{pn})(I_{pn} + \tilde{i}_{pn}) = V_{pn} I_{pn} + V_{pn} \tilde{i}_{pn} + \tilde{v}_{pn} I_{pn} + \tilde{v}_{pn} \tilde{i}_{pn} \tag{4.65}$$

where $\tilde{v}_{pn}$ and $\tilde{i}_{pn}$ denote the DFR of v_{pn} and i_{pn}, respectively. The extra double frequency power which propagates through all currents and voltages of the qZSI is due to the power balance equation in all single-phase inverters. The power balance for all the system considering both sides is described as following

$$P_{in} = V_{in} i_{L1} = P_{pn}(1 - d_{ST}) = v_{pn} i_{pn}(1 - d_{ST}) \tag{4.66}$$

Disregarding double frequency ripples in (4.66), one can derive the average value of inductor current as follows

$$I_{L_1} = \frac{V_{pn} I_{pn}(1 - d_{ST})}{V_{in}} \tag{4.67}$$

Substituting (2.12) in (4.67) yields the inductor current reference as

$$I_{L_1}^{*} = I_{pn} \frac{(1 - d_{ST})}{(1 - 2d_{ST})} \tag{4.68}$$

Replacing (2.11) in (4.68) yields the inductor current reference as

$$I_{L_1}^* = I_{pn}(\frac{V_{C_1}^*}{V_{in}}) \tag{4.69}$$

The reference for the output current of the inverter ($i_{L_f}^*$) is produced by using a PR controller whose transfer function is specified as

$$H_{PR}(s) = k_p + \frac{2k_i\omega_c s}{s^2 + 2\omega_c s + \omega_r^2} \tag{4.70}$$

where the cutoff frequency and the resonant frequency are denoted as ω_c and ω_r. The output voltage error $(v_o^* - v_o)$ is applied to the PR controller and the controller generates the inductor current reference. If ω_r is considered equal to the frequency of v_o^*, then the PR controller introduces a finite gain at ω_r thus v_o tracks v_o^* with zero error in the steady state. According to Figure 4.6.c, the modulation signal can be written as

$$m = \frac{(i_{Lf}^* - i_{Lf})}{\phi_{ac}} \tag{4.71}$$

On the other hand, v_{inv} is the inverter output voltage, which is essentially a sinusoidal waveform plus harmonics, can be written as

$$v_{inv} = v_{inv1} + v_{invh} = mV_{pn} + v_{invh} \tag{4.72}$$

where v_{inv1} and v_{invh} are the fundamental and harmonic components, respectively. Nevertheless, the harmonic components are ignored for simplicity and v_{inv} is considered as $v_{inv} = mV_{pn}$. Averaging (4.6) and (4.9) in one switching period yields

$$L_f \frac{di_{Lf}}{dt} = -r_f i_{Lf} + (1 - d_{ST})v_{inv} - v_o \tag{4.73}$$

Substituting $v_{inv} = \dfrac{V_{pn}(i_{Lf}^{*} - i_{Lf})}{\phi_{ac}}$ in (4.73) yields

$$L_f \frac{di_{Lf}}{dt} + r_f i_{Lf} + v_o = \frac{i_{Lf}^{*} - i_{Lf}}{\phi_{ac}}(1 - d_{ST})V_{pn} \tag{4.74}$$

Substitution of (2.11) and (2.12) into (4.74) and considering $V_{C1}^{*} = V_{C1}$ in steady state, one can obtain

$$L_f \frac{di_{Lf}}{dt} + r_f i_{Lf} + v_o = \frac{i_{Lf}^{*} - i_{Lf}}{\phi_{ac}} V_{C1}^{*} \tag{4.75}$$

According to Figure 4.1, i_{Lf} can be written as $i_{Lf} = i_{C_f} + i_o$ whose Laplace transform under resistive load yields

$$I_{Lf}(s) = (sC_f + \frac{1}{R})V_o(s) \tag{4.76}$$

Substituting (4.76) in the Laplace transform of (4.75) results in

$$\left(KL_f C_f s^2 + (\frac{KL_f}{R} + Kr_f C_f + C_f)s + \frac{Kr_f}{R} + K + \frac{1}{R} \right) V_o(s) = I_{Lf}^{*}(s) \tag{4.77}$$

where $K = \phi_{ac} / V_{C1}^{*}$. Since I_{Lf}^{*} is generated through PR controller by processing $(v_o^{*} - v_o)$, the Laplace transform of PR output can be written as

$$I_{Lf}^{*}(s) = (V_o^{*}(s) - V_o(s)) \left(\frac{k_p s^2 + 2\omega_c (k_p + k_i)s + k_p \omega_r^2}{s^2 + 2\omega_c s + \omega_r^2} \right) \tag{4.78}$$

Now, substituting (4.78) into (4.77) gives

$$\frac{V_o(s)}{V_o^{*}(s)} = \frac{k_p s^2 + 2\omega_c (k_p + k_i)s + k_p \omega_r^2}{b_4 s^4 + b_3 s^3 + b_2 s^2 + b_1 s + b_0} \tag{4.79}$$

Where

$$b_0 = (\frac{Kr_f}{R} + K + \frac{1}{R})\omega_r^2 + k_p\omega_r^2$$

$$b_1 = (\frac{KL_f}{R} + Kr_fC_f + C_f)\omega_r^2 + 2\omega_c(\frac{Kr_f}{R} + K + \frac{1}{R}) + 2\omega_c(k_p + k_i)$$

$$b_2 = KL_fC_f\omega_r^2 + 2\omega_c(\frac{KL_f}{R} + Kr_fC_f + C_f) + \frac{Kr_f}{R} + K + \frac{1}{R} + k_p$$

$$b_2 = KL_fC_f\omega_r^2 + 2\omega_c(\frac{KL_f}{R} + Kr_fC_f + C_f) + \frac{Kr_f}{R} + K + \frac{1}{R} + k_p$$

$$b_3 = 2\omega_c KL_fC_f + \frac{KL_f}{R} + Kr_fC_f + C_f$$

$$b_4 = KL_fC_f$$

The magnitude response of $\frac{V_o(s)}{V_o^*(s)}$ which is calculated by using the system and control parameters in Table 4.1 is displayed in Figure 4.5. Clearly, the magnitude of $V_o(s)/V_o^*(s)$ is 0dB at 50Hz which means that the steady-state error in the output voltage is zero.

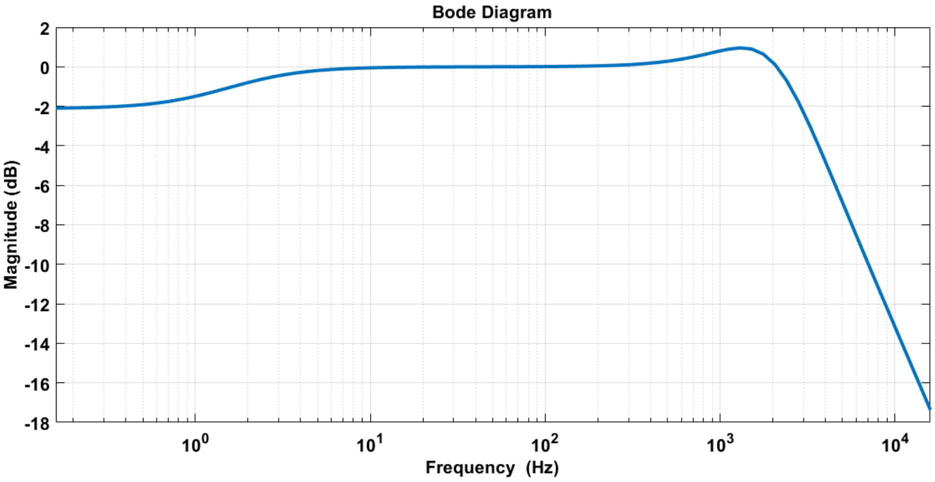

Figure 4.5: Magnitude response of equation (4.79)

4.2.4 Simulation and Experimental Results

Figure 4.6 shows of the proposed control method in three parts. The perspective of the entire control method, the reference generation and the sliding mode control are shown in Figure 4.6(a), Figure 4.6(b) and Figure 4.6(c), respectively. The performance and validity of the proposed control technique is explored through simulation and experimental studies. The proposed control method is implemented on OPAL-RT Wanda platform as shown in Figure 4.7. The single-phase inverter circuit board is made by Genesic GB100XCP12 IGBT modules and Avago ACPL-332J gate drivers. Voltage and current sensors are LEM LA100-P and LV 25-P, respectively. The system and control parameters in the simulation ex and experimental tests are also given in Table 4.1.

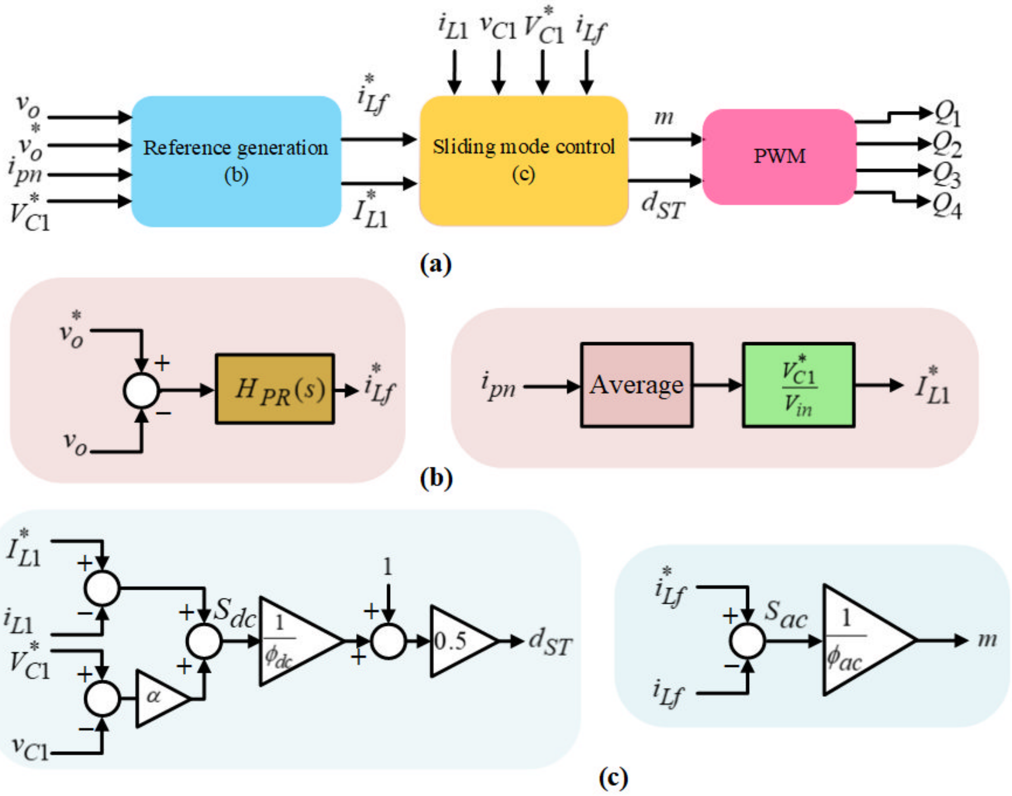

Figure 4.6: Block diagram of the proposed control method: (a) Control system, (b) Reference generation, (c) Sliding mode control

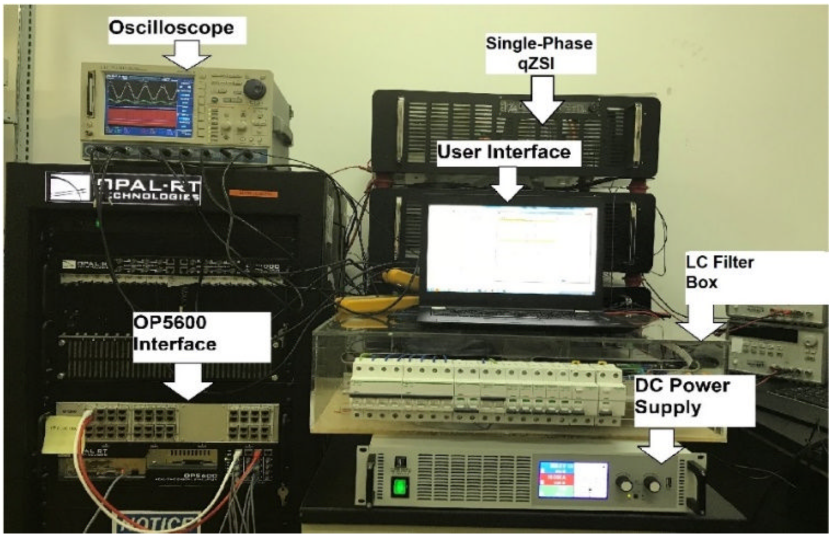

Figure 4.7: Prototype of single-phase qZSI.

Table 4.1: System and control parameters

Parameter	**Value**
Input dc voltage (V_{in})	250 V
qZS network inductances ($L_1 = L_2 = L$)	1000 μH
qZS network capacitances ($C_1 = C_2 = C$)	1000 μF
Filter inductance (L_f)	2000 μH
Filter capacitance (C_f)	10 μF
Amplitude of output voltage reference (v_o^*)	220 $\sqrt{2}$ V
Dc side capacitor voltage reference ($V_{C_1}^*$)	350 V
Nominal frequency (f_g)	50 Hz
Sampling time (T_s)	40 μ s
Switching frequency (f_{sw})	20 kHz
Amplitude of the carrier (V_P)	1 V
Proportional and resonant gains (k_p, k_i)	0.14,400
Cut off frequency (ω_c)	1
Sliding constant (α)	0.4
Boundary layer thickness (ϕ_{ac}, ϕ_{dc})	5,2

I. Steady State Response Results

Figure 4.8 and 4.9 depict the steady-state simulation and experimental results of dc side variables ($v_{pn}, v_{C_1}, v_{C_2}, i_{L_1}$) and ac side variables (v_o, i_o) under linear and nonlinear loads. The dc side capacitor voltage reference ($V_{C_1}^*$) and ac side load voltage references are considered to be 350V and $v_o^* = 220\sqrt{2}\sin(\omega t)$, respectively. The linear load is assumed to be a resistive load with 16Ω. The simulation and experimental responses of the variables under linear load are depicted in Figure 4.8(a) and 4.9(a), respectively. Considering Figure 4.8, the average value of v_{pn} is about 450V which infers that the boost factor (*B*) and shoot through duty cycle (d_{ST}) values are around 1.8 and 0.222, respectively. According to equation (2.11), with this d_{ST} value, the theoretical value of V_{C_1} is calculated to be 350V which is in good agreement with the presented simulation and experimental result. Similarly, the theoretical v_{C_2} is 100V which is also in good agreement with the simulation and experimental results. The nonlinear load connected to the inverter is a diode-bridge rectifier with parallel *RC* (*R*=65Ω and *C*=1000μF). The simulation and experimental responses of variables under this load are given in Figure 4.8(b) and 4.9(b). Comparing the actual values with their references, the controller outperforms as well. Specifically, even the load current is so much distorted, the load voltage is almost not affected from the nonlinear load current. The controlled variables such as v_{C_1} and v_o track their references in both linear and nonlinear load types.

The THDs and harmonic components (in rms) of load voltage under linear and nonlinear load types are given in Figure 4.10. It is clear that the load voltage of linear load type has much smaller harmonic components than that of nonlinear load. The THDs of load voltages of linear and nonlinear loads are measured to be 1.1% and 2.4%, respectively which are in the boundary of the internationally recognized standards [76].

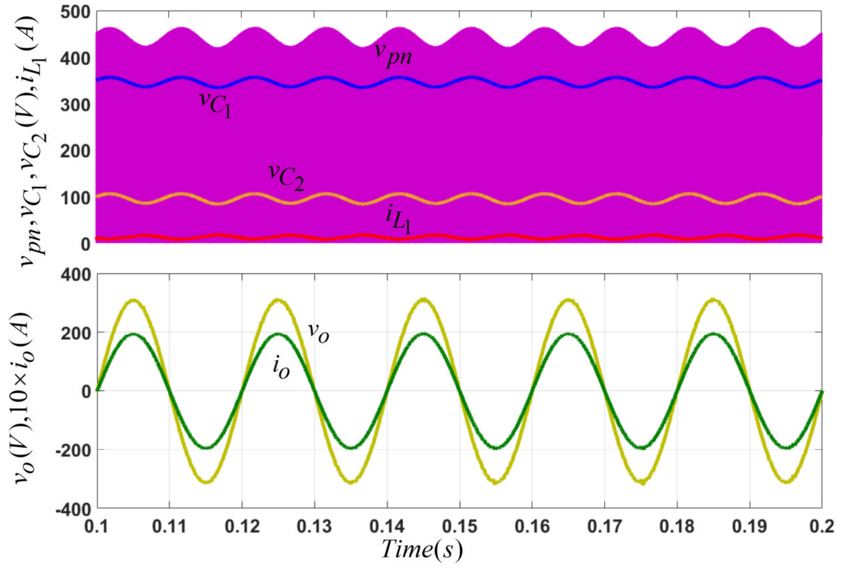

(a)

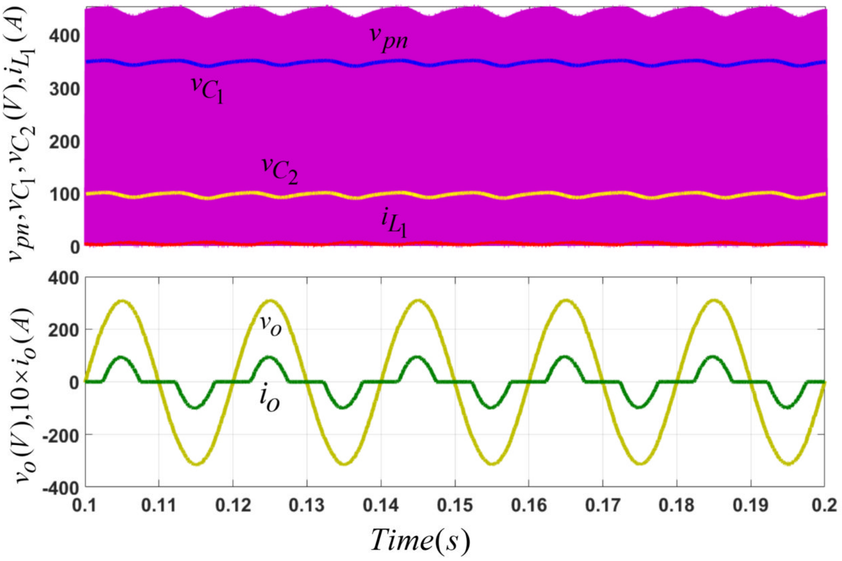

(b)

Figure 4.8: Simulation results of dc and ac side variables in steady state under: (a) Linear Load (b) Nonlinear load

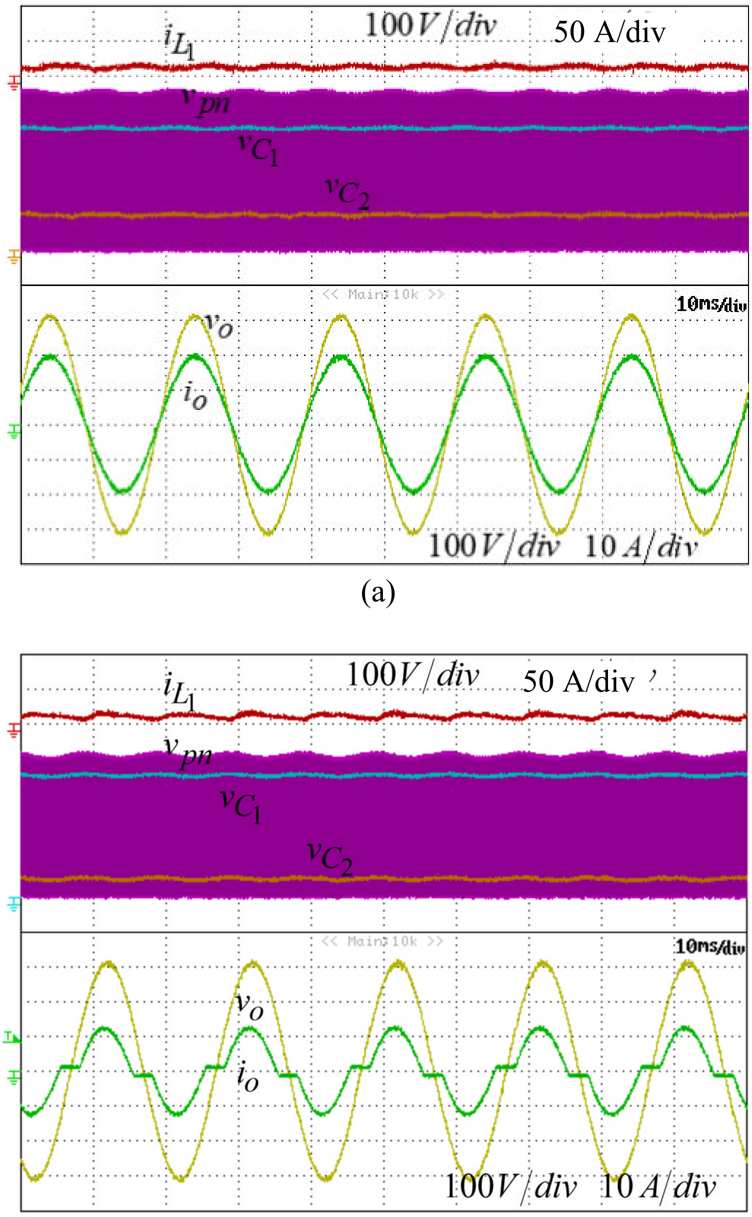

(a)

(b)

Figure 4.9: Experimental responses of dc and ac side variables in steady state under: (a) Linear Load (b) Nonlinear load

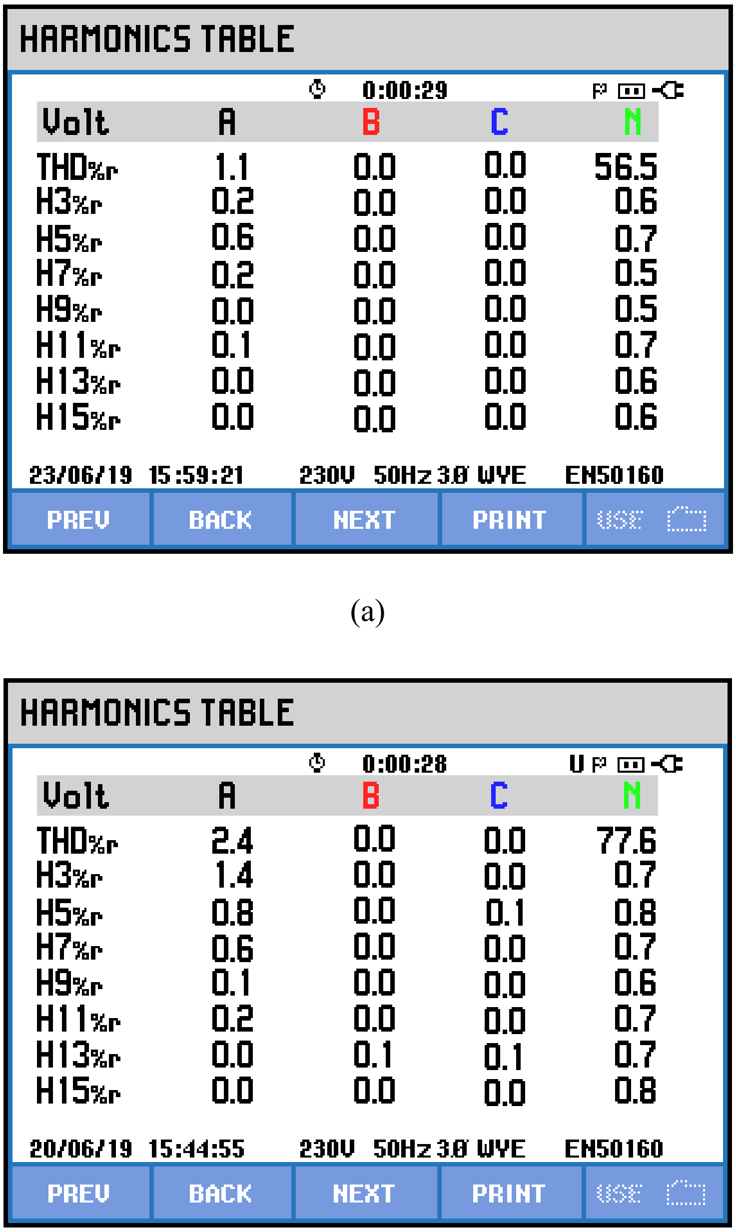

Volt	A	B	C	N
THD%r	1.1	0.0	0.0	56.5
H3%r	0.2	0.0	0.0	0.6
H5%r	0.6	0.0	0.0	0.7
H7%r	0.2	0.0	0.0	0.5
H9%r	0.0	0.0	0.0	0.5
H11%r	0.1	0.0	0.0	0.7
H13%r	0.0	0.0	0.0	0.6
H15%r	0.0	0.0	0.0	0.6

23/06/19 15:59:21 230V 50Hz 3Ø WYE EN50160

(a)

Volt	A	B	C	N
THD%r	2.4	0.0	0.0	77.6
H3%r	1.4	0.0	0.0	0.7
H5%r	0.8	0.0	0.1	0.8
H7%r	0.6	0.0	0.0	0.7
H9%r	0.1	0.0	0.0	0.6
H11%r	0.2	0.0	0.0	0.7
H13%r	0.0	0.1	0.1	0.7
H15%r	0.0	0.0	0.0	0.8

20/06/19 15:44:55 230V 50Hz 3Ø WYE EN50160

(b)

Figure 4.10: THD and harmonic components of load voltage under: (a) Linear load, (b) Nonlinear load

II. Dynamic Response Results

The dynamic responses of dc and ac side variables are inspected for linear and non-linear loads in two parts. In the first part, the dynamic response of the system is observed for a load change and in the second part, the dynamic response of the system is observed for a change in dc side capacitor voltage reference.

Figure 4.11(a) and 4.12(a) displays the simulation and experimental responses of the system variables for a sudden change in a linear load from 16 Ω to 32 Ω. The references for (v_{C_1}) and (v_o) are same as before. Considering the effect of load current on the inductor current, increasing load current leads to increment in the inductor current. Since increasing load current doesn't have effect on the duty cycle, both capacitor voltages in the dc side are maintained constant except for the transient period due to the load change. Because of this, the dc-link voltage (v_{pn}) also remains constant. Also, it is evident that the amplitude of the load voltage is almost not affected due the load change. The simulation and experimental dynamic responses obtained for an abrupt change in the nonlinear load are shown in Figure 4.11(b) and 4.12(b), respectively. Both dc and ac side variables exhibit good dynamic response to this load change. Again, except for the short transient period, the capacitor and dc-link voltages in the dc side converge to their original values which were attained before. On the other hand, it seems that the load voltage is not affected from the sudden variation in the nonlinear load.

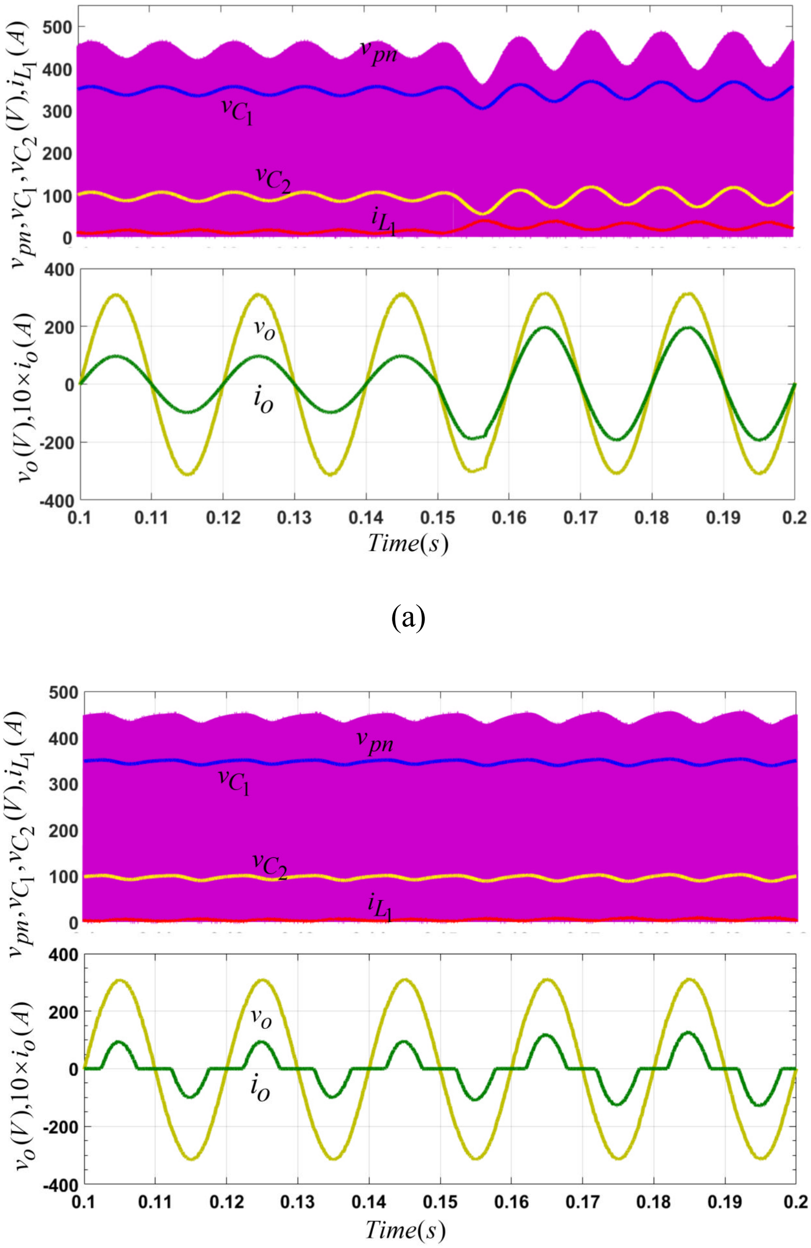

(a)

(b)

Figure 4.11: Simulated dynamic responses of dc and ac side variables for an abrupt change in: (a) Linear load, (b) Nonlinear load.

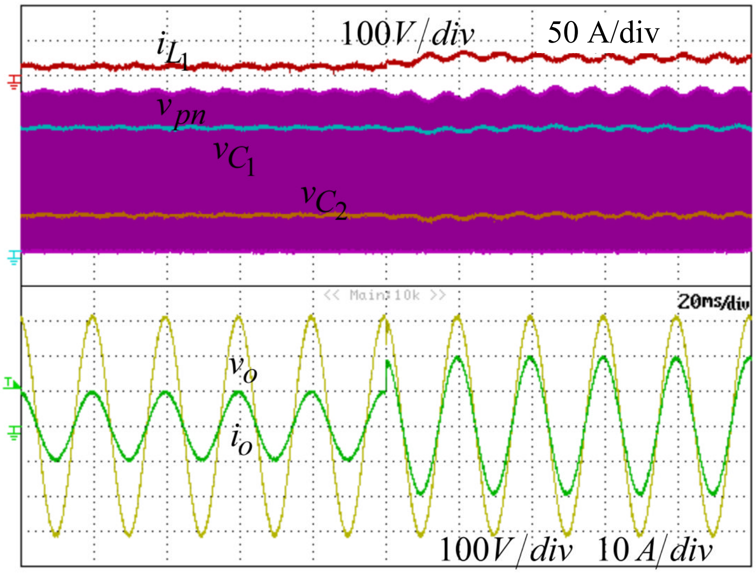

(a)

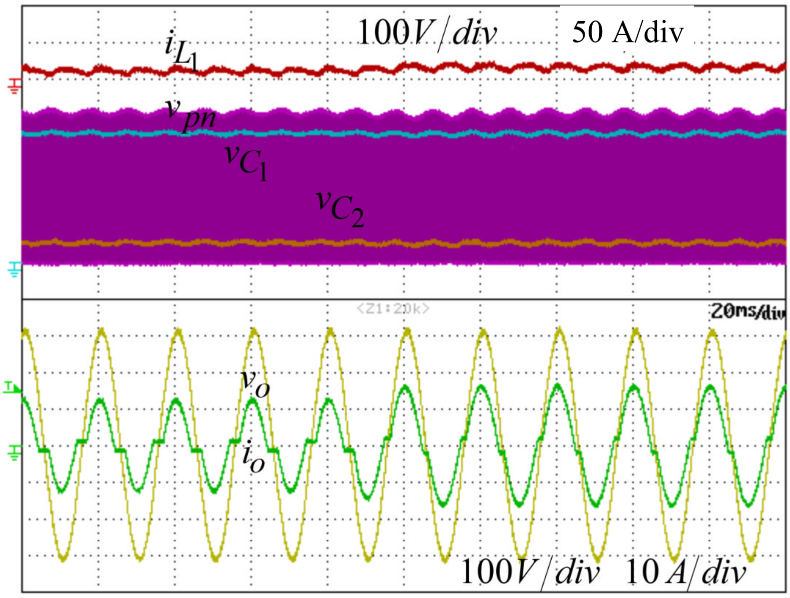

(b)

Figure 4.12: Experimental dynamic responses of dc and ac side variables for an abrupt change in: (a) Linear load, (b) Nonlinear load.

Dynamic response of the system for a sudden change in $V_{C_1}^{*}$ is also investigated. The simulation and experimental results are depicted in Figure 4.13 and 4.14 for linear and nonlinear load types, respectively. In Figure 4.13(a) and 4.14 (a), the simulation and experimental dynamic responses of dc and ac side variables are shown for an abrupt change in $V_{C_1}^*$ from 350V to 400V under linear load type. The operating point of the system before the step change corresponds to the operating point shown in Figure 4.8(a) and 4.9(a). It is important noting that when $V_{C_1}^*$ is changed to 400V, the boost factor is also increased from 1.8 to 2.2. Because of this increase in the boost factor, the dc-link voltage (v_{pn}) surges to 550V. In such a case, according to equation (2.11), v_{C_2} also surges to 150V. However, despite the change in $V_{C_1}^*$, the load voltage is maintained at its desired level without having any interruption. Except for the short transition period, the inductor current in dc side also preserves its value before and after the step change. Figure 4.13(b) and 4.14 (b) also depict the simulation and experimental dynamic responses of dc and ac side variables for a step change in $V_{C_1}^*$ for a nonlinear load. Again, the system responds to this reference change successfully and continues to operate without any problem.

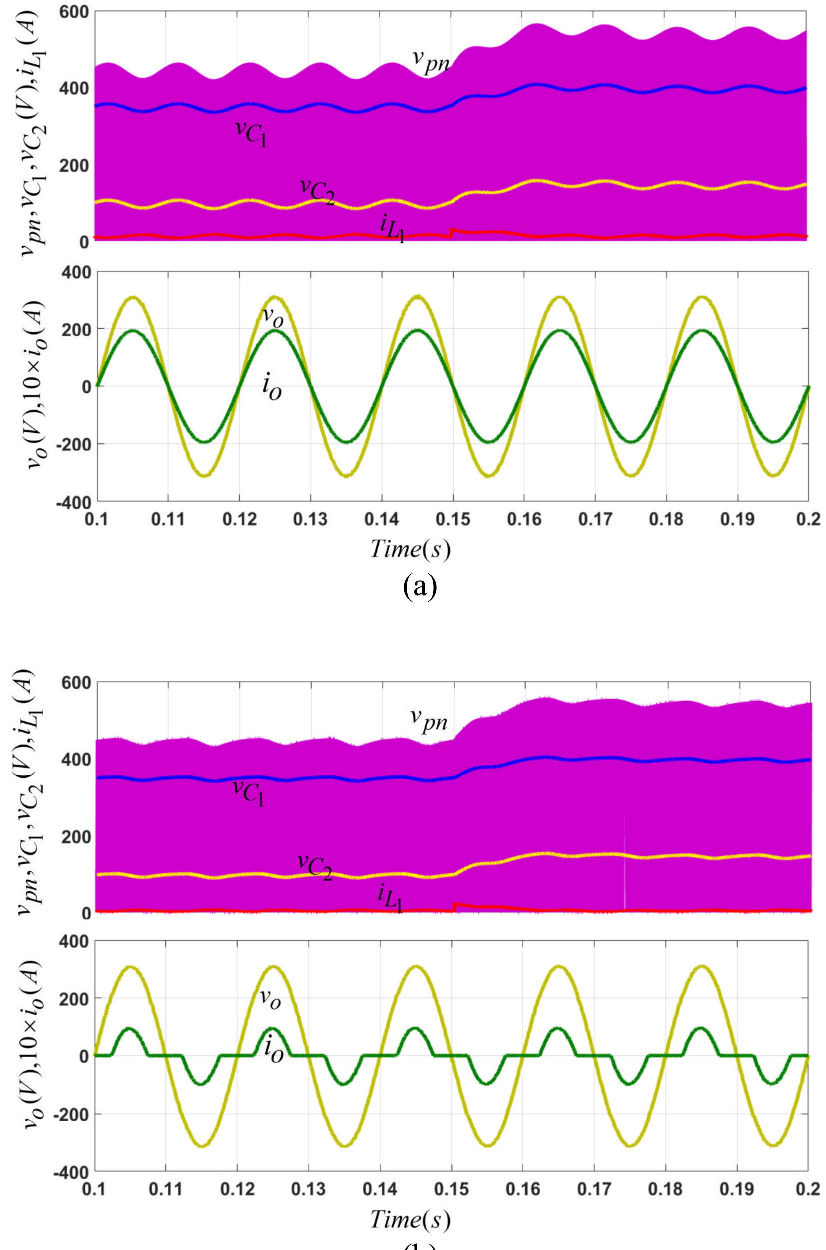

Figure 4.13: Simulated dynamic responses of dc and ac side variables for an abrupt change in $(v_{C_1}^*)$ under: (a) Linear load, (b) Nonlinear load.

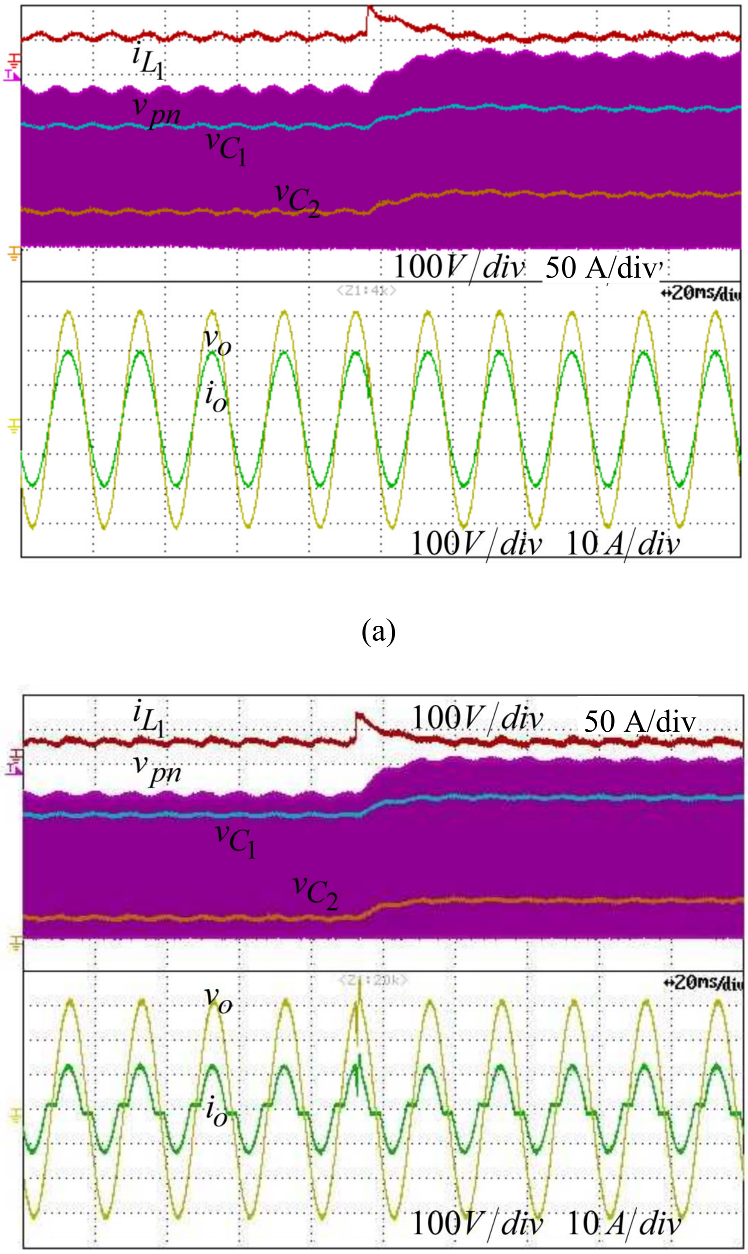

(a)

(b)

Figure 4.14: Experimental dynamic responses of dc and ac side variables for an abrupt change in $(v_{C_1}^{*})$ under: (a) Linear load, (b) Nonlinear load.

The dynamic response of the system for an abrupt change in the load type is also investigated. The simulation and experimental results are shown in Figure 4.15.and 4.16, respectively. Firstly, the inverter is connected to a resistive load (active load) with 65Ω and after that suddenly a reactive load with series RL (R=15Ω, L=90mH) is connected in parallel to the inverter. Obviously, with active load the phase difference is zero and after connection of the inductive load, the load current lags the load voltage by 30.6° which yields approximately a power factor of 0.86. The robustness of the control method is evident that the load voltage is not affected from the abrupt load type variation.

The simulation and experimental dynamic responses of the system variables for an abrupt change in V_{in} from 250V to 275V are displayed in Figure 4.16. According to equations (2.10) and (2.12), increasing V_{in} leads to increment in capacitor voltages and v_{pn}. Though, after passing the transients, the dc side variables converge to the new values in accordance with equations (2.10) and (2.12). However, because v_{C1} is controlled to track its own reference which is 350V, thus it is maintained at 350 V. The new values of v_{C2} and v_{pn} are 75V and 425V, respectively. The new shoot through and boost factor values according to the new operating point are computed to be 0.1765 and 1.5456, respectively. Regardless of the variations in the dc side, the ac side variables are unaffected from this step change due to the control method enforcing them to track their references.

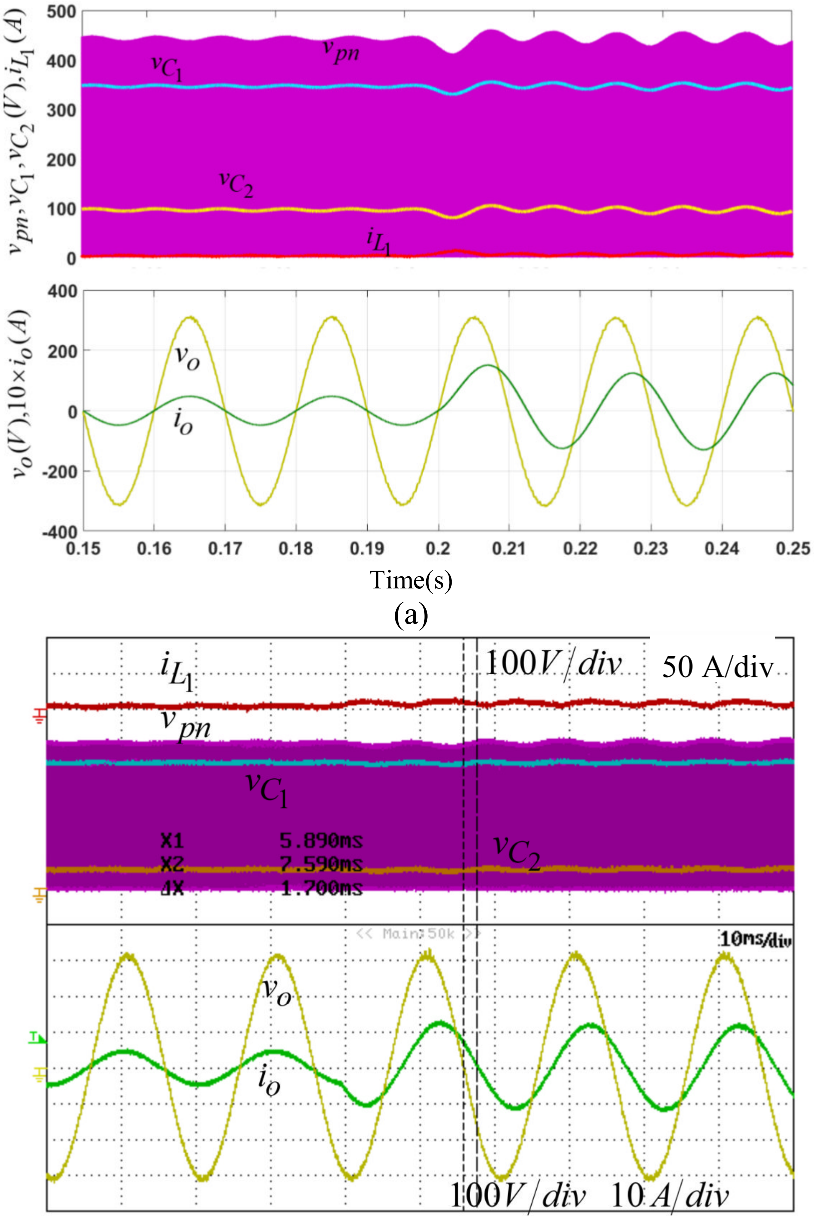

(a)

(b)

Figure 4.15: Simulated and experimental dynamic responses of dc and ac side variables for an abrupt change in the load type (a) Simulation result (b) Experimental result

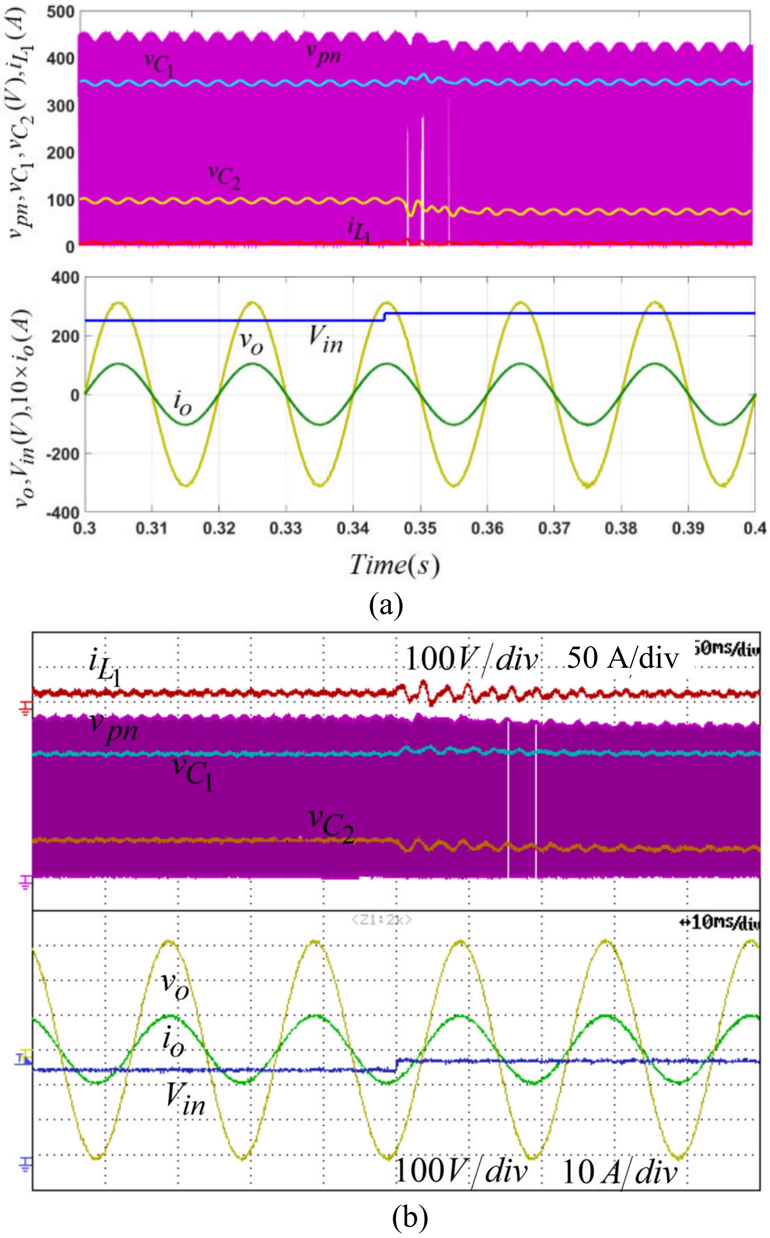

Figure 4.16: Dynamic responses of dc and ac side variables for an abrupt change in the dc input voltage. (a) Simulation result (b) Experimental result

The presented control approach is compared with the existing SMC based control methods introduced in [12], [42]-[44] in Table 4.2. Obviously, the presented control technique has many benefits in terms of implementation simplicity, robustness of both sides, and steady-state error.

Table 4.2: Comparison of the Proposed Method with Existing SMC Methods

Comparison category	**[12]**	**[42]**	**[43]**	**[44]**	**Proposed**
Topology	3-ph qZSI	1-ph qZSI	3-ph qZSI	1-ph ZSI	1-ph qZSI
Operation mode	Standalone	Grid-tied	Standalone	Grid-tied	Standalone
Number of sensors in dc/ac sides	5/3	5/2	3/3	3/2	3/2
Number of control gains	5	3	6	3	3
Robustness	Dc side only	Dc side only	Dc side only	Both sides	Both sides
Complexity	High	High	Normal	High	Simple
Steady-state error at output	Exists due to PI	Exists due to PI	Zero due to PR	Exists due to PI	Zero due to PR
THD of output volt./curr. (%)	Not reported	2.28	1.32	1.1	1.02
Concurrent use of SMC	Only in dc side	Only in dc side	Only in dc side	Both sides	Both sides

4.3 Grid-Tied Mode

4.3.1 State Space Modeling of Grid-Tied qZSI

Figure 4.17 depicts a single-phase qZSI connected to the grid through an *LCL* filter.

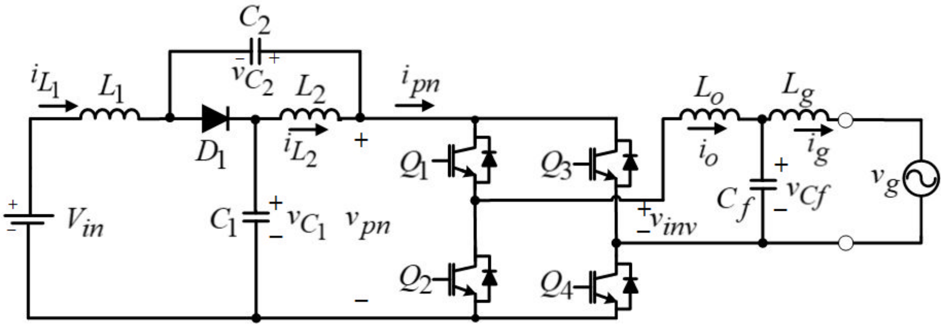

Figure 4.17: Single-phase LCL filtered qZSI connected to the grid.

The relation between v_{pn} and v_g can be written as

$$v_g = mv_{pn} \tag{4.80}$$

Where the modulation signal is defined as $m = M\sin\omega t$. The power balance equation for the single-phase inverter is written as [18]

$$v_{pn}i_{pn}(1-d_{ST}) = v_g i_g = mv_{pn}i_g \tag{4.81}$$

From (4.81), it follows that

$$i_{pn}(1-d_{ST}) = mi_g \tag{4.82}$$

Same as before, to simplify the equations, it can be assumed that $L_1 = L_2 = L$ and $C_1 = C_2 = C$. The equivalent model of the entire system in ST state and nST state is depicted in Figure 4.18.

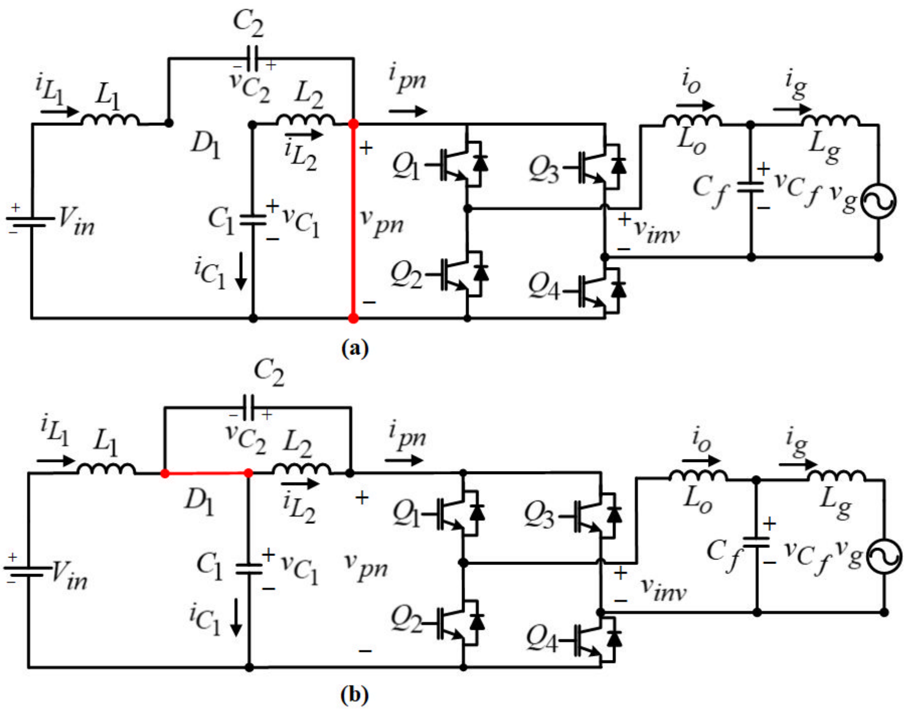

Figure 4.18: Equivalent model of the entire system in (a) ST state (b) nST state

According to Figure 4.18(a), the equations that can be derived in ST state are

$$L\frac{di_{L_1}}{dt} = V_{in} + v_{C_2} \tag{4.83}$$

$$C\frac{dv_{C_1}}{dt} = -i_{L_2} \tag{4.84}$$

$$L_o\frac{di_o}{dt} = -v_{C_f} \tag{4.85}$$

$$C_f\frac{dv_{C_f}}{dt} = i_o - i_g \tag{4.86}$$

According to Figure 4.18(b), the differential equations of the inverter in nST state are

$$L\frac{di_{L_1}}{dt} = V_{in} - v_{C_1} \tag{4.87}$$

$$C\frac{dv_{C_1}}{dt} = i_{L_1} - i_{pn} \tag{4.88}$$

$$L_o\frac{di_{L_o}}{dt} = v_{inv} - v_{C_f} \tag{4.89}$$

$$C_f\frac{dv_{C_f}}{dt} = i_o - i_g \tag{4.90}$$

The goal of the control method is to inject a sinusoidal grid current with unity power factor. Therefore, assuming the grid voltage as $v_g = V_g \sin(\omega t)$, then the grid current reference should be considered as

$$i_g^* = I_g^* \sin(\omega t) \tag{4.91}$$

where the reference value of the grid current is defined as i_g^*. Deriving the average equations of (4.83)-(4.90) yields

$$L\frac{di_{L_1}}{dt} = d_{ST}(V_{in} + v_{C2}) + (1 - d_{ST})(V_{in} - v_{C1}) \tag{4.92}$$

$$C\frac{dv_{C_1}}{dt} = d_{ST}(-i_{L_1}) + (1 - d_{ST})(i_{L_1} - i_{pn}) \tag{4.93}$$

$$L_o\frac{di_o}{dt} = d_{ST}(-v_{C_f}) + (1 - d_{ST})(v_{inv} - v_{C_f}) \tag{4.94}$$

$$C_f \frac{dv_{C_f}}{dt} = d_{ST}(i_o - i_g) + (1 - d_{ST})(i_o - i_g) \tag{4.95}$$

Rearranging (4.92)-(4.95), the following relationships are obtained

$$L\frac{di_{L_1}}{dt} = V_{in} - v_{C_1} + d_{ST}(2v_{C_1} - V_{in}) \tag{4.96}$$

$$C\frac{dv_{C_1}}{dt} = d_{ST}(-2i_{L_1}) + m(-i_g) + i_{L_1} \tag{4.97}$$

$$L_o \frac{di_o}{dt} = d_{ST}(-v_{inv}) + (v_{inv} - v_{C_f}) \tag{4.98}$$

$$C_f \frac{dv_{C_f}}{dt} = (i_o - i_g) \tag{4.99}$$

Therefore, if d_{ST} and m are considered as the control input variables of the system, then the matrix format of the state-space equations can be written as

$$\begin{bmatrix} L\frac{di_{L_1}}{dt} \\ C\frac{dv_{C_1}}{dt} \\ L_o\frac{di_o}{dt} \\ C_f\frac{dv_{C_f}}{dt} \end{bmatrix} = \begin{bmatrix} 0 & -1 & 0 & 0 \\ 1 & 0 & 0 & 0 \\ 0 & 0 & 0 & -1 \\ 0 & 0 & 1 & 0 \end{bmatrix} \begin{bmatrix} i_{L_1} \\ v_{C_1} \\ i_o \\ v_{C_f} \end{bmatrix} + \begin{bmatrix} 2v_{C1} - V_{in} & 0 \\ -2i_{L1} & -i_g \\ -v_{inv} & 0 \\ 0 & 0 \end{bmatrix} \begin{bmatrix} d_{ST} \\ m \end{bmatrix} + \begin{bmatrix} V_{in} \\ 0 \\ v_{inv} \\ -i_g \end{bmatrix} \tag{4.100}$$

4.3.2 Reference Generation

The grid power is considered as

$$P_g = v_g i_g = V_g \sin(\omega t) I_g \sin(\omega t) = 0.5 V_g I_g (1 - \cos(2\omega t)) \tag{4.101}$$

According to (4.101), the output power has an extra double frequency part which propagates through all currents and voltages of the qZSI. Equating the grid power and the source power yields

$$P_g = P_{in} = V_{in} i_{L_1} = 0.5 V_g I_g (1 - \cos(2\omega t)) \tag{4.102}$$

Because the inductor current of the qZS network has also a double frequency ripple, ignoring this part in both input and output power in (4.102) yields

$$V_{in}I_{L_1} = \frac{V_g I_g}{2} \tag{4.103}$$

So, the inductor current reference of the qZS network can be obtained as

$$I_{L_1}^* = \frac{V_g I_g^*}{2V_{in}} \tag{4.104}$$

Two cascaded PR controllers produce the ac side inductor current reference (i_o^*). The s-domain equations of the PR controllers are defined as

$$H_{PR1}(s) = K_{p1} + \frac{2K_{r1}\omega_c s}{s^2 + 2\omega_c s + \omega^2} \tag{4.105}$$

$$H_{PR2}(s) = K_{p2} + \frac{2K_{r2}\omega_c s}{s^2 + 2\omega_c s + \omega^2} \tag{4.106}$$

where the cutoff frequency and the resonant frequency are given as ω_c and ω, respectively. The first PR controller generates v_C^* by applying the grid current error ($i_g^* - i_g$) as the input and the second PR controller generates the desired i_o^* by applying the capacitor voltage error ($v_C^* - v_C$) as the input. The dynamic and steady-state responses of the system are determined by tuning K_{p1}, K_{p2}, K_{r1} and K_{r2}.

4.3.3 Simulation Responses

Matlab/Simulink software is used to verify the correctness and effectiveness of the proposed control technique in grid-tied mode. Figure 4.19 displays the system with the related MIMO SMC method. Table 4.3 shows the system and control parameters used to simulate the system.

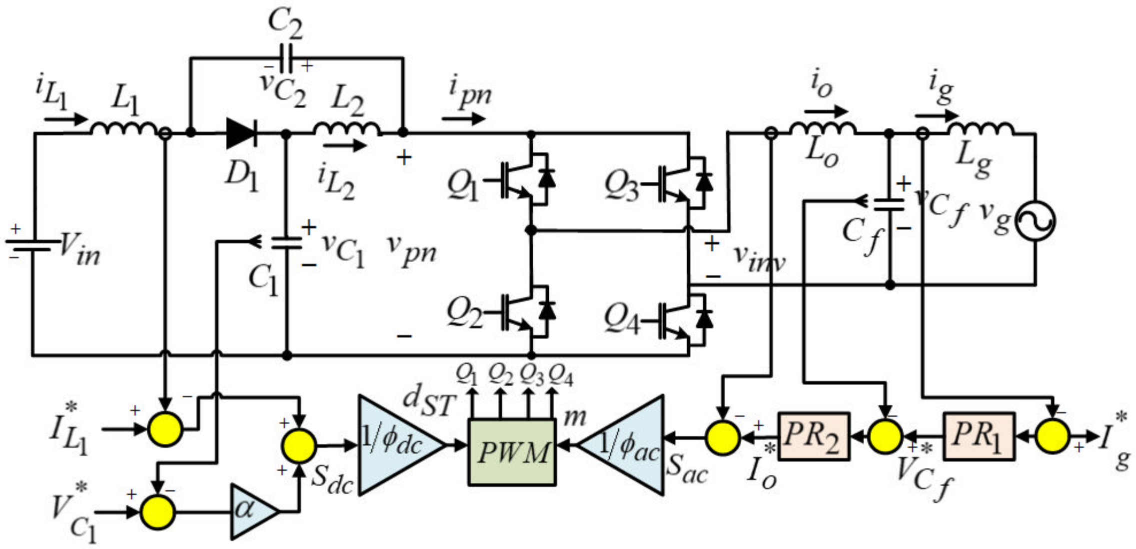

Figure 4.19: Single-phase grid-tied qZSI with the proposed control method.

The steady-state behavior of the voltages of the qZS network variables (v_{C_1} , v_{C_2} , v_{pn}) are depicted in Figure 4.20. The capacitor voltage reference is 400 V and obviously, v_{C_1} tracks its reference successfully. Calculating v_{pn} from equation (2.12) gives the value of v_{pn} as 544V which agrees well with the result of the simulation. The values of the shoot-through duty cycle and the boost factor are computed to be 0.27 and 2.17, respectively. Similarly, the value of v_{C_2} can be computed from (2.11) which is 146 V and it is almost equal to the result shown in Figure 4.20.

Table 4.3: System and control parameters

Parameter	**Value**
Input dc voltage (V_{in})	250 V
qZS network inductances ($L_1 = L_2 = L$)	3mH
qZS network capacitances ($C_1 = C_2 = C$)	1000 μF
Filter inductance (L_o)	2mH
Filter inductance (L_g)	0.6867mH
Filter capacitance (C_f)	9 μF
Grid voltage (V_g)	$230\sqrt{2}$ V
Amplitude of grid current reference (I_g^*)	10 A
Dc side capacitor voltage reference (V_{C1}^*)	400V
Nominal frequency (f_g)	50Hz
Switching frequency (f_{sw})	10kHz
Proportional and resonant gains (K_{p1}, K_{p2}, K_{r1}, K_{r2})	1, 0.6,3000,3000
Cut off frequency (ω_c)	1 rad/s
Sliding constant (α)	0.2
Boundary layer thickness (ϕ_{ac}, ϕ_{dc})	1, 1

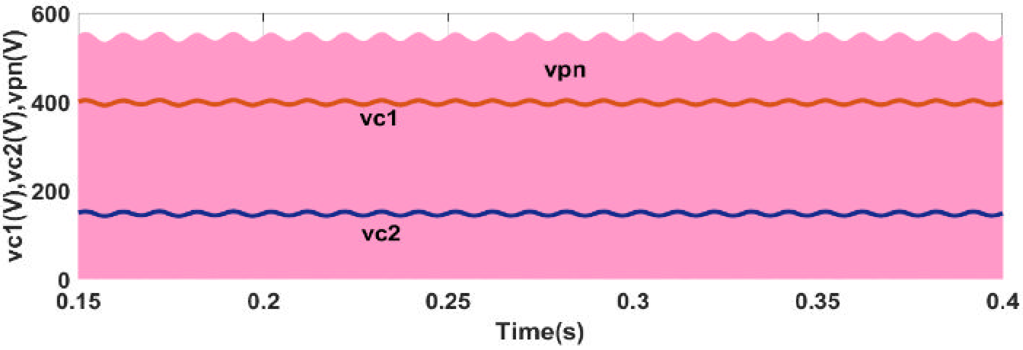

Figure 4.20: Steady-state results of the qZS network voltages.

Figure 4.21 verifies the achievement of the control method to generate a sinusoidal grid current with zero power factor. As it is displayed in this figure, the grid current and voltage are in phase while the grid current reference is $i_g^* = 10\sin(\omega t)$.

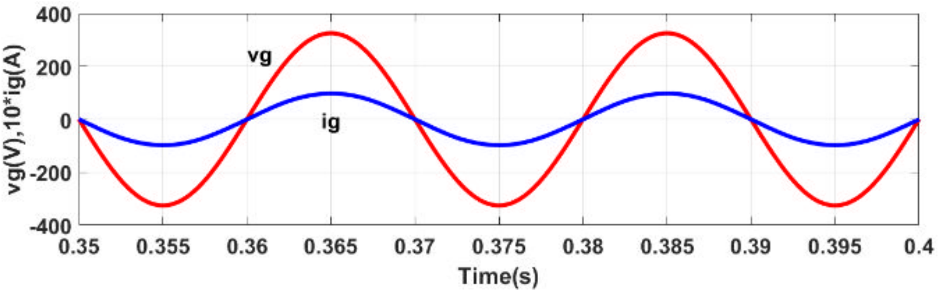

Figure 4.21: Steady-state Grid variables.

The modulation signal and shoot-through duty cycle are displayed in Figure 4.22. According to this figure, the modulation signal is approximately a sinusoidal waveform and shoot through duty cycle is a constant as expected.

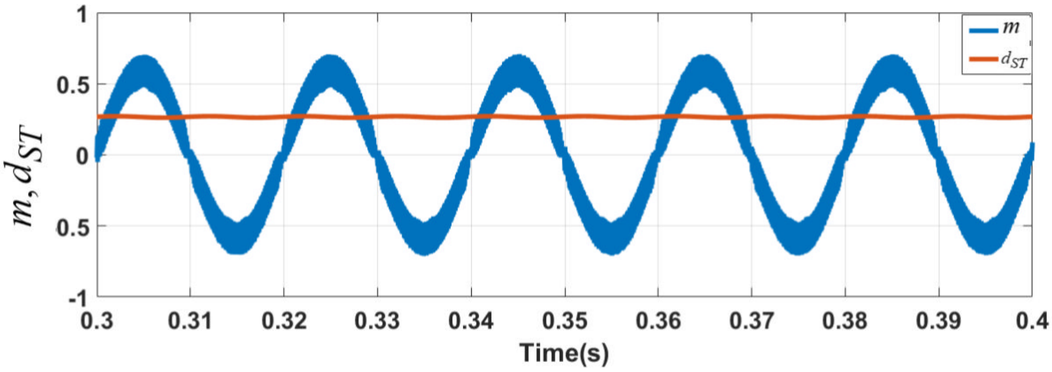

Figure 4.22: Modulation signal (m) and shoot through duty cycle (d_{ST})

The output current of the inverter accompanying its reference in the steady-state are revealed in Figure 4.23. The tracking goal is achieved successfully while generating the reference is also fulfilled without error that verifies the effectiveness of the PR controller in regulating ac waveforms.

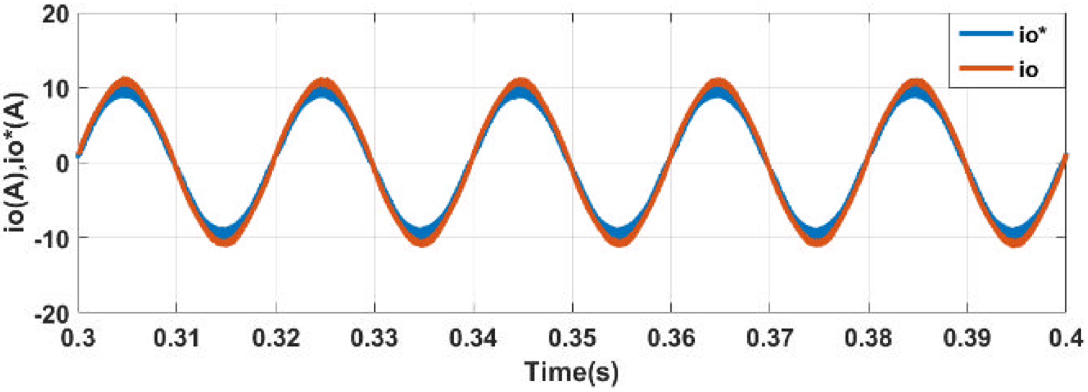

Figure 4.23: Inverter output current and its reference in the steady-state.

The performance of the system is inspected for a sudden variation in i_g^* from 10A to 15A in Figure 4.24. The dc side capacitor voltage in Figure 4.24 (a) is not affected from this variation and tracks its reference value. On the other hand, increasing the grid current leads to increment in (i_o) and (i_{L_1}) as shown in Figure 4.24(b). However, they stabilize to the new reference successfully after the transition period. Figure 4.24(c) shows the fixed switching frequency performance of the control method under a step change in i_g. Dynamic responses of the system variables for a sudden variation in V_{C1}^* from 400V to 500V is displayed in Figure 4.25. Figure 4.25(a) shows the dc side variables due to the step change in V_{C1}^*. It should be mentioned that the value of i_{L_1} is multiplied by 30 for displaying it better in Figure 4.25(a). Therefore, the spike observed in i_{L_1} is a small value and is disappeared in a short time and i_{L_1} returns to its reference. The effect of a sudden change in V_{C1}^* on the control input is inspected in Figure 4.25(b). The shoot-through duty cycle is increased which is reasonable due to the rise of V_{C1}^* and the modulation signal is reduced to control the variables in ac side.

Figure 4.25(c) shows i_o and i_o^* which verifies that the control method is quite successful in forcing i_o to track its reference after an abrupt change in V_{C1}^*.

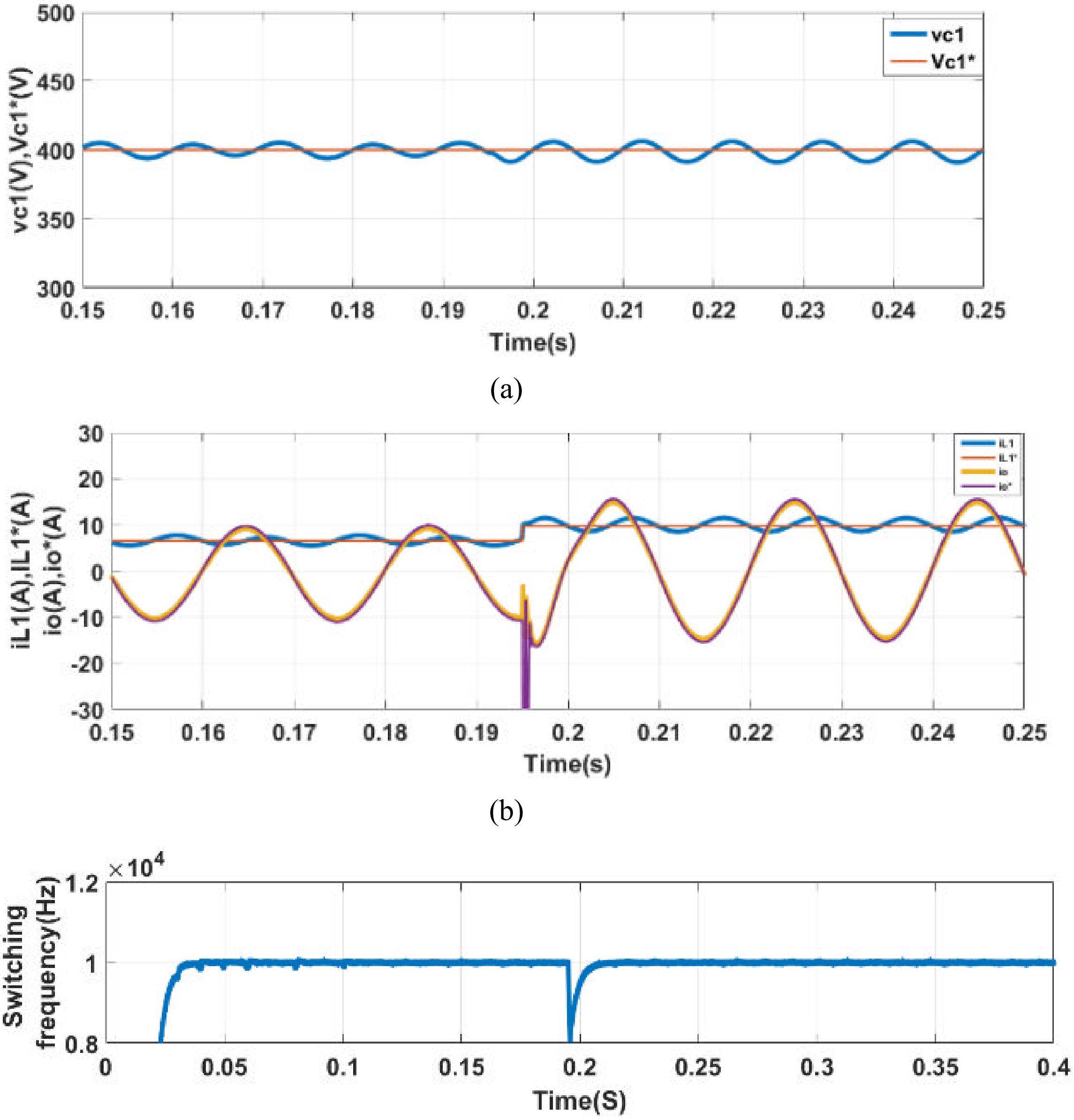

(a)

(b)

(c)

Figure 4.24: Dynamic responses of v_{C_1} ,i_o , i_{L_1} and f_{sw} during a sudden variation in i_g from 10A to 15A (a) v_{C_1} (b) i_o , i_{L_1} (c) f_{sw}

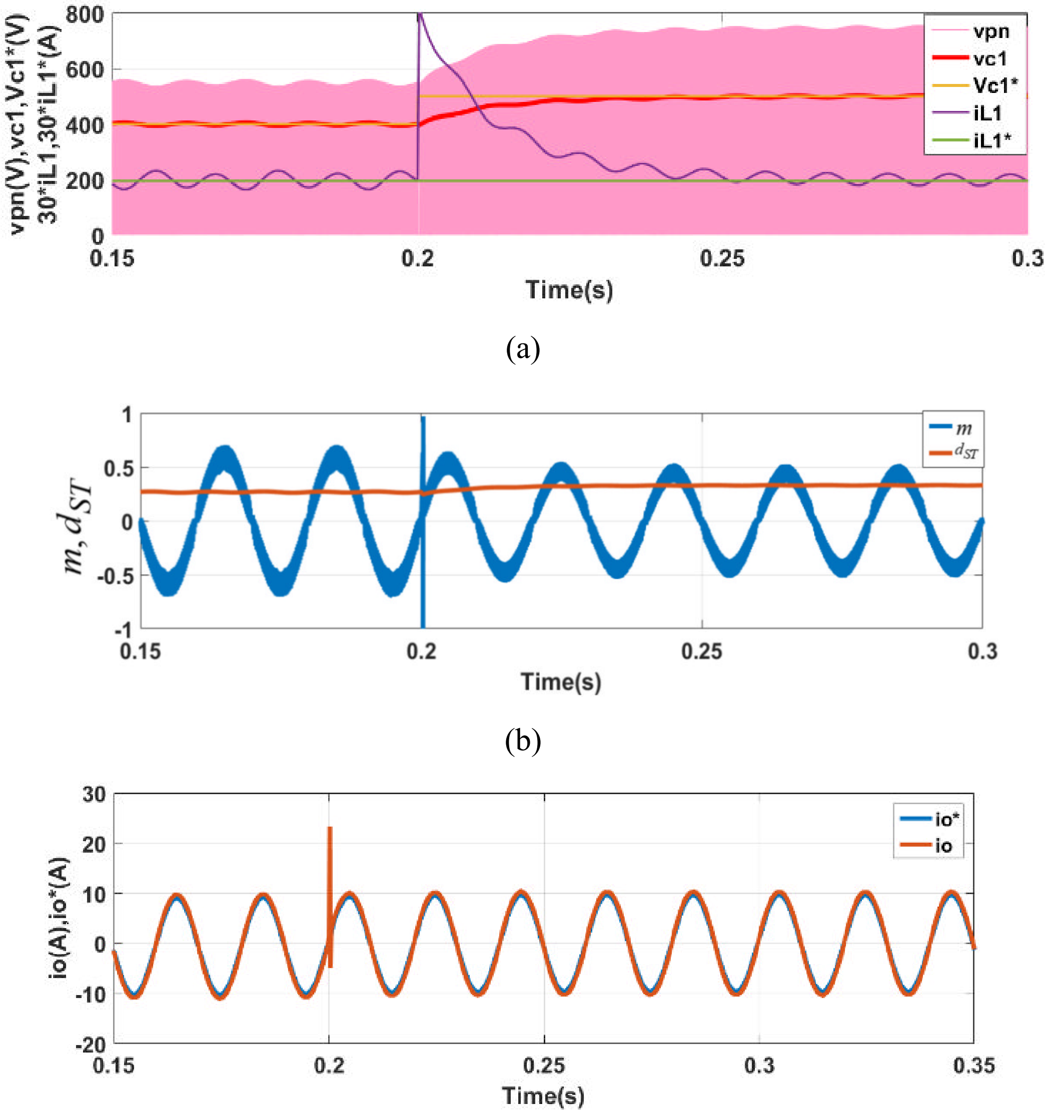

(a)

(b)

(c)

Figure 4.25: Dynamic responses of v_{C_1} and i_{L_1} during a sudden variation in V_{C1}^* from 400V to 500V (a) $v_{C_1}, v_{C_1}^*, i_{L_1}, i_{L_1}^*, v_{pn}$ (b) m and d_{ST}, (c) i_o^* and i_o .

4.4 Conclusion

In this chapter, a MIMO SMC methodology is proposed for the single-phase qZSI operating in the standalone mode and grid-tied mode. The proposed control technique is capable of controlling the whole variables of the qZSI concurrently. Different from the existing control methods devised for qZSI, the proposed control approach does not employ any PI controller in the dc side. Fast dynamic response, strong robustness, and simplicity in implementation are the significant features of the proposed method. Besides, using the PR controller to generate the ac side reference achieves zero steady-state error in the load voltage or grid current. Similarly, achieving a fixed switching frequency is made possible by flattening the sliding manifold function through a boundary layer. The feasibility and performance of the presented control method is validated through simulation and experimental results in the standalone mode under linear and nonlinear load types and simulation results for grid-tied LCL-filtered qZSI.

Chapter 5

MULTI INPUT MULTI OUTPUT BASED SLIDING MODE CONTROL FOR SWITCHED Z-SOURCE INVERTER (SZSI)

5.1 Introduction

This chapter discusses the application of MIMO SMC method to generate modulation signal and shoot through ratio simultaneously to achieve the desired control objectives for a high gain Z-source inverter which is called switched Z-source inverter (SZSI). Like the topology of qZSI, multiple-input and output of the system need an efficient control loop to control all state variables at the same time. Besides, another switch in the topology of SZSI helps the system generate high boost factor at the expense of complication of the control method. In this chapter, the sliding surface functions are used within the boundary layer to mitigate chattering and fix the switching frequency. The simulation results show the efficiency of method in controlling the SZSI.

5.2 State Space Modeling of Standalone SZSI

Figure 5.1 displays a high gain switched-Z-source inverter (SZSI). As it is mentioned in Chapter 2, this novel topology attains a very high boost factor while achieving continuous input current. Same as the other impedance source inverters, it has also two operation modes as shown in Figure 5.2. The SZSI changes its mode by turning switch Q. It means that when the switch Q is turned ON, the inverter is in the ST mode and when the switch Q is turned OFF, the inverter is in the nST mode.

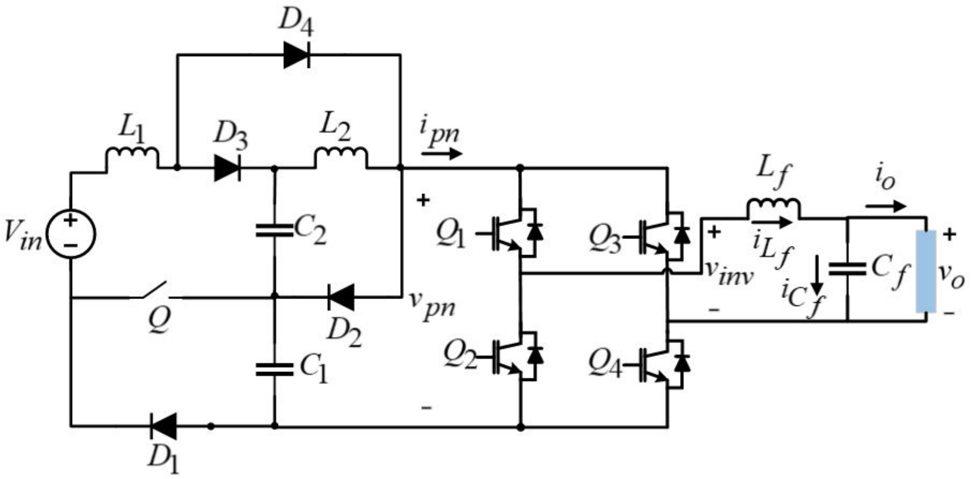

Figure 5.1: Single-phase switched Z-source inverter.

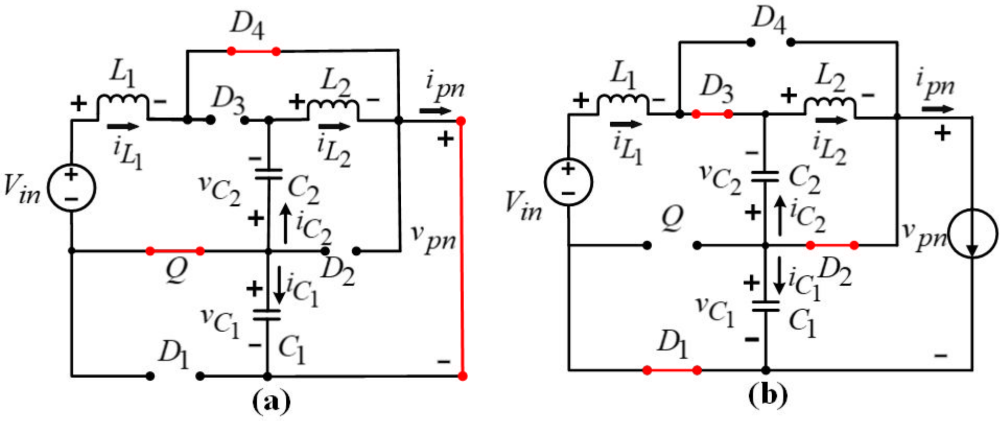

Figure 5.2: Equivalent circuits of the SZSI (a) ST state (b) nST state.

If switch Q is ON, the system goes to ST state as shown in Figure 5.2(a) and the equations of this state can be written as

$$L_1 \frac{di_{L_1}}{dt} = V_{in} + v_{C_1} - (r_L + r_C)i_{L_1} - r_C i_{L_2} \tag{5.1}$$

$$C_1 \frac{dv_{C_1}}{dt} = -i_{L_1} - i_{L_2} \tag{5.2}$$

$$L_2 \frac{di_{L_2}}{dt} = v_{C_1} - v_{C_2} - (r_L + 2r_C)i_{L_2} - r_C i_{L_1} \tag{5.3}$$

$$C_2 \frac{dv_{C_2}}{dt} = i_{L_2} \tag{5.4}$$

where the source voltage, the qZS network capacitor voltages , the qZS network inductor currents and the output voltage of the network are denoted as V_{in} , v_{C_1} , v_{C_2} , i_{L_1} , i_{L_2} and v_{pn} , respectively. Furthermore, $r_{L_1} = r_{L_2} = r_L$ and $r_{C_1} = r_{C_2} = r_C$ are the internal resistances of the dc side inductors and capacitors of the SZS network considered equal for simplicity of analysis. If switch Q is OFF, the system goes to nST state as shown in Figure 5.2(b) and the equations of this state are

$$L_1 \frac{di_{L_1}}{dt} = V_{in} + v_{C_2} - v_{C_1} - (r_L + 2r_C) i_{L_1} + r_C i_{L_2} + r_C i_{pn} \tag{5.5}$$

$$C_1 \frac{dv_{C_1}}{dt} = i_{L_1} - i_{pn} \tag{5.6}$$

$$L_2 \frac{di_{L_2}}{dt} = -v_{C_2} - (r_L + r_C) i_{L_2} + r_C i_{L_1} \tag{5.7}$$

$$C_2 \frac{dv_{C_2}}{dt} = i_{L_2} - i_{L_1} \tag{5.8}$$

By using the state space average method, the average equations in one switching cycle can be written as follows:

$$\begin{aligned} L \frac{di_{L_1}}{dt} &= d_{ST}(V_{in} + v_{C_1} - (r_L + r_C) i_{L_1} - r_C i_{L_2}) \\ &\quad + (1 - d_{ST})(V_{in} + v_{C_2} - v_{C_1} - (r_L + 2r_C) i_{L_1} + r_C (i_{L_2} + i_{pn})) \end{aligned} \tag{5.9}$$

$$C \frac{dv_{C_1}}{dt} = d_{ST}(-i_{L_1} - i_{L_2}) + (1 - d_{ST})(i_{L_1} - i_{pn}) \tag{5.10}$$

$$\begin{aligned} L \frac{di_{L_2}}{dt} &= d_{ST}(v_{C_1} - v_{C_2} - (r_L + 2r_C) i_{L_2} - r_C i_{L_1}) \\ &\quad + (1 - d_{ST})(-v_{C_2} - (r_L + r_C) i_{L_2} + r_C i_{L_1}) \end{aligned} \tag{5.11}$$

$$C \frac{dv_{C_2}}{dt} = d_{ST}(i_{L_2}) + (1 - d_{ST})(i_{L_2} - i_{L_1}) \tag{5.12}$$

where the dc-side capacitors and inductors assumed to have equal values $L_1 = L_2 = L$, $C_1 = C_2 = C$ and d_{ST} is the shoot through duty cycle. Rearranging equations (5-9)-(5-12) and substituting equations (2.22) and (2.23), the state space equations can be reduced to second order as follows

$$\begin{aligned} L\frac{di_{L_1}}{dt} &= v_{C_1}(-d_{ST}^2+3d_{ST}-1)+i_{L_1}(r_C(2d_{ST}^2-2d_{ST}-1)-r_L) \\ &\quad +i_{pn}(r_C(1-d_{ST}))+V_{in} \end{aligned} \tag{5.13}$$

$$C\frac{dv_{C_1}}{dt} = i_{L_1}(d_{ST}^2-3d_{ST}+1)+i_{pn}(d_{ST}-1) \tag{5.14}$$

Therefore, equations (5.13)-(5.14) can be written in matrix form as follows

$$\begin{bmatrix} L\dfrac{di_{L_1}}{dt} \\ C\dfrac{dv_{C_1}}{dt} \end{bmatrix} = \begin{bmatrix} r_C(2d_{ST}^2-2d_{ST}-1)-r_L & (-d_{ST}^2+3d_{ST}-1) \\ (d_{ST}^2-3d_{ST}+1) & 0 \end{bmatrix} \begin{bmatrix} i_{L_1} \\ v_{C_1} \end{bmatrix} + \begin{bmatrix} 1 & (r_C(1-d_{ST})) \\ 0 & (d_{ST}-1) \end{bmatrix} \begin{bmatrix} V_{in} \\ i_{pn} \end{bmatrix} \tag{5.15}$$

The characteristic equation of the SZSI in the Laplace domain can be obtained from the state-space equation as follows

$$s^2+k_1s+k_2=0 \tag{5.16}$$

where

$$k_1 = r_L - \frac{r_C(2d_{ST}^2-2d_{ST}-1)}{r_L}\ , \quad k_2 = \frac{(d_{ST}^2-3d_{ST}+1)^2}{LC} \tag{5.17}$$

The normalized form of a second order characteristic equation is defined as

$$s^2+2\xi\omega_n s+\omega_n^2=0 \tag{5.18}$$

Now, considering (5.16) and (5.18), the squared natural frequency and damping ratio can be written as follows:

$$\omega_n^2 = [(d_{ST}^2-3d_{ST}+1)^2 / LC] \tag{5.19}$$

$$\xi = \frac{(r_L - r_C(2d_{ST}^2 - 2d_{ST} - 1)) / \sqrt{LC}}{2L(d_{ST}^2 - 3d_{ST} + 1)} \tag{5.20}$$

Referring to [80], the condition for the stability of a second order system is $\xi\omega_n > 0$. Inherently, the natural frequency is positive, therefore the damping ratio should be also positive to make the system stable. Henceforth, the satisfaction of the following equation is needed to make the system stable

$$2d_{ST}^2 - 2d_{ST} - 1 < \frac{r_L}{r_C} \tag{5.21}$$

Equation (5.21) reveals that varying the passive components and shoot through duty cycle have effects on the stability of the system.

5.3 Mathematical Model of the System Based on Multiple Inputs

To find the whole state space of the system (dc and ac sides together) the equation of ac side is added, and the following equations can be derived:

$$\begin{aligned} L\frac{di_{L_1}}{dt} &= v_{C_1}(-d_{ST}^2 + 3d_{ST} - 1) + V_{in} \\ C\frac{dv_{C_1}}{dt} &= i_{L_1}(d_{ST}^2 - 3d_{ST} + 1) + i_{pn}(d_{ST} - 1) \\ L_f\frac{di_{L_f}}{dt} &= v_{inv} - mv_{pn} = v_{inv} - mv_{C_1} \end{aligned} \tag{5.22}$$

where is *m* the modulation signal defined as $m = M\sin(\omega t)$ and the internal resistances of the inductors and capacitors are ignored to simplify the derivations. Considering the power balance equation yields [18]

$$v_{pn}i_{pn}(1 - d_{ST}) = v_o i_o = mv_{pn}i_o \quad , \quad i_{pn}(1 - d_{ST}) = mi_o \tag{5.23}$$

Substituting (5.23) in (5.22) and letting $d_{ST}^2 - 3d_{ST} + 1 = v$, the following state-space equation can be obtained:

$$\begin{bmatrix} L\dfrac{di_{L_1}}{dt} \\ C\dfrac{dv_{C_1}}{dt} \\ L_f\dfrac{di_{L_f}}{dt} \end{bmatrix} = \begin{bmatrix} 0 & -v_{C_1} \\ -i_o & i_{L_1} \\ -v_{C_1} & 0 \end{bmatrix} \begin{bmatrix} m \\ v \end{bmatrix} + \begin{bmatrix} V_{in} \\ 0 \\ v_{inv} \end{bmatrix} \tag{5.24}$$

where v and m are the control inputs of the system.

5.4 Multi Input Multi Output (MIMO) Sliding Mode Control Method

I. Sliding Surface Design

The state variables are defined as follows

$$x_1 = I_{L_1}^* - i_{L_1}, \ x_2 = i_o^* - i_o \tag{5.25}$$

where I_{L1}^* and i_o^* represent the references for i_{L_1} and i_o, respectively. The sliding surface manifold and the sliding surface derivative are defined as

$$S = \begin{bmatrix} S_{dc} \\ S_{ac} \end{bmatrix} = \begin{bmatrix} x_1 \\ x_2 \end{bmatrix}, \quad \dot{S} = \begin{bmatrix} \dot{S}_{dc} \\ \dot{S}_{ac} \end{bmatrix} = \begin{bmatrix} \dot{x}_1 \\ \dot{x}_2 \end{bmatrix} \tag{5.26}$$

Likewise, the derivative of state variables are

$$\frac{dx_1}{dt} = 0 - \frac{di_{L_1}}{dt} = -\frac{1}{L}[v(-v_{C_1}) + V_{in}]$$

$$\frac{dx_2}{dt} = \frac{d}{dt}(i_o^* - i_o) = \frac{d}{dt}(i_{L_f}^* - i_{L_f}) = \frac{di_{L_f}^*}{dt} - \frac{1}{L_f}[m(-v_{C_1}) + v_{inv}] \tag{5.27}$$

The dynamics of the system during sliding mode is defined as $\frac{dS}{dt} = 0$, from which the equivalent control can be determined by solving $\frac{dS}{dt} = 0$ as follows

$$v = \frac{V_{in}}{v_{C_1}} = d_{ST}{}^2 - 3d_{ST} + 1$$

$$m = \frac{v_{inv} - L_f \frac{di_{Lf}^*}{dt}}{v_{C_1}} \tag{5.28}$$

where $v = d_{ST}{}^2 - 3d_{ST} + 1$ and m are the equivalent control inputs of the sliding surface manifold.

According to [77], the existence conditions should be satisfied for sliding manifolds to let the state variables reach to the manifold and slide along it. Hence, the existence conditions are defined as

$$S_{dc}\dot{S}_{dc} < 0 \quad , \quad S_{ac}\dot{S}_{ac} < 0 \tag{5.29}$$

The discontinuous control input is given as

$$u = \begin{bmatrix} u_1 \\ u_2 \end{bmatrix} = \begin{bmatrix} 0.5(1 - sign(S_{dc}) \\ sign(S_{ac}) \end{bmatrix} \tag{5.30}$$

where u_1 and u_2 are the discontinuous control inputs. Substituting (5.30) and (5.27) into (5.29) yields

$$S_{dc}(-\frac{1}{L}[0.5(1 - sign(S_{dc})(-v_{C_1}) + V_{in}]) < 0$$

$$S_{ac}(\frac{di_{Lf}^*}{dt} - \frac{1}{L_f}[sign(S_{ac})(-v_{C_1}) + v_{inv}]) < 0 \tag{5.31}$$

Then, the stability conditions can be gained as

$$(i) \Rightarrow S_{dc} > 0 \Rightarrow S_{dc}(-\frac{V_{in}}{L}) < 0$$

$$(ii) \Rightarrow S_{dc} < 0 \Rightarrow S_{dc}(-\frac{1}{L}[V_{in} - v_{C_1}]) < 0$$

$$(iii) \Rightarrow S_{ac} > 0 \Rightarrow S_{ac}(\frac{di_{Lf}^*}{dt} - \frac{1}{L_f}[-v_{C_1} + v_{inv}]) < 0 \tag{5.32}$$

$$(iv) \Rightarrow S_{ac} < 0 \Rightarrow S_{ac}(\frac{di_{Lf}^{*}}{dt} - \frac{1}{L_f}[v_{C_1} + v_{inv}]) < 0$$

Rearranging equation (5.32) gives the boundaries of variables to assure the existence conditions around sliding manifold as follows

$$V_{in} > 0 \, , \, V_{in} < v_{C_1} \quad , \quad \left| v_{Lf}^{*} - v_{inv} \right| < v_{C_1} \tag{5.33}$$

These conditions define an attraction domain of the sliding manifold. Since the sliding function controller doesn't content any control gain to be regulated, the existence conditions are prearranged by the system design. In steady state equation (5.33) is satisfied by the definition of a SZSI. It means that in steady sate, the capacitor voltage (v_{C_1}) is more than the input voltage and the input voltage is always positive and the absolute value of output voltage is less than the dc side capacitor voltage.

II. Fixed Switching Frequency

The same method applied to qZSI in chapter 4, is also utilized for SZSI to alleviate chattering and bound the sliding manifolds in a thin boundary layer to make them appropriate for PWM generation process. Constant boundary layer thicknesses are considered as ϕ_1 and ϕ_2 . The sliding manifolds are approximated inside these boundary layers which are used to generate PWM pulses for the inverter switches.

5.5 Reference Generation for AC and DC Sides

Using boundary layer method leads to a steady state error in load voltage. Achieving zero steady-state in the output voltage can be made by producing the reference inverter output current through a PR controller with the following transfer function

$$H_{PR}(s) = k_{pr} + \frac{2k_r \omega_c s}{s^2 + 2\omega_c s + \omega^2} \tag{5.34}$$

The output voltage error $(v_o^* - v_o)$ is applied to the PR controller and the output is the inverter output current reference $(i_{L_f}^*)$. The output voltage reference is a sinusoidal waveform defined as $v_o^* = V_o \sin(\omega t)$. The desired dynamic and steady state responses of the system are determined by tunning of k_{pr} and k_r. i_o^* can simply be obtained by subtracting the measured capacitor current from $i_{L_f}^*$, as follows

$$i_o^* = i_{L_f}^* - i_{C_f} \tag{5.35}$$

Dc side control input is the dc side sliding manifold which is defined as the dc-side inductor current error. Generating inductor current reference and attaining zero steady sate error in v_{C_1} is made possible via using a cascaded PI controller as following

$$I_{L_1}^* = k_p (V_{C_1}^* - v_{C_1}) + k_i \int (V_{C_1}^* - v_{C_1}) dt \tag{5.36}$$

Where k_p and k_i are the parameters to regulate the best steady sate and dynamic responses.

5.6 Simulation Verification

The block diagram of the presented control approach is shown in Figure 5.3. According to Figure 5.3, the modulation signal and shoot through duty cycle are the outputs of sliding mode control. Matlab/Simulink is used to test the performance and robustness of the proposed control method. The system and control parameters are revealed in Table 5.1.

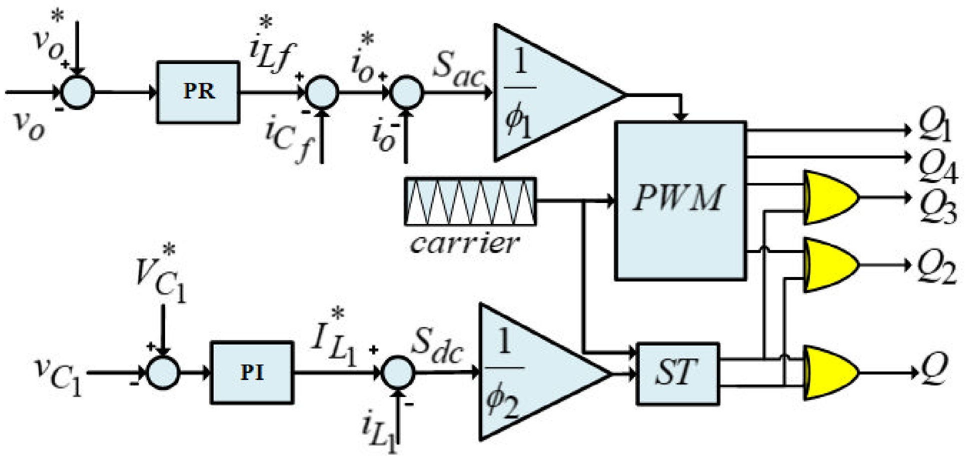

Figure 5.3: Block diagram of the proposed control approach.

Table 5.1: System and Control Parameters

Parameter	**Value**
Input dc voltage (V_{in})	150 V
SZS network inductances ($L_1 = L_2 = L$)	2mH
SZS network capacitances ($C_1 = C_2 = C$)	220 μF
Filter inductance (L_f)	2mH
Filter capacitance (C_f)	9 μF
Amplitude of output voltage reference (V_o^*)	200 V
Dc side capacitor voltage reference ($V_{C_1}^*$)	500V
Nominal frequency (f_g)	50Hz
Switching frequency (f_{sw})	10kHz
Amplitude of the carrier (V_p)	1V
Proportional and resonant gains of PR controller (k_{pr}, k_r)	0.6, 3000
Proportional and resonant gains of PI controller (k_p, k_i)	1, 20
Cut off frequency (ω_c)	1
Boundary layer thickness (ϕ_1, ϕ_2)	0.7, 0.1

The boost factor of SZS network can be calculated by using equation (2.14) which is $v_{pn} = v_{C_1} = \frac{V_{in}}{(d_{ST}{}^2 - 3d_{ST} + 1)} = BV_{in}$. The steady-state values of input and output voltages of SZS network (V_{in} and v_{pn}) are shown in Figure 5.4. Substituting the relevant values in Table 5.1 into equation (2.14), one can calculate the boost factor and shoot through duty cycle as 3.33 and 0.255, respectively. These values agree well with the simulation results shown in Figure 5.4.

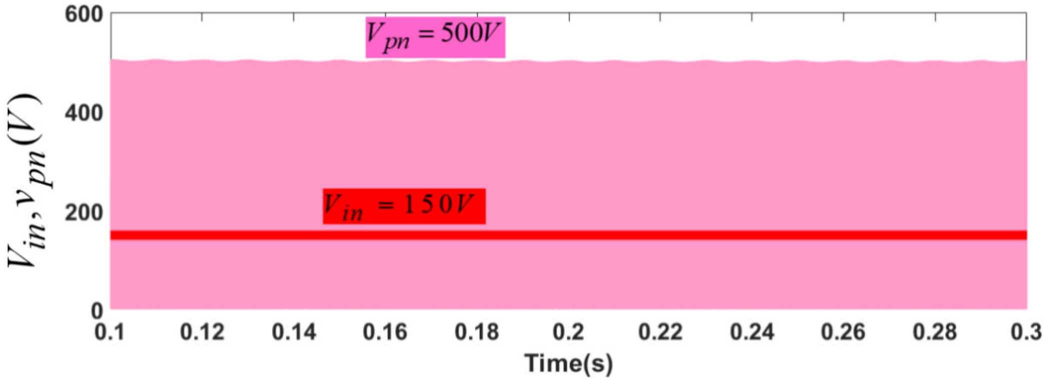

Figure 5.4: Input and output voltages of SZS network in the steady-state.

The dc side capacitor voltages (v_{C_1}, v_{C_2}) and output voltage of the SZS network (v_{pn}) in steady-state is displayed in Figure 5.5. Equality of v_{C_1} and v_{pn} confirms the agreement of simulation and theory in equation (2.14). The inherent double frequency ripple is also obvious in Figure 5.5.

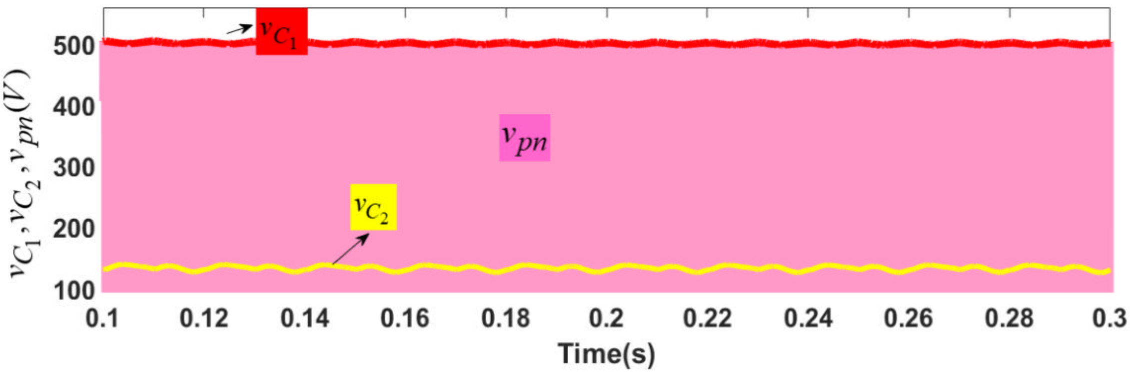

Figure 5.5: Capacitor and output voltages of the SZS network in the steady-state.

The steady-state output voltage and current under linear and nonlinear loads are displayed in Figure 5.6. The linear load is supposed to be a resistive load and the nonlinear load is assumed to be diode-rectifier with parallel RC at its output (R=60Ω and C=4000 μF). The output current is sinusoidal under the linear load as shown in Figure 5.6(a). Both output voltages are also sinusoidal under linear and nonlinear load in Figure 5.6(a) and (b) which confirms the effectiveness of the control approach leading to a low THD in the output voltage. The THDs of output voltage under linear and nonlinear loads are calculated to be 0.22% and 0.7%, respectively. Dynamic responses of the ac and dc side variables for a step change in the linear load at t=0.205 are shown in Figure 5.7. It can be seen that the output voltage in Figure 5.7(a) is almost not affected from the variation in the load. Furthermore, the dc-side capacitor voltage follows its reference due to variation of load as shown in Figure 5.7(b).

The use of boundary layer method removes the discontinuity in the control signal and makes it comparable with the triangular carrier signal which results in fixed switching frequency. The switching frequency of inverter is shown in Figure 5.8. Except for the initial time, the switching frequency is always fixed and is not affected from the load change.

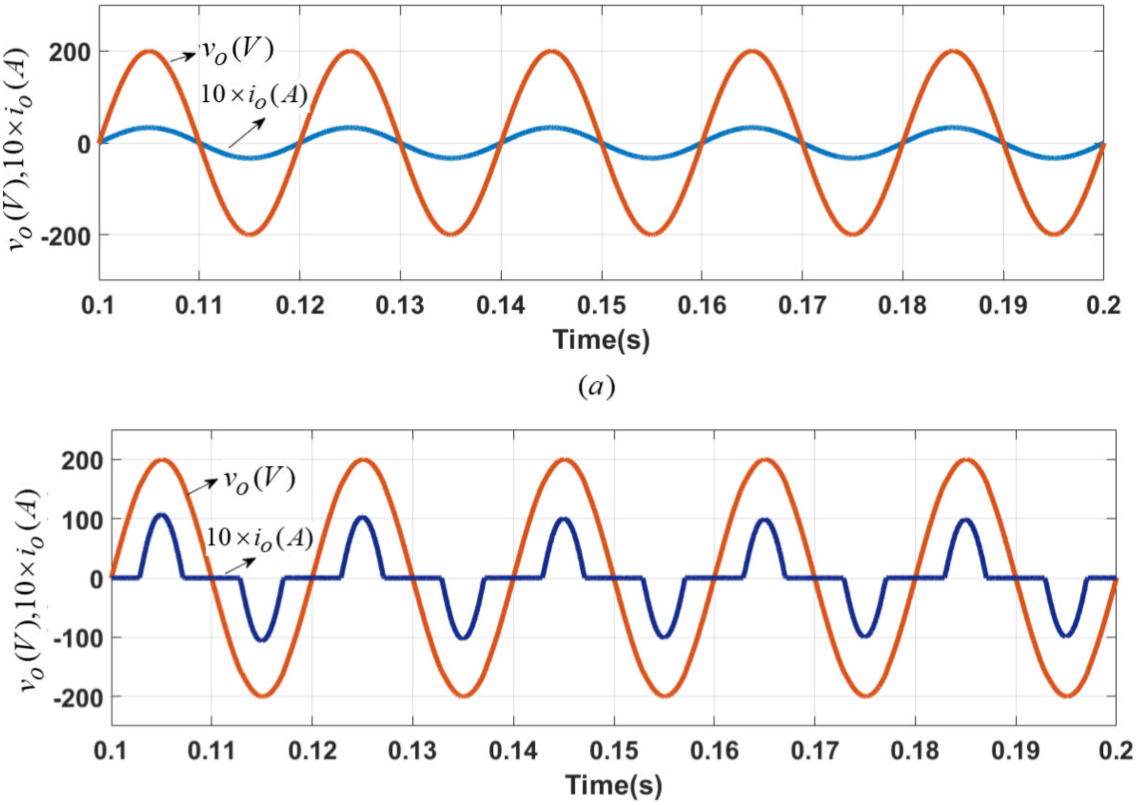

(a)

(b)

Figure 5.6: Output current and voltage (a) with linear load (b) with nonlinear load.

The effect of a step variation in $V_{C_1}^*$ from 500V to 600V on all the variables of the system is displayed in Figure 5.9. According to Figures 5.9(a) and (b), the control of the variables of the SZS network is accomplished effectively with the presented technique. It is worth mentioning that the inductor current is not affected (except for the short transient period) from the step change in the capacitor voltage.

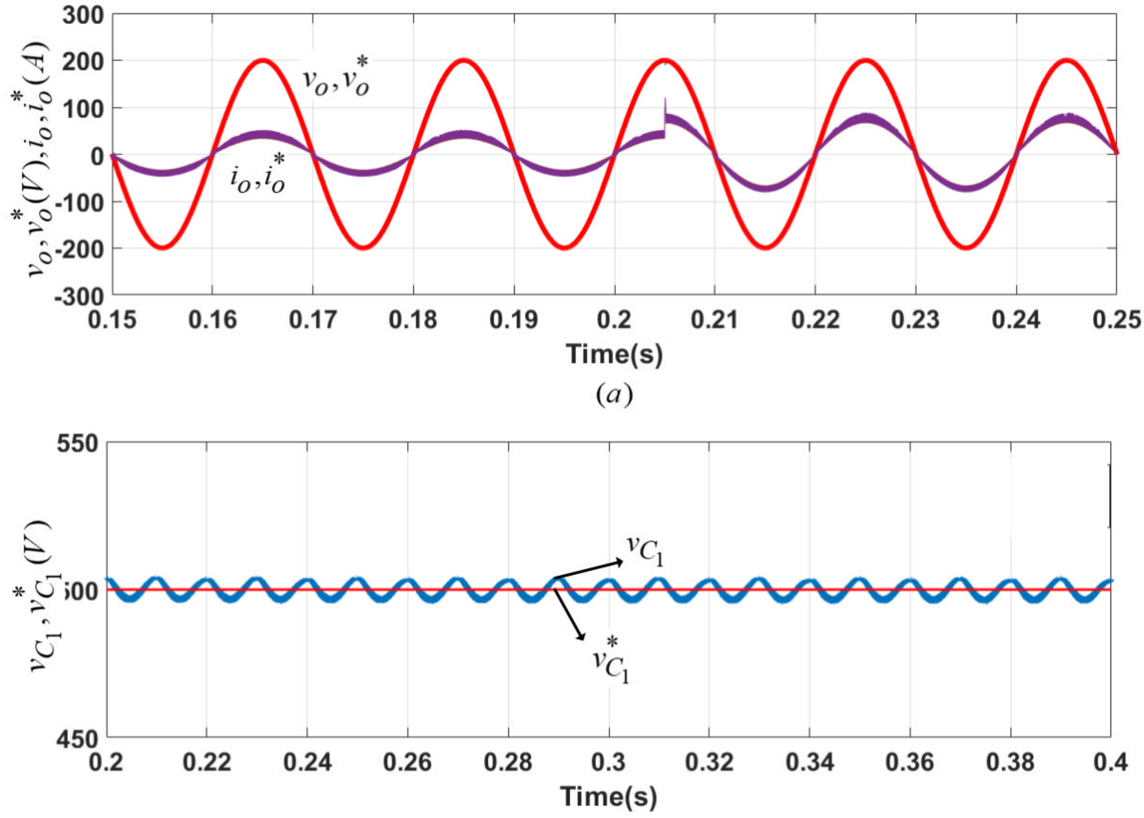

(*a*)

(*b*)

Figure 5.7: A step change under linear load at t=0.205s (a) Output current and voltage and their references (b) v_{C_1} and $V_{C_1}^*$.

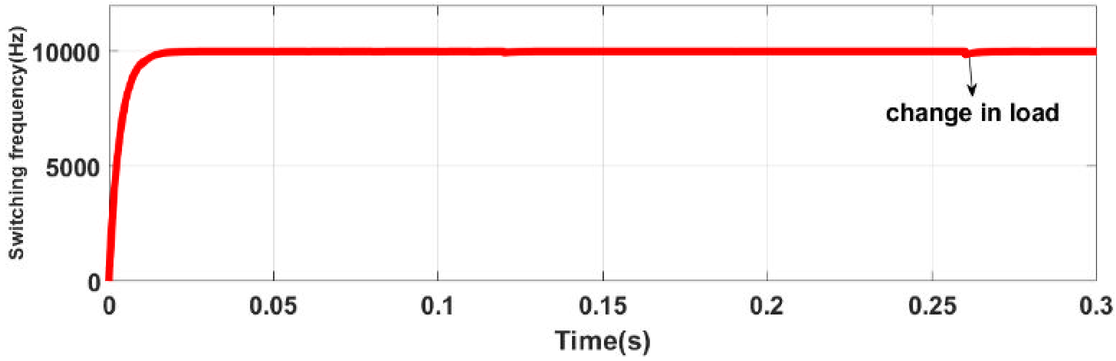

Figure 5.8: Switching frequency due to a step change in load.

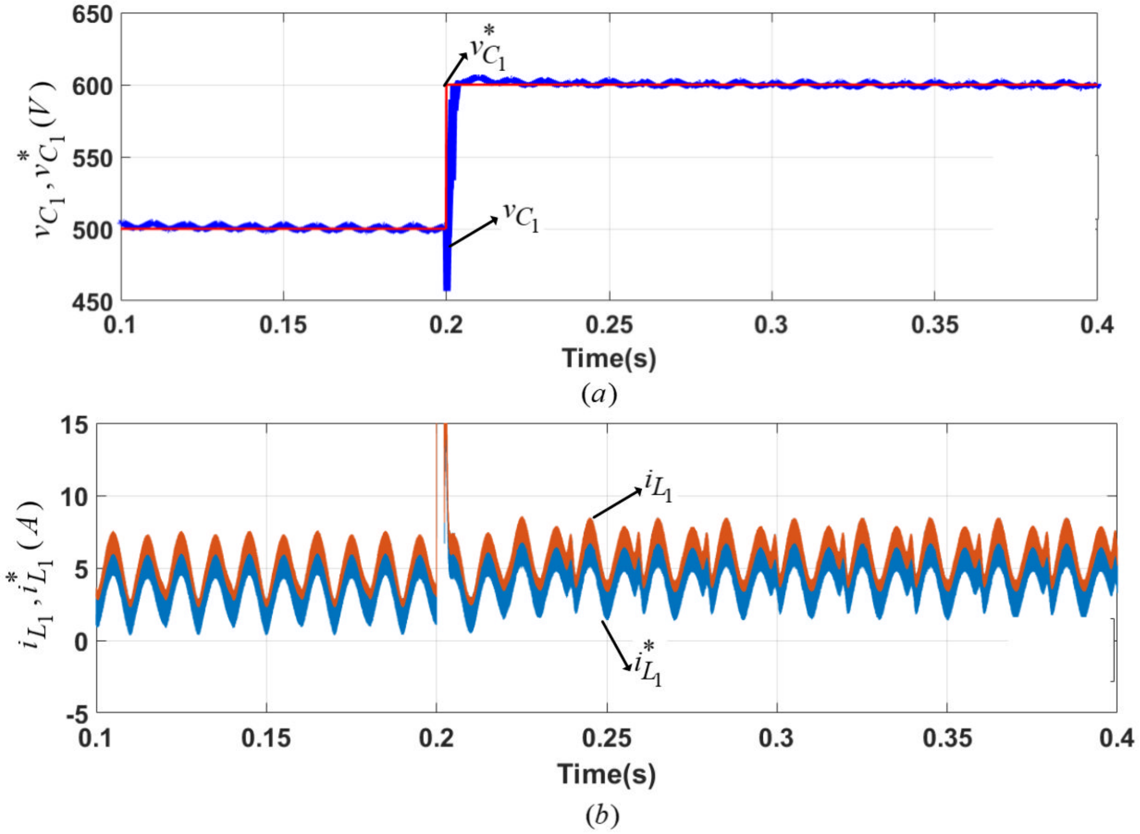

Figure 5.9: A step change in capacitor voltage reference at t=0.2s (a) Dynamic responses of capacitor voltage and its reference (b) Dynamic responses of inductor current and its reference.

Figure 5.10 displays modulation signal (m) and shoot through duty cycle (d_{ST}). According to this result, the modulation signal is a sinusoidal signal which varies between -1 and +1 and shoot through duty cycle is a constant which is between 0 and +1.

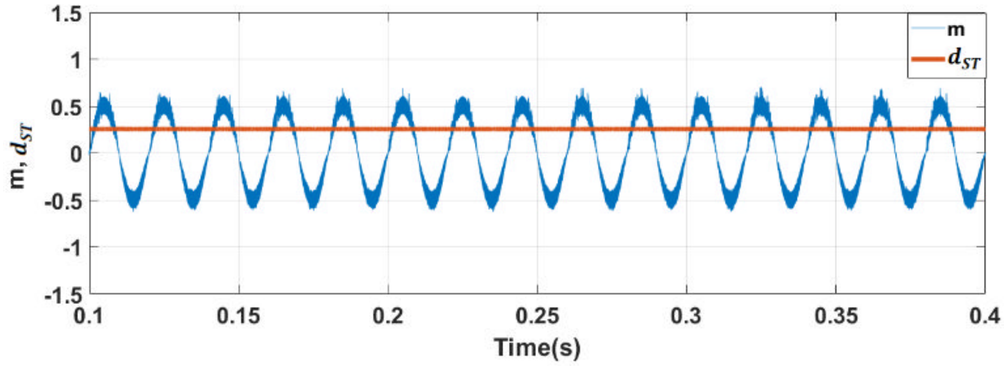

Figure 5.10: Modulation signal (*m*) and shoot through duty cycle of the control approach in steady state

5.7 Conclusion

This chapter discusses the application of the MIMO SMC approach for the high voltage gain switched-Z-source inverter. The switched-Z-source inverter is a novel topology with high boost factor and continuous input current. With these features, the switched-Z-source inverter could find a place in the applications where the power is transferred from RES to the load or grid. The proposed MIMO SMC not only provides a combined control of dc- and ac-side variables into a compact form of equations, but also presents simple sliding manifolds for calculation and implementation without using derivative, integral or even coefficients. Additionally, the operation of inverter at fixed switching frequency is assured with the continuous control signal which is obtained by smoothing the sliding manifolds in a narrow boundary layer. The simulation results under linear and nonlinear loads confirm the efficiency of the proposed control approach in attaining the anticipated control objections such as sinusoidal output voltage with low THD, fast dynamic response, zero steady-state error in tracking dc- and ac-side variables and a fixed switching frequency.

Chapter 6

CONCLUSIONS AND FUTURE WORK

This thesis proposes control approaches with distinct features to apply on impedance source inverters and especially qZSI. The first control approach is the MBCC method with mitigation of dc-side inductor DFR applied on the grid-tied LCL filtered qZSI. This method uses the relation between dc side variables and generates a ripple free inductor current reference, then enforces the inductor current to follow its reference by using the simple boost control method. The inductor current ripple is damped through the proposed approach. The MBCC approach with active damping and virtual time constant adjusts the inverter current to track its reference as desired. Moreover, an active damping method is also proposed in the close loop control by adjusting the ac side current reference.

The second control approach proposed in the thesis is MIMO SMC approach applied on single- phase qZSI and single-phase SZSI. This approach has the ability for controlling dc and ac side variables of the impedance source inverters simultaneously. According to the obtained results, the proposed approach achieves fast dynamic response, strong robustness, and simplicity in implementation. Furthermore, the steady-state error in the load voltage of standalone mode or grid current in grid-tied mode is removed using PR controller in the ac side. Also, the fixed switching frequency results in less EMI. The feasibility and performance of the proposed control approach is validated through experimental results under linear and nonlinear load types in standalone mode and validated through simulation results in MATLAB/SIMULINK in grid-tied qZSI.

The proposed MIMO SMC approach is also applied to the high voltage gain SZSI. SZSI is a novel topology with high boost factor while achieving continuous input current which is a good choice for connecting renewable energy sources to the load or grid. The proposed MIMO SMC not only provides a combined control of dc and ac-side variables into a compact form of equations, but also presents simple sliding manifolds for calculation and implementation without using derivative, integral or even coefficients. Additionally, the fixed switching frequency of the inverter is achieved with the help of boundary layer method. The simulation results under linear and nonlinear loads confirm the efficiency of the proposed control approach in attaining the anticipated control aims such as sinusoidal output voltage with low THD, fast dynamic response, zero steady-state error in tracking dc- and ac-side variables and a fixed switching frequency.

Introducing impedance source inverters has opened a new horizon in the field of power electronics and drives and they have a wide range of applications. Novel topologies have been presented with the aim of improving the reliability and performance of the system. Designing appropriate and simple control methods based on nonlinear control and especially SMC for the novel topologies can be the future work of this thesis.

On the other hand, various methods for fixing the frequency of sliding mode control are presented in literate that boundary layer method is one of them. Applying other methods to mitigate the chattering and fixing the switching frequency is another plan.

The boundary layer method presented in Chapter 4 is a constant boundary layer value and can be selected as a time varying boundary layer thickness which is another idea to apply on impedance source inverters and can lead to less steady state error and better dynamic response.

There are, of course, some limitations in this study, the foremost of which is not considering a harmonic polluted grid. Studying a harmonic polluted grid-tied qZSI and verifying the successful performance of the control method in such a case can validate the strong robustness of the method. However, lack of facilities in experimental lab can limit studies on harmonic detection. Therefore, this topic is also another open issue that can be worked on in the future.

REFERENCES

[1] M. H. Rashid. (1993). Power electronics, 2nd ed. *Englewood Cliffs, NJ: Prentice-Hall.*

[2] F. Z. Peng. (Mar./Apr 2003). “Z-source inverter,” *IEEE Trans. Ind. Appl.*, vol. 39, no. 2, pp. 504–510.

[3] Y. P. Siwakoti, F. Z. Peng, F. Blaabjerg, et al. (2015) “Impedance-source networks for electric power conversion part I: a topological review,” *IEEE Trans. Power Electron,* vol. 30, no. 2, pp. 699–716.

[4] H. Abu-Rub, M. Malinowski, and K. Al-Haddad. (2014).” Power Electronics for Renewable Energy Systems, Transportation and Industrial Applications,” *John Wiley & Sons Ltd., Hoboken, NJ.*

[5] Y. Liu, H. Abu-Rub, B. Ge, et al. (2016)” Impedance source power electronic converters,” *John Wiley & Sons Ltd., Hoboken, NJ.*

[6] Y. Liu, H Abu-Rub, and B. Ge. (2014). “Z-source/quasi-Z-source inverters – derived networks, modulations, controls, and emerging applications to photovoltaic conversion,” *IEEE Ind. Electron*, vol. 8, no. 4, pp. 32–44.

[7] H. Komurcugil, S. Bayhan, F. Bagheri, O. Kukrer and H. Abu-Rub. (2018). “Model-based current control for single-phase grid-tied quasi-Z-source inverters

with virtual time constant," *IEEE Trans. Ind. Electron*, vol. 65, no. 10, pp. 8277–8286.

[8] J. Anderson and F. Z. Peng. (2008). "Four quasi-Z-source inverters," in *Proc. of 39th IEEE Annual Power Electron. Spec. Conf.,* Rhodes, Greece, pp. 2743–2749.

[9] B. Ge, H. Abu-Rub, F. Peng, Q. Lei, A. de Almeida, F. Ferreira, D. Sun, and Y. Liu. (2013). "An energy stored quasi-Z-source inverter for application to photovoltaic power system," *IEEE Trans. Ind. Electron.*, vol. 60, no. 10, pp. 4468–4481.

[10] H. Komurcugil, S. Bayhan and H. Abu-Rub. (2017). "Lyapunov-function-based control method for three-phase grid-tied quasi-Z-source inverter with LCL filter," in *Proc. of 19th European Conference on Power Electronics and Applications*, pp. 1-9.

[11] Y. Li, S. Jiang, J. C. Rivera, and F. Z. Peng. (2013). "Modeling and control of quasi-Z-source inverter for distributed generation applications," *IEEE Trans. Ind. Electron,* vol. 60, no. 4, pp. 1532-1541.

[12] J. Liu, S. Jiang, D. Cao, and F. Z. Peng. (2013). "A digital current control of quasi-Z-source inverter with battery," *IEEE Trans. Ind. Inf.,* vol. 9, no. 2, pp. 928-937.

[13] D. Sun, B. Ge, X. Yan, D. Bi, H. Zhang, Y. Liu, H. Abu-Rub, L. Ben. Brahim, and F. Z. Peng. (2014). "Modeling, impedance design, and efficiency analysis

of quasi-Z source module in cascaded multilevel photovoltaic power system, "*IEEE Trans. Ind. Electron.*, vol. 61, no. 11, pp. 6108-6117.

[14] B. Ge, Y. Liu, H. Abu-Rub, R. S. Balog, F. Z. Peng, H. Sun, and X. Li. (2016). "An active filter method to eliminate DC-side low-frequency power for a single-phase quasi-Z-source inverter," *IEEE Trans. Ind. Electron.,* vol. 63, no. 8, pp. 4838-4848.

[15] Y. Liu, B. Ge, H. Abu-Rub, H. Sun, F. Z. Peng, and Y. Xue. (2016). "Model predictive direct power control for active power decoupled single-phase quasi-Z-source inverter," *IEEE Trans. Ind. Inf.,* vol. 12, no. 4, pp. 1550-1559.

[16] Y. Zhou, and H. Li. (2016). "A single-phase PV quasi-Z-source inverter with reduced capacitance using modified modulation and double-frequency ripple suppression control," *IEEE Trans. Power Electron*., vol. 31, no. 3, pp. 2166-2173.

[17] Y. Liu, B. Ge, H. Abu-Rub, and H. Sun. (2016). "Hybrid pulse width modulated single-phase quasi-Z-source grid-tie photovoltaic power system," *IEEE Trans. Ind. Inf.,* vol. 12, no. 2, pp. 621-632.

[18] B. Ge, Y. Liu, H. Abu-Rub, R. S. Balog, F. Z. Peng, S. McConnell, and X. Li. (2016). "Current ripple damping control to minimize impedance network for single-phase quasi-Z source inverter system," *IEEE Trans. Ind. Inf.,* vol. 12, no. 3, pp. 1043-1054.

[19] M. Shen, J. Wang, A. Joseph, F. Z. Peng, L. M. Tolbert, and D. J. Adams. (2006)." Constant boost control of the Z-source inverter to minimize current ripple and voltage stress," *IEEE Trans. Ind. Appl.*, vol. 42, no. 3, pp. 770–778.

[20] Y. Sun, Y. Liu, M. Su, W. Xiong, and J. Yang. (2016). "Review of active power decoupling topologies in single-phase systems," *IEEE Trans. Power Electron.*, vol. 31, no. 7, pp. 4778–4794.

[21] M. A. Vitorino, L. F. S. Alves, R. Wang, and M. B. de R. Correa. (2017). "Low-frequency power decoupling in single-phase applications: A comprehensive overview," *IEEE Trans. Power Electron.,* vol. 32, no. 4, pp. 2892–2912.

[22] Y. Tang, Z. Qin, F. Blaabjerg, and P. C. Loh. (2015). "A dual voltage control strategy for single-phase PWM converters with power decoupling function," *IEEE Trans. Power Electron.*, vol. 30, no. 12, pp. 7060–7071.

[23] S. Li, W. Qi, and S. C. Tan. (2018). "Enhanced automatic-power-decoupling control method for single-phase AC-to-DC converters," *IEEE Trans. Power Electron.,* vol. 33, no. 2, pp. 1816-1828.

[24] Y. Liu, B. Ge, H. Abu-Rub, and H. Sun. (2016). "Hybrid pulse width modulated single-phase quasi-Z-source grid-tie photovoltaic power system," *IEEE Trans. Ind. Inf.,* vol. 12, no. 2, pp. 621-632.

[25] R. P. Alzola, M. Liserre, F. Blaabjerg, R. Sebastion, J. Dannehl, and F. W. Fuchs. (2013) "Analysis of the passive damping losses in LCL-filter-based grid converters," *IEEE Trans. Power Electron.,* vol. 28, no. 6, pp. 2642–2646.

[26] M. Castilla, J. Miret, J. Matas, L. G. de Vicuna, and J. M. Guerrero. (2009). "Control design guidelines for single-phase grid-connected photovoltaic inverters with damped resonant harmonic compensators," *IEEE Trans. Ind. Electron.*, vol. 56, no. 11, pp. 4492-4501.

[27] D. Pan, X. Ruan, C. Bao, W. Li, and X. Wang. (2014). "Capacitor-current feedback active damping with reduced computation delay for improving robustness of LCL-type grid-connected inverter," *IEEE Trans. Power Electron.*, vol. 29, no. 7, pp. 3414–3427.

[28] J. Xu, S. Xie, and T. Tang. (2014). "Active damping-based control for grid connected LCL-filtered inverter with injected grid current only," *IEEE Trans. Ind. Electron.*, vol. 61, no. 9, pp. 4746–4758.

[29] H. Komurcugil, S. Ozdemir, I. Sefa, N. Altin, and O. Kukrer. (2016). "Sliding-mode control for single-phase grid-connected LCL-filtered VSI with double-band hysteresis scheme," *IEEE Trans. Ind. Electron.*, vol. 63, no. 2, pp. 864–873.

[30] H. Komurcugil, S. Bayhan, and H. Abu-Rub. (2017). "Variable and fixed switching frequency-based HCC methods for grid-connected VSI with active

damping and zero steady-state error," *IEEE Trans. Ind. Electron.*, vol. 64, no. 9, pp. 7009–7018.

[31] H. Komurcugil, N. Altin, S. Ozdemir, and I. Sefa. (2016). "Lyapunov-function and proportional-resonant-based control strategy for single-phase grid-connected VSI with LCL filter," *IEEE Trans. Ind. Electron.*, vol. 63, no. 5, pp. 2838–2849.

[32] C. A. Busada, S. G. Jorge, and J. A. Solsona. (2015). "Full-state feedback equivalent controller for active damping in LCL filtered grid connected inverters using a reduced number of sensors," *IEEE Trans. Ind. Electron.*, vol. 62, no. 10, pp. 5993–6002.

[33] F. Liu, Y. Zhou, S. Duan, J. Yin, B. Liu, and F. Liu. (2009). "Parameter design of a two-current-loop controller used in a grid-connected inverter system with LCL filter," *IEEE Trans. Ind. Electron.,* vol. 56, no. 11, pp. 4483–4491.

[34] Y. Liu, B. Ge, H. Abu-Rub, and F. Z. Peng. (2013). "Control system design of battery-assisted quasi-Z-source inverter for grid-tie photovoltaic power generation," *IEEE Trans. Sustainable Energy,* vol. 4, no. 4, pp. 994-1001.

[35] P. Iniyaval and S. R. Karthikeyan. (2016). "Fuzzy logic based quasi Z-source cascaded multilevel inverter with energy storage for photovoltaic power generation system," in *Proc. Int. Conf. Emerge. Trends Eng., Technol. Sci.,* Pudukkottai, India, pp. 1–5.

[36] H. Abu-Rub, A. Iqbal, Sk. M. Ahmed, F. Z. Peng, Y. Li, and G. Baoming. (2013). “Quasi-Z-source inverter-based photovoltaic generation system with maximum power tracking control using ANFIS,” *IEEE Trans. Sustainable energy*, vol. 4, no. 1, pp. 11-20.

[37] H. Rostami and D. A. Khaburi. (2010). “Neural networks controlling for both the DC boost and AC output voltage of Z-source inverter,” in *Proc. 1st Power Electron. Drive Syst. Technol. Conf.*, pp. 135–140.

[38] A. Ayad, P. Karamanakos, and R. Kennel. (2017). “Direct model predictive current control strategy of quasi-Z-source inverters,” *IEEE Trans. Power Electron*, vol. 32, no. 7, pp. 5786-5801.

[39] S. Bayhan, M. Trabelsi, H. Abu-Rub, and M. Malinowski. (2017). “Finite-control-set model-predictive control for a quasi-Z-source four-leg inverter under unbalanced load condition*,” IEEE Trans. Ind. Electron*, vol. 64, no. 4, pp. 2560-2569.

[40] P. Karamanakos, A. Ayad, and R. Kennel. (2018). “A variable switching point predictive current control strategy for quasi-Z-source inverters,” *IEEE Trans. Ind. Appl.,* vol. 54, no. 2, pp. 1469-1480.

[41] Y. Liu, H. Abu-Rub, Y. Xue and F. Tao. (2018). “A discrete-time average model-based predictive control for a quasi-Z-source inverter,” *IEEE Trans. Ind. Electron,* vol. 65, no. 8, pp. 6044-6054.

[42] U. K. Shinde, S. G. Kadwane, S. P. Gawande, M. J. B. Reddy, and D. K. Mohanta. (2017). “Sliding mode control of single-phase grid-connected quasi-Z-source inverter,” *IEEE Access,* vol. 5, pp. 10232–10240.

[43] B. Xu, X. Ran. (2018). “Sliding mode control for three-phase quasi-Z-source inverter,” IEEE Access, vol. 6, pp. 60318–60328.

[44] A. Zakipour, S. S. Kojori, and M. T. Bina. (2017).” Closed-loop control of the grid-connected Z-source inverter using hyper-plane MIMO sliding mode,” *IET Power Electronics*, vol. 10, no. 15, p. 2229-2241.

[45] V. Utkin, J. Guldner, and J. Shi. (2009). Sliding Mode Control in Electromechanical Systems, *CRC press,* second edition.

[46] S. S. Nag and S. Mishra. (2014). “Current–fed switched inverter,” *IEEE Trans. Ind. Electron.*, vol. 61, no. 9, pp. 4680–4690.

[47] M. K. Nguyen, T. V. Le, S. J. Park, and Y. C. Lim. (2015). “A class of quasi switched boost inverters,” *IEEE Trans. Ind. Electron.,* vol. 62, no. 3, pp. 1526–1536.

[48] M. K. Nguyen, Y. C. Lim, and S. J. Park. (2015). “A comparison between single phase quasi-Z-source and quasi-switched boost inverters,” *IEEE Trans. Ind. Electron.,* vol. 62, no. 10, pp. 6336–6344.

[49] A. V. Ho, T.W. Chun, and H. G. Kim. (2015). "Extended boost active-switched-capacitor/switched-inductor quasi-Z-source inverters," *IEEE Trans. Power Electron.,* vol. 30, no. 10, pp. 5681–5690.

[50] M. K. Nguyen, T. V. Le, S. J. Park, Y. C. Lim, and J. Y. Yoo. (2015). "Class of high boost inverters based on switched-inductor structure," *IET Power Electron*., vol. 8, no. 5, pp. 750–759.

[51] E. Babaei, E. S. Asl, M. H. Babayi, and S. Laali. (2016). "Developed embedded switched-Z-source inverter," *IET Power Electron*., vol. 9, no. 9, pp. 1828-1841.

[52] M. K. Nguyen, T. D. Duong, Y. C. Lim and Y. G. Kim. (2018). "Switched capacitor quasi-switched boost inverters," *IEEE Trans. Ind. Electron*., vol. 65, no. 6, pp. 5105–5113.

[53] M. H. B. Nozadian, E. Babaei, S. H. Hosseini, and E. S. Asl. (2017). "Steady-state analysis and design considerations of high voltage gain switched Z-source inverter with continuous input current," *IEEE Trans. Ind. Electron*., vol. 64, no. 7, pp. 5342–5350.

[54] J. Anderson and F. Peng, "A class of quasi-Z-source inverters. (2008)." in *Proc. IEEE Industry Applications Society Annual Meeting*, pp. 1–7.

[55] J. Anderson and F. Z. Peng. (2008). "Four quasi-Z-source inverters," in *Proc. IEEE Power Electronics Specialists Conf., PESC*, June 15–19.

[56] O. Ellabban and H. M. Abu-Rub. (2016).” Z-Source inverter topology improvements review,” *IEEE Industrial Electronics Magazine*, pp. 6–24.

[57] F. Guo, L. Fu, C.H. Lin, C. Li, W. Choi, and J. Wang. (2013). “Development of an 85-kW bidirectional quasi-Z-source inverter with DC-link feed-forward compensation for electric vehicle applications,” *IEEE Trans. Power Electron.*, vol. 28, no. 12, pp. 5477–5488.

[58] Y. P. Siwakoti, F. Z. Peng, F. Blaabjerg, P. Loh, and G. E. Town. (2015). “Impedance-source networks for electric power conversion part I: A topological review,” *IEEE Trans. Power Electron.*, vol. 30, no. 2, pp. 699–716.

[59] F. Ahmed, H. Cha, S. Kim, and H. Kim. (2016). “Switched-coupled-inductor quasi-Z-source inverter,” *IEEE Trans. Power Electron.*, vol. 31, no. 2, pp. 1241– 1254.

[60] F. Ahmed, H. Cha, S. H. Kim, and H. G. Kim. (2014). “A high voltage gain switched-coupled-inductor quasi-Z-source inverter,” in *Proc. Int. Power Electronics Conf. (IPEC-Hiroshima 2014 - ECCEASIA)*, pp. 480–484.

[61] F. Ahmed, H. Cha, S. Kim, and H. Kim. (2016). “Switched-coupled-inductor quasi-Z-source inverter*,” IEEE Trans. Power Electron.,* vol. 31, no. 2, pp. 1241– 1254.

[62] A. Ho, T. Chun, and H. T. Kim. (2015). "Extended boost active-switched-capacitor/switched-inductor quasi-Z-source inverters," *IEEE Trans. Power Electron.*, vol. 30, no. 10, pp. 568–5690.

[63] M. K. Nguyen, Y. C. Lim, and J. H. Choi. (2012). "Two switched-inductor quasi-Z-source inverters," *IET Power Electron.*, vol. 5, no. 7, pp. 1017–1025.

[64] K. Deng, F. Mei, J. Mei, J. Zheng, and G. Fu. (2014). "An extended switched-inductor quasi-Z-source inverter," *J. Electr. Eng. Technol.*, vol. 9, no. 2, pp. 541–549.

[65] C. J. Gajanayake, F. L. Luo, H. B. Gooi, P. L. So, and L. K. Siow. (2010). "Extended-boost Z-source inverters," *IEEE Trans. Power Electron.*, vol. 25, no. 10, pp. 2642–2652.

[66] D. Vinnikov, I. Roasto, T. Jalakas, R. Strzelecki, and M. Adamowicz. (2012). "Analytical comparison between capacitor assisted and diode assisted cascaded quasi-Z-source inverters," *Electr. Rev.,* vol. 88, no. 1a, pp. 212–217.

[67] D. Vinnikov, I. Roasto, T. Jalakas, and S. Ott. (2011). "Extended boost quasi-Z-source inverters: possibilities and challenges," *Electron. Elect. Eng,* vol. 112, no. 6, pp. 51–56.

[68] Y. Zhou, W. Huang, J. Zhao, and P. Zhao. (2012). "Tapped inductor quasi-Z-source inverter*,"* in *Proc. 27th Annul. IEEE Applied Power Electronics Conf. Exposition (APEC)*, pp. 1625–1630.

[69] W. Qian, F. Z. Peng, and H. Cha. (2011). “Trans-Z-source inverters,” *IEEE Trans. Power Electron.,* vol. 26, no. 12, pp. 3453–3463.

[70] M. K. Nguyen, Y. C. Lim, and S. J. Park. (2013). “Improved trans-Z-source inverter with continuous input current and boost inversion capability,” *IEEE Trans. Power Electron.*, vol. 28, no. 10, pp. 4500–4510.

[71] M. K. Nguyen, Q. D. Phan, Y. C. Lim, and S. J. Park. (2013). “Transformer-based quasi-Z-source inverters with high boost ability,” in *Proc. IEEE Int. Symp. Industrial Electronics (ISIE)*, pp. 1–5.

[72] M. K. Nguyen, Y. C. Lim, and Y. G. Kim. (2013). “T-Z-source inverters,” *IEEE Trans. Ind. Electron.*, vol. 60, no. 12, pp. 5686–5695.

[73] F. Z. Peng, M. Shen, and Z. Qian. (2005). “Maximum boost control of the Z-source inverter,” *IEEE Trans. Power Electron.*, vol. 20, no. 4, pp. 833–838.

[74] J. Khajesalehi, K. Sheshyekani, M. Hamzeh, and E. Afjei. (2016). “Maximum constant boost approach for controlling quasi-Z-source-based interlinking converters in hybrid AC–DC microgrids,” *IET Journal*, vol. 10, no. 4, pp. 938–948.

[75] Y. Li, J. Anderson, F. Z. Peng, and D. Liu. (2009). “Quasi-Z-source inverter for photovoltaic power generation systems,” in *Proc. 24th Annul. IEEE Appl. Power Electron. Conf. Expo. (APEC’09)*, pp. 918-924.

[76] IEEE recommended practices and requirements for harmonic control in electrical power systems, Std. IEEE-519-192.

[77] J. J. E. Slotine and W. Li. (1991). Applied Nonlinear Control. Englewood Cliffs, NJ, USA: Prentice-Hall.

[78] M. Mohammadi, J. Moghani, and J. Milimonfared. (2018). “A novel dual switching frequency modulation for Z-source and quasi-Z-source inverters,” *IEEE Trans. Ind. Electron*, vol. 65, no. 6, pp. 5167-5176.

[79] J. Liu, S. Jiang, D. Cao, and F. Z. Peng. (2013). “A digital current control of quasi-Z-source inverter with battery,” *IEEE Trans. Ind. inform*, vol. 9, no.2, pp. 5167-5176.

[80] C.T. Chen. (2012). Linear System Theory and Design, *Oxford University Press*, New York, NY, USA.

[81] J. Liu, S. Jiang, D. Cao, and F. Z. Peng. (2013). “A digital current control of quasi-Z-source inverter with battery,” *IEEE Trans. Ind. Inf.*, vol. 9, no. 2, pp. 928-937.

[82] A. Abrishamifar, A. Ahmad, M. Mohamadian. (2012). “Fixed switching frequency sliding-mode control for single-phase unipolar inverters,” *IEEE Trans. Power Electron.*, vol. 27, no. 5, pp. 2507–2514.

[83] F. Guo, L. Fu, C. H. Lin, C. Li, and J. Wang. (2012). "Small signal modeling and controller design of a bidirectional quasi-Z-source inverter for electric vehicle applications," *IEEE Energy Conversion Congress and Exposition (ECCE),* pp. 2223–2228.

[84] F. Bagheri, H. Komurcugil and O. Kukrer. (2018). "Modified MIMO sliding-mode controller with constant switching frequency for grid-connected LCL-filtered quasi-Z-source inverter," in *Proc. of 44th Annual Conf. of the IEEE Industrial Electronics Society*, pp. 3889-3894.

[85] F. Bagheri, H. Komurcugil and O. Kukrer. (2018). "Fixed switching frequency sliding-mode control methodology for single-phase LCL-filtered quasi-Z-source grid-tied inverters," in *Proc. of 12th International Conference on Compatibility, Power Electronics and Power Engineering*, Qatar, pp. 1-6.

[86] F. Bagheri, H. Komurcugil, O. Kukrer, S. Bayhan and N. Guler. (2019). "Modeling, analysis and sliding mode controller design of high voltage gain switched-Z-source inverter," in *Proc. of 13th International Conference on Compatibility, Power Electronics and Power Engineering*, Denmark.

[87] F. Bagheri, H. Komurcugil, O. Kukrer, N. Guler, S. Bayhan (2019). "Multi-input Multi-output-based sliding-mode controller for single-phase Quasi-Z-source inverters, ", *IEEE Trans. Ind. Electron*, Early Access